



**Università
degli Studi
di Palermo**

AREA RICERCA E TRASFERIMENTO TECNOLOGICO
SETTORE DOTTORATI E CONTRATTI PER LA RICERCA
U. O. DOTTORATI DI RICERCA

Dottorato Di Ricerca In Scienze Della Terra e Del Mare
Dipartimento di Scienze della Terra e del Mare
Settore Scientifico Disciplinare Geografia Fisica e Geomorfologia

**STOCHASTIC ASSESSMENT OF LANDSLIDE
SUSCEPTIBILITY ALONGSIDE “VÍA AL LLANO” HIGHWAY,
COLOMBIA**

IL DOTTORE

LAURA PAOLA CALDERON CUCUNUBA

IL COORDINATORE

PROF. ALESSANDRO AIUPPA

IL TUTOR

PROF. CHRISTIAN CONOSCENTI

CO-TUTOR

PROF. GERMAN VARGAS CUERVO

CICLO XXXVI
ANNO CONSEGUIMENTO TITOLO 2024

INDEX

ACKNOWLEDGMENTS.....	4
CHAPTER 1. INTRODUCTION	5
CHAPTER 2. STUDY AREA AND MATERIALS.....	6
2.1. Location	6
2.2. Geology	8
2.3. Geomorphology.....	16
2.4. Historic landslides	22
2.5. Previous landslides susceptibility studies in the study area.....	28
2.6. Pluviosity	33
CHAPTER 3. LANDSLIDES, REMOTE SENSING AND SOFTWARE	37
3.1. Landslides classification.....	37
3.2. Landslides susceptibility maps	49
3.3. Landslides inventory	50
3.4. Mapping units.....	50
3.5. Remote sensing techniques.....	52
3.5.1. Digital Terrain Models (DTMs)	52
3.5.2. Optical images	52
3.5.3. Radar images	53
3.6. Predictors	54
3.7. Modeling techniques.....	54
3.8. Software.....	55
3.8.1. R and RStudio	55
3.8.2. QGIS.....	56
3.8.3. SAGA GIS	56
3.8.4. Google Earth Engine (GEE).....	56
CHAPTER 4. METHODOLOGY	57
4.1. Geomorphology Mapping.....	57
4.3. Pluviosity	59
4.4. Landslides inventory	62
4.4.1. Google Earth	62
4.4.2. Google Earth Engine.....	62
4.5. Confusion Matrix.....	64
4.6. Independent variables	66
4.6.1. The elevation (ELE)	66
4.6.2. The slope (SLO)	66

4.6.3. The aspect (ASP)	67
4.6.4. Plan Curvature (PCV).....	67
4.6.5. Profile curvature (PRC)	67
4.6.6. Convergence Index (CI)	67
4.6.7. LS Factor (LSF).....	67
4.6.8. Stream Power Index (SPI)	68
4.6.9. Topographic Position Index (TPI)	68
4.6.10. Topographic Wetness Index (TWI)	68
4.6.11. Vertical Distance to Channel Network (VDCN)	68
4.7. Data sampling.....	69
4.8. Statistical modeling.....	70
4.9. Validation strategy.....	70
CHAPTER 5. RESULTS.....	71
5.1. Geomorphology Map.....	71
5.2. Pluviosity maps	75
5.3. Landslides inventory	78
5.4. Importance of predictor variables.....	81
5.5. Validation of the models.....	86
5.6. Landslide susceptibility maps.....	91
CHAPTER 6. DISCUSSION	94
6.1. Geomorphology Mapping.....	94
6.2. Pluviosity	99
6.3. Automatic landslide inventory.....	102
6.4. Variable importance analysis and comparative model results	103
CHAPTER 7. CONCLUSIONS	106
REFERENCES.....	108

ACKNOWLEDGMENTS

This project began as a personal proposal, inspired by my frequent travels between Bogotá and Villavicencio during vacation periods. On the journey between these cities, it is possible to see the variety of rock and geological processes in the area. Furthermore, is an ideal location to observe and understand the interaction of anthropic activities and the recent geomorphological processes such as landslides, floods, and soil erosion.

I am grateful with the Università degli Studi di Palermo for give the opportunity to foreign students to pursue doctoral studies with financial support. Special thanks to my Supervisor Christian Conoscenti for agreeing to guide me in the development of this project, which had no funding. Thank you, Professor, for motivating me to give my best and allowing me to grow as a professional in Geomorphology. I also extend my gratitude to my co-Supervisor German Vargas Cuervo for his advice, feedback, and support.

I am also thankful for the opportunities provided by various Italian and European institutions that have contributed to my professional growth, such as the Geomorphological Mapping Course by University of Camerino, the Soil Erosion Course by International Association of Geomorphologists, international conferences in Germany, Austria, Portugal, and Italy. Additionally, I appreciate the Geomorphology courses taught by Professor Eduardo Rotigliano and Professor Cipriano Di Maggio, the Remote Sensing courses by Professor Antonino Maltese, and professors of the courses on Geostatistics and data analysis, and Google Earth Engine.

Personally, I thank God for all the opportunities and challenges He has given me in life, and with them, the strength to face each day. Thanks to Mother Earth for allowing me to study her and connect through rocks, minerals, plants, animals, and materials. Thanks to my spiritual guides.

I dedicate this thesis to my parents because they are always willing to help me. My mom was of grater assistance by being with me during these last three months in Palermo, and my dad in Bogotá managing the "Ritmika Laura Calderón" school. Thanks to my family, sisters (Jesi and Meli), and nephews for their support from a distance. Thanks to my pets Simona, Lupita, and Arancina for the joy they bring me with their presence, and to Andres for being my partner over those years. Thanks to my doctors for supporting me in improving my health, and to my friends for their advice and support in the distance. In addition, I am grateful to the colleagues and people I have met in Italy, who have been able to share this period with me.

CHAPTER 1. INTRODUCTION

Steep slopes, deforestation, unconsolidated deposits, high annual rainfall, and a highly dissected landscape contribute to frequent landslides along one of the most important Colombian highways, the "Via al Llano," often causing traffic disruptions. This road connects Bogota, the capital of Colombia, with Villavicencio, the capital of the Meta state, facilitating the transportation of agricultural and industrial products and promoting economic development through tourism.

The Via al Llano highway traverses five municipalities: Chipaque, Caqueza, Quetame, Guayabetal, and Villavicencio. These areas are characterized by folds, faults, joints, and outcrops of various lithologies and ages (INGEOMINAS, 1998, 2011). The geological composition on the region includes Precambrian phyllites, Paleozoic sandstones and claystones, Jurassic conglomerates, Cretaceous siltstones, mudstones, and quartz-rich sandstones, as well as Quaternary deposits resulting from fluvial and gravitational processes (INGEOMINAS, 1998, 2011).

The landscape of the road features steep slopes molded by both tributaries and the main watercourses of the Rio Negro, Rio Blanco, and Guayuriba River. The study area, which encompasses the basins of these rivers, experiences significant precipitation ranging from 1000 to 2500 mm/year in the north and central areas, and 2500 to 5000 mm/year in the south, with peak rainfall occurring in May, June, and July, often triggering landslides.

Recent mass wasting events in June 2017 and May 2019 blocked the road for 1 and 6 months, respectively, despite efforts by the Colombian Geological Service (SGC) to mitigate such incidents through inventory maintenance and hazard mapping since 2010. Hence, Calderón-Guevara et al. (2022) and Herrera-Coy et al. (2023) have pursued alternative landslide prediction methods for the Via al Llano area. However, their focus on predictive modeling often yields maps with insufficient correlation to the road, necessitating a new approach.

To address the complexity and potential disconnect between the area and the road, this study aims to enhance spatial resolution by subdividing it into five municipalities based on political boundaries. This subdivision accounts for significant lithological, climatic, and geomorphological variability, yielding results at a scale of 1:50,000 instead of the previous 1:100,000 scale. In addition, annual average precipitation will be considered as an independent predictive variable, derived from data interpolation of rain gauge stations surrounding the study area. This variable also exhibits unique seasonal behaviors in each of the five municipalities throughout the year.

Furthermore, the study will assess the feasibility of developing automatic inventories using radiometric data from optical and radar satellite images. Leveraging the Google Earth Engine (GEE) platform, we aim to streamline the time-consuming process of manual landslide inventory creation. Additionally, radar images will be evaluated for their effectiveness in landslide detection, particularly in cloud-obscured areas.

Subsequently, the relationship between predictor variables (e.g., elevation, slope angle, aspect, curvature, lithology, precipitation, NDVI) and landslides will be modeled using Multivariate Adaptive Regression Splines (MARS) technique. Models will be calibrated and validated using ten training and ten test samples, with predictive performance assessed through the area under the Receiver Operating Curve (AUC).

Additionally, geomorphological maps will be produced for the five municipalities, inspired by the methodology used in Italy with "Cuaderno 13" elaborated by AIGEO and CARG entities.

CHAPTER 2. STUDY AREA AND MATERIALS

2.1. Location

The Via al Llano is considered one of the most important highways in Colombian, connecting Bogota (the capital) to Villavicencio (the capital of the Meta state) (Fig. 1a). This route facilitates tourism, the transportation of agricultural-industrial products and promotes economic progress in the territories located in the center and in the southeastern part of the country. In addition, the road passes through the municipalities of Chipaque, Cáqueza, Quetame, Guayabetal and Villavicencio (Fig. 1b).

The current highway has 86 km of length, crossing the Cordillera Oriental, one of the three branches of the Colombian Andes formed by the subduction of the Nazca plate beneath South America. The study area covers 520km², which includes basins that drain water toward the road (Fig. 1b, 2a, and 2b). The main rivers on the area are Rio Blanco, Rio Negro and Guayuriba River (Fig. 2).

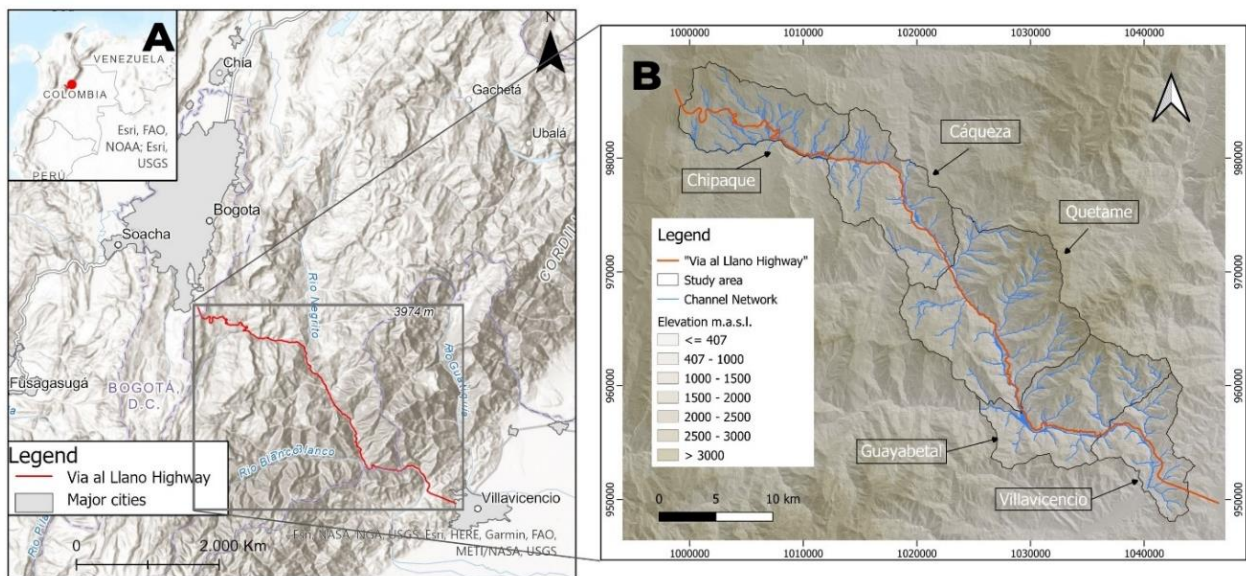


Fig. 1. (a) Location on Regional setting. (b) Study area and municipalities traversed by the road. Coordinate Reference System EPSG: 3116. MAGNA-SIRGAS/Colombian Bogota zone.

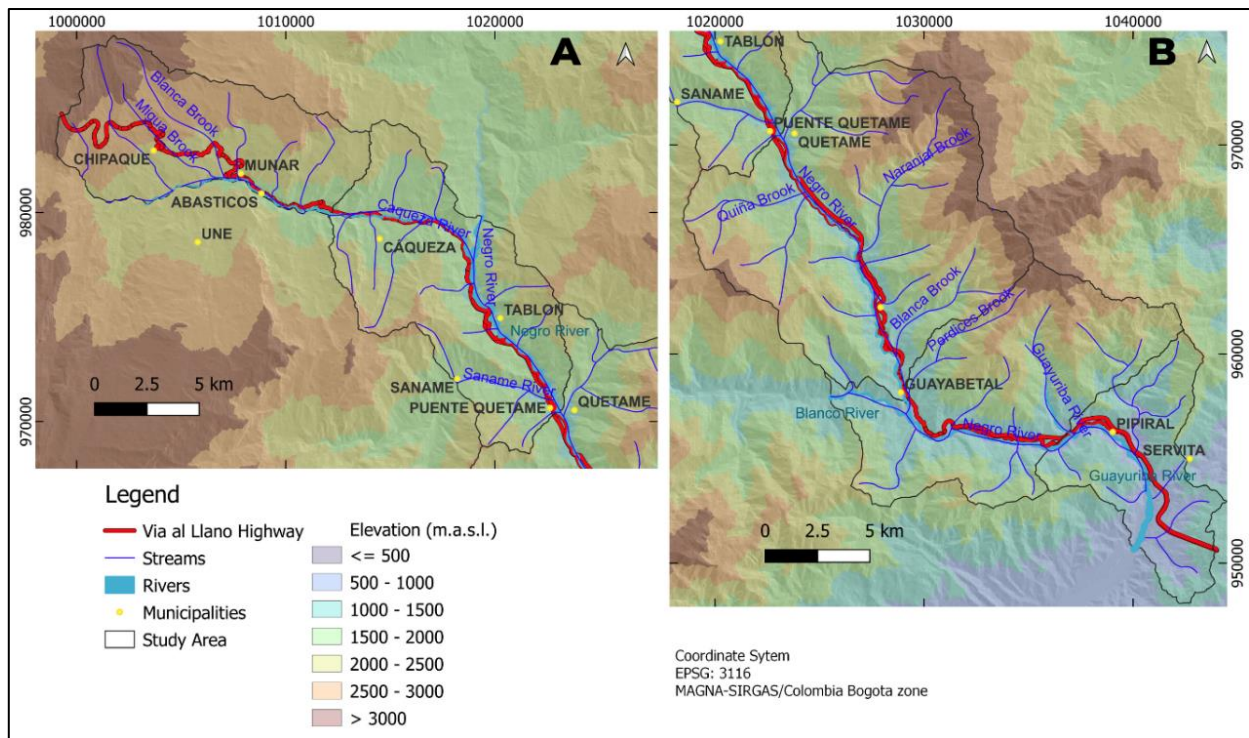


Fig. 2. (a) Watercourses in Chipaque and Caqueza. (b) Watercourses in Quetame, Guayabetal and Villavicencio.

The study area is part of the topographic sheets “247” and “266” at a scale of 1:100,000 (Fig. 3A, 3B), according to the division established by the *Instituto Geográfico Agustín Codazzi* (IGAC), the entity responsible for the official basic cartography of Colombia. These two sheets cover the departments of Cundinamarca and Meta. Additionally, the study area encompasses 10 topographic sheets at a scale of 1:25,000 (Fig. 3C), which, according to the official nomenclature, are as follows: 247-I-C, 247-I-D, 247-III-A, 247-III-B, 247-III-D, 247-IV-A, 247-IV-C, 266-I-B, 266-II-A, 266-II-C.

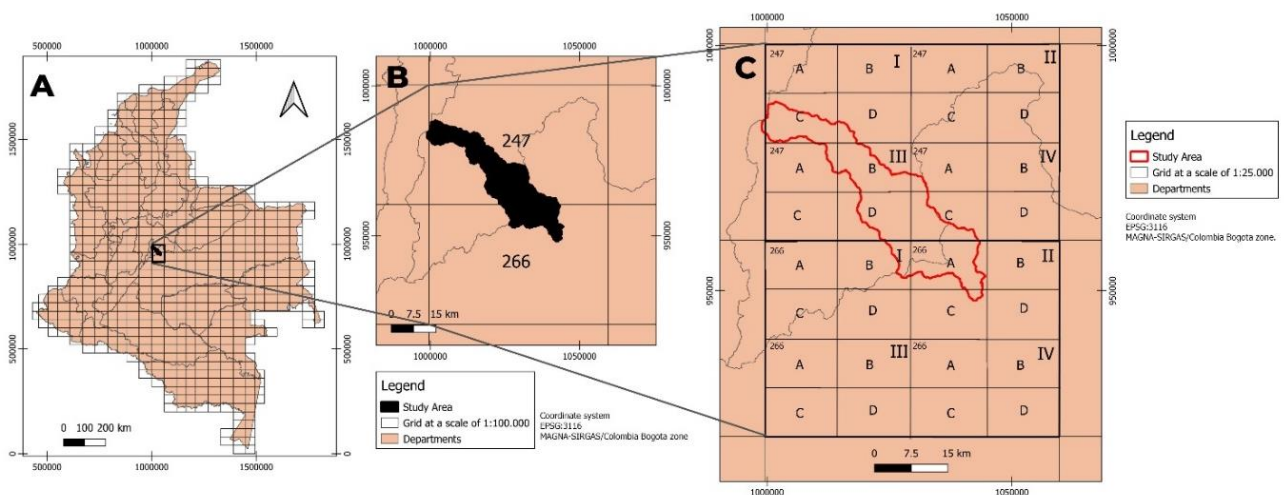


Fig. 3. (a) Topographic sheets of Colombia. (b) Study area on the topographic grid sheet at a scale of 1:100,000. (c) Study area on the topographic grid division sheet at a scale of 1:25,000.

2.2. Geology

In the area, Precambrian metamorphic rocks, and Paleozoic to Cenozoic sedimentary rocks outcrop (INGEOMINAS, 1998, 2011). The metamorphic rocks are grouped in the Quetame Group, comprising the Susumuco and Guayabetal Formations. Both formations consist of gray and green phyllites, but the Guayabetal Formation also includes quartzite and gray schist, products of low-grade contact metamorphism from pre-Devonian age (INGEOMINAS et al., 2001).

The Quetame Group is in fault contact with Paleozoic sedimentary rocks grouped by Segovia (1963, as cited in INGEOMINAS et al., 2011) as the Farallones Group. This group includes the Areniscas de Gutierrez Formation, Lutitas de Pipiral Formation, and Capas Rojas del Guatiquia Formation. The Areniscas de Gutierrez Formation is composed of conglomeratic, shales, and sandstone levels, from the Middle Devonian. The Lutitas de Pipiral Formation consists of gray shales and siltstones intercalated with some gray limestones, also from the Middle Devonian. Lastly, the Capas Rojas del Guatiquia Formation comprises gray to red siltstone intercalated with gray-green sandstones, dating back to the Carboniferous period (INGEOMINAS et al., 2011).

In angular discordance with the preceding Paleozoic sedimentary rocks is the Buenavista Formation, from the Upper Jurassic Period (Tithonian). This formation is characterized by breccias and conglomerates containing sedimentary and metamorphic lithics in the lower segment, and sandstones to mudstones in the upper levels. The potential formation involves erosion and deposition associated with the syn-rift processes during the Triassic-Jurassic and Lower Cretaceous rifting in the area, in a Cretaceous Sea (INGEOMINAS et al., 2011).

The Cáqueza Group represents the initial formations of the Lower Cretaceous Period (from Berriasian to Hauterivian). These rocks display an angular unconformity with the Buenavista Formation and the Paleozoic Farallones Group. The Cáqueza group is composed of the Lutitas de Macanal Formation and the Areniscas de Cáqueza Formation, which have variable thicknesses due to differential subsidence from tectonic movements on the rifting period. The Lutitas de Macanal Formation comprises black shales intercalated with sandstones and features abundant fossils of ammonites and bivalves. The Areniscas de Cáqueza Formation consists of sandstones rich in quartz, intercalated with light beds of black mudstones. It also contains fossils of bivalves, echinoderms, ammonites, and foraminifera, dating from the Hauterivian Age (INGEOMINAS et al., 2011).

Following this, the next rocks were deposited in concordant-transitional sequences in a continental environment post-rift, during Upper Cretaceous. The Fomeque Formation consists of gray-black bioclastic limestones intercalated with black to green mudstone, dating from the Barremian to Aptian periods (Guerrero, 2002, as cited in INGEOMINAS et al., 2011). Subsequently, in a concordant sequence, the Une Formation is found, which is a succession of thick sandstone layers, separated by beds of claystone with shale layers, from the Albian to Cenomanian Age. The Chipaque Formation composed of black mudstones with minor intercalations of fine-grained sandstones and limestones, deposited between the Cenomanian to Santonian Ages. The last Cretaceous lithology found in the study area is the Arenisca Dura Formation composed of fine-grained quartzose sandstones, white in color, tabular, massive, with intercalations of thin layers of very fine sandstones exhibiting wavy planar parallel

lamination. This formation is dated from the Santonian to the Campanian (INGEOMINAS et al., 2011).

During the Upper Miocene, rhyodacite intruded into the Lutitas de Macanal Formation in the Quetame region. This intrusion occurs during the new compression environment that subsequently leads to the current mountain range. During this period, the faults that were normal in the rift period become reactivated and change their behavior to thrust faults (INGEOMINAS et al., 2011).

Additionally, in the study area, there are unconsolidated units from Holocene Epoch. This includes alluvial terraces, colluvial deposits and recent alluvial deposits. The latest deposits are located along the riverbeds, of the Une River, the Caqueza River, the Negro River, Blanco River and the Guatiquia River (INGEOMINAS et al., 2001, 2011).

The lithological composition and stratigraphic position of each formation exposed in the study area are summarized in the stratigraphic table in Fig. 5 (INGEOMINAS et al., 2001, 2011). Similarly, the location of each formation in the area is represented in the lithological map of the Fig. 4, information extracted from the geological maps of sheets 247 and 266 at a 1:100,000 scale from the Colombian Geological Service (SGC) (INGEOMINAS, 1998, 2011). Additionally, the drainage locations were updated using images available on Google Earth between the years 2020 and 2022.

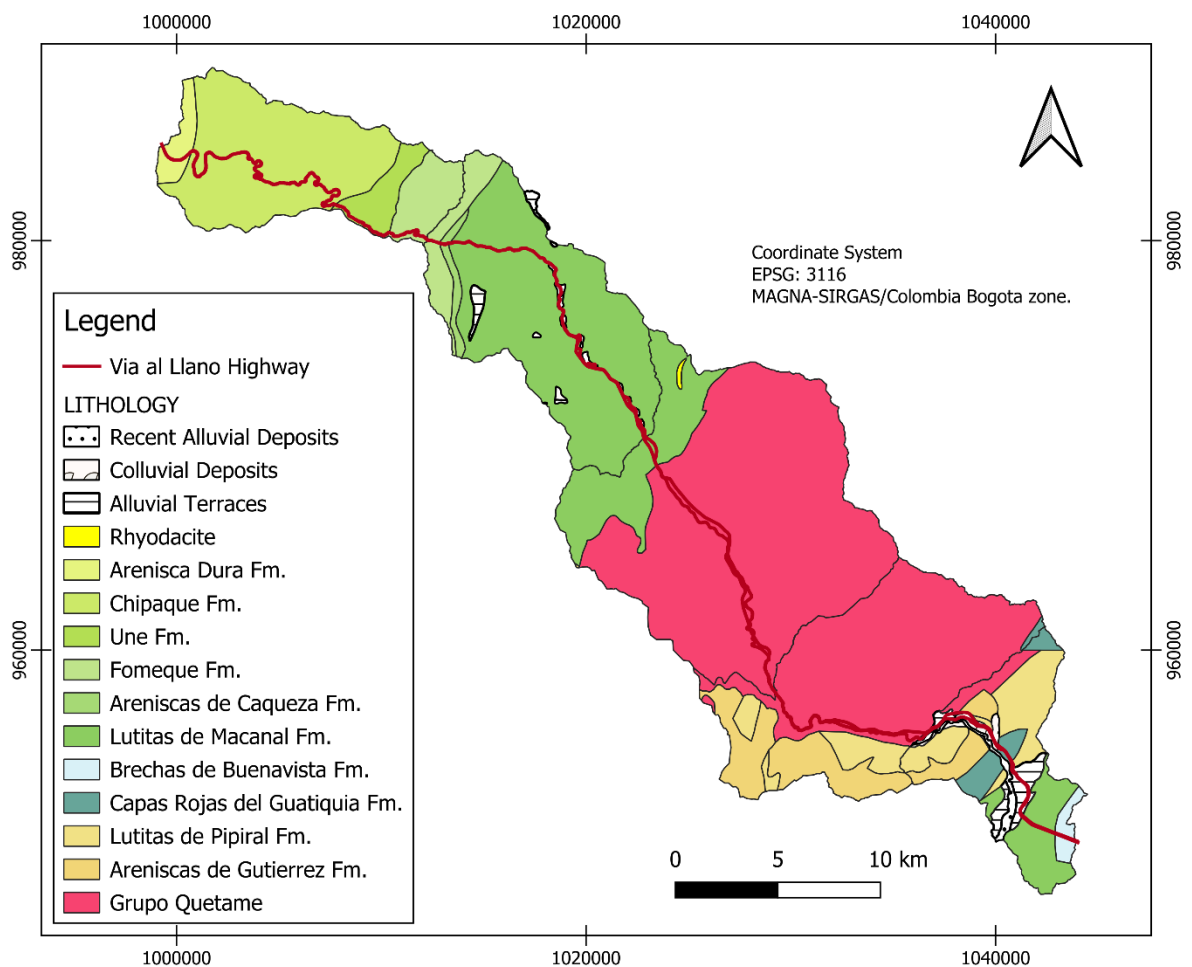


Fig. 4. Distribution of Lithologies in the study area of “Via al Llano” highway. Modified from (INGEOMINAS, 1998, 2011)

	UNITS	TIME	GRAPHIC LITHOLOGY	LITHOLOGICAL DESCRIPTION
Unconsolidated Units	Recent alluvial deposits	Holocene Epoch		Unconsolidated gravel, pebbles, and stones in a sandy-silty matrix
	Colluvial deposits			Mass movement deposits
	Alluvial terraces			Rounded and subrounded pebbles embedded in a sandy-loamy matrix
	Rhyodacite	Upper Miocene		Intrusive igneous rock with an acidic composition
	Arenisca Dura Fm.	Santonian to Campanian		Sandstones with occasional clayey layers
	Chipaue Fm.	Cenomanian to Santonian		Mudstones with fine-grained sandstones and limestones
	Une Fm.	Albian to Cenomanian		Sandstone with some claystone - shale layers
	Fomeque Fm.	Barremian to Aptian		Bioclastic limestones intercalated with mudstone
	Caqueza Group	Areniscas de Caqueza Fm.	Lower Cretaceous (Berriasian - Hauterivian)	
Lutitas de Macanal Fm.				Shales with some sandstones
	Brechas de Buenavista Fm.	Upper Jurassic (Tithonian)		Lithic breccias and conglomerates of Farallones Group
Farallones Group	Capas Rojas del Guatiquia Fm.	Carboniferous		Mudstones with some sandstones
	Lutitas de Pipiral Fm.	Middle Devonian		Shales
	Areniscas de Gutierrez Fm.	Middle Devonian		Lithic conglomerates of the Quetame Group - sandstones - shales
Quetame Group	Susumuco Fm.	Pre-Devonian		Phyllites
	Guayabetal Fm.	Pre-Cambrian - Pre-Devonian		Phyllites - quartzite - schist

Fig. 5. Stratigraphic Column of the Study Area surrounding the Highway “Via al Llano”. Modified from INGEOMINAS et al., (2011)

For a more thorough analysis, the study area was divided into the five municipalities through which the road passes: Chipaque, Cáqueza, Quetame, Guayabetal, and Villavicencio, located from north to south, respectively. In the Chipaque area (Fig. 6), structures exhibit a predominantly north-south strike orientation; however, the dip direction of these formations varies due to the presence of two synclines. The Teusacá Syncline that has its axial axis in the middle of the Chipaque Formation, while the Mercadillo Syncline is located in the middle of the Fomeque Formation. Additionally, three faults cut across the road and the course of the Une River. The first brings the Une and Fomeque formations into contact, the second is situated in the middle of the Fomeque Formation with a NE-SW direction, and the third is known as the Cáqueza River Fault, running parallel to its course (INGEOMINAS, 2011; INGEOMINAS et al., 2011).

In the Cáqueza area (Fig. 7), the Lutitas de Macanal Formation covers the most extensive area and displays a series of faults, predominantly of reverse component. Among them, the Cáqueza River Fault, the Negro River Fault, and the Quebrada Honda Fault stand out. The Cáqueza River Fault maintains an orientation parallel to the river course, as its path is influenced by this fault. It is a strike-slip fault that affects the Fomeque, Areniscas de Caqueza, and Lutitas de Macanal formations. The Negro River Fault, with an approximate north-south direction, controls the course of the Negro River and is also classified as a strike-slip fault. On the other hand, the Quebrada Honda Fault, located to the south of the area, follows a direction of approximately N30°E with a dip towards the SE. Additionally, in the northern part of this area, the Ubaque Fault emerges, establishing contact between the Fomeque Formation with Areniscas de Caqueza, and Lutitas de Macanal formations. It is characterized as a thrust fault with a dip of N35°E (INGEOMINAS, 2011; INGEOMINAS et al., 2011).

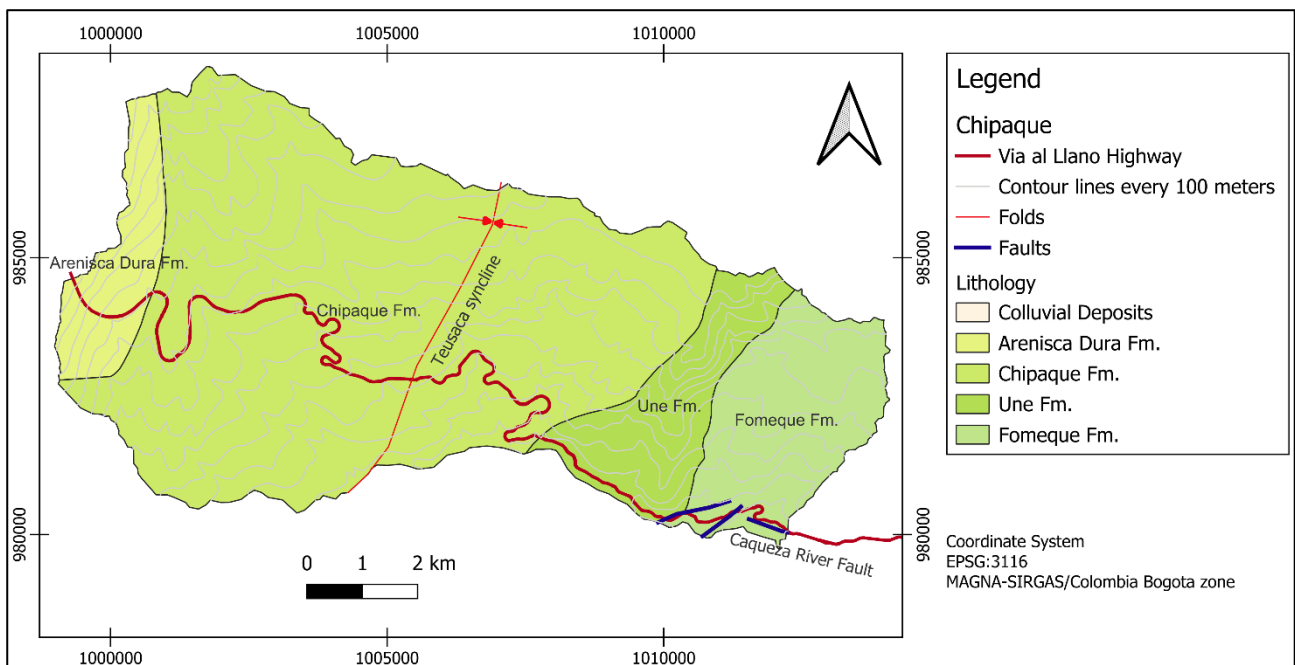


Fig. 6. Geological and structural setting in the Municipality of Chipaque. Modified from INGEOMINAS, (2011)

In the Quetame area (Fig. 8), the presence of the Lutitas de Macanal Formation and the Quetame Group is identified, with the latter being the lithological unit that covers the largest extent in the zone. The Las Mercedes and Quetame faults are responsible for the interaction between these two formations. Additionally, it is postulated that the Quetame Fault could be a high-angle regional and cortical structure that facilitated the intrusion of the rhyodacitic igneous body and some thermal springs south of the town of Quetame. This fault has an orientation of N25E and controls the course of the Contador River. Within the Quetame Group unit, the presence of the Quebrada Grande Fault and the Jabonera Fault is also observed, with the latter exerting control for the Negro River until its confluence with the Blanco River (INGEOMINAS, 2011; INGEOMINAS et al., 2011).

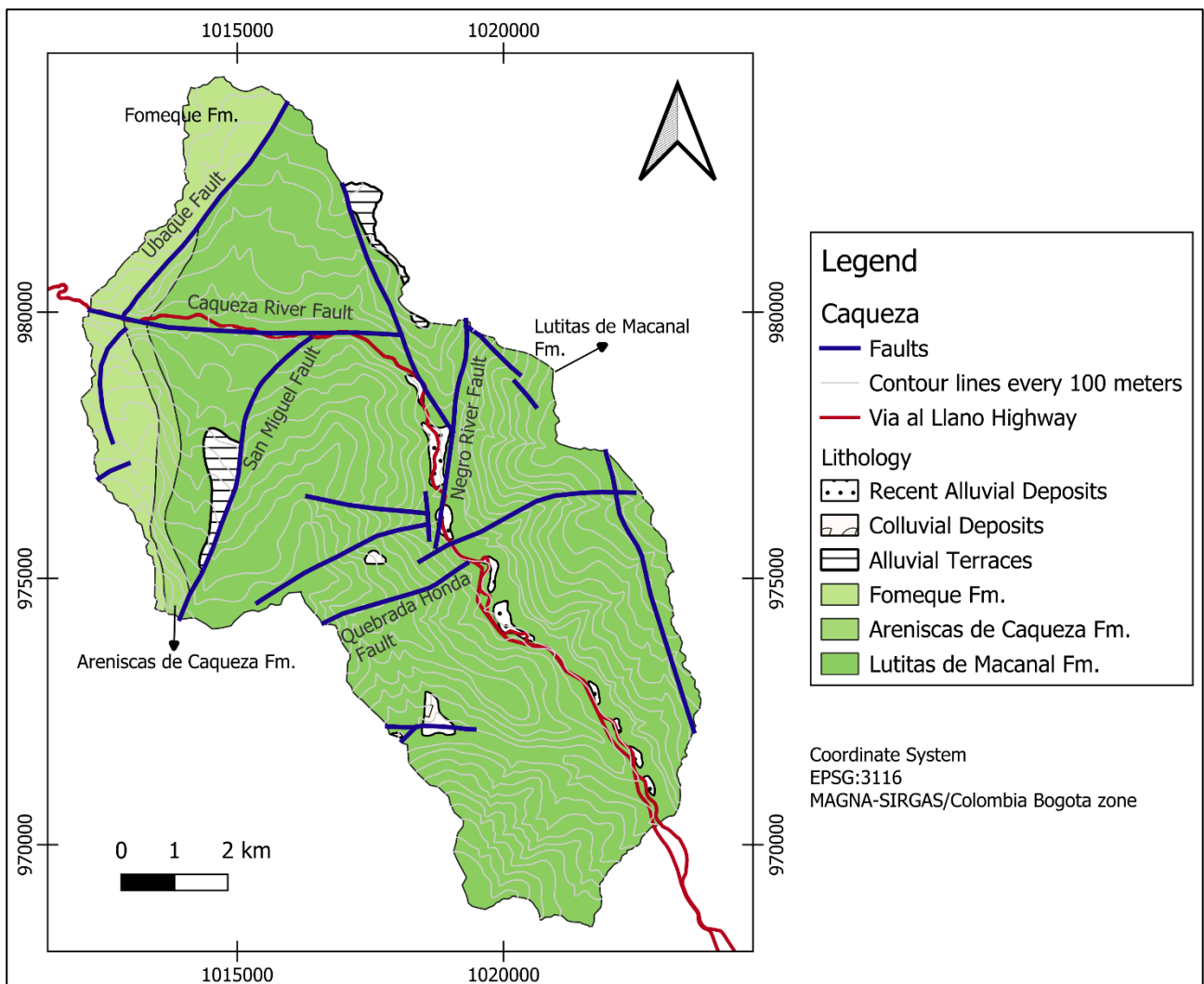


Fig. 7. Geological and structural setting in the Municipality of Caqueza. Modified from (INGEOMINAS, (2011))

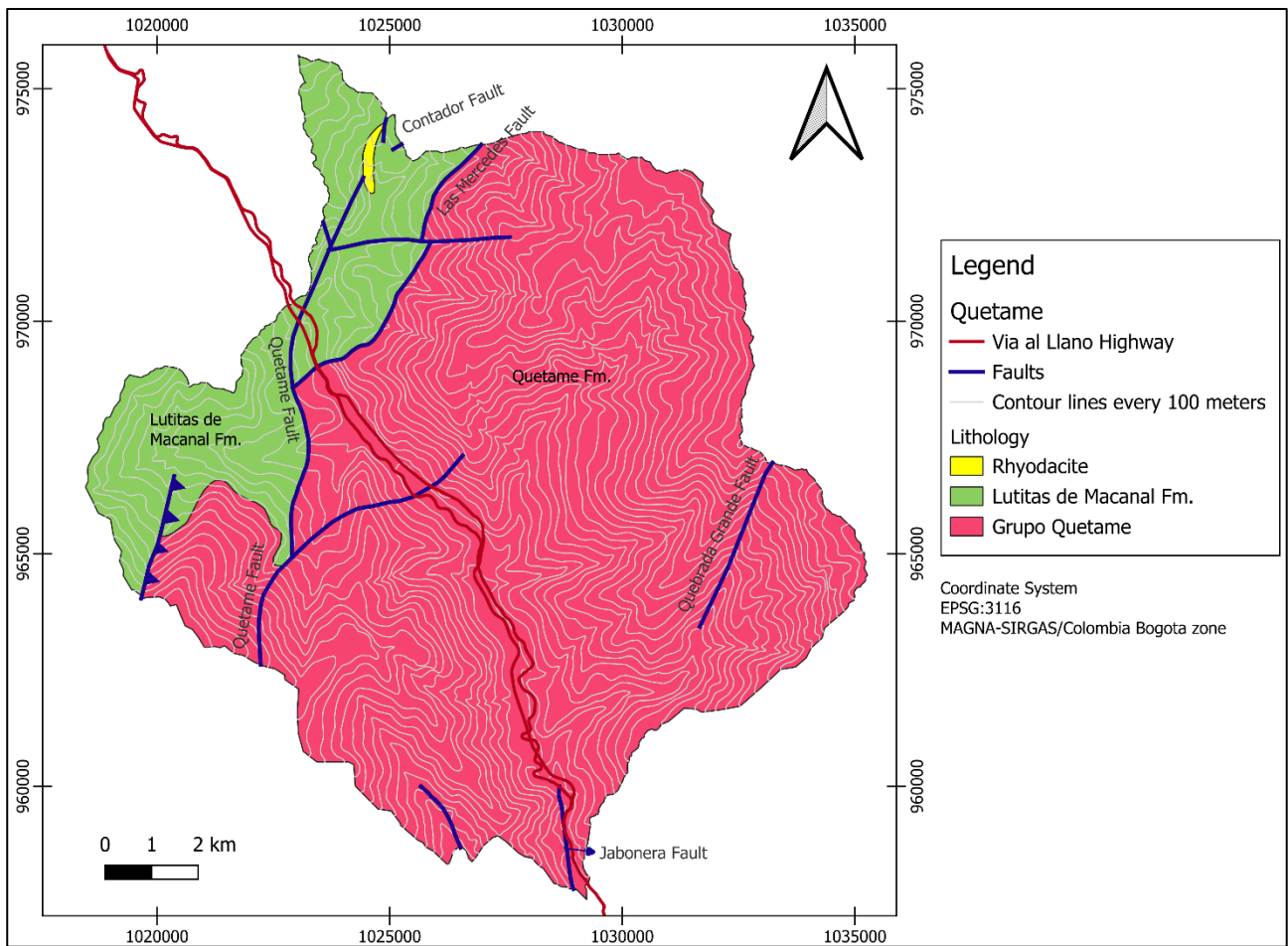


Fig. 8. Geological and structural setting in the Municipality of Quetame. Modified from INGEOMINAS, 2011)

In the Guayabetal area (Fig. 9), the predominant formations are the Quetame Group, along with the Areniscas de Gutiérrez and Lutitas de Pipiral formations. The Jabonera Fault persists in a north-south direction and affects the Areniscas de Gutiérrez Formation. Notably, over the Quetame Group, the presence of the San Juanito Fault stands out, facilitating contact with the Capas Rojas del Guatiquia Formation. This fault, with a sub-vertical inverse component, exhibits a westward dip. Subsequently, the Portachuelo Fault and the Susumuco Fault are encountered. The latter is considered a dextral strike-slip fault with a direction of N15W, controlling the course of the Susumuco Brook. Additionally, the Rio Blanco Fault separates the Quetame Group from the Farallones Group (Areniscas de Gutiérrez and Lutitas de Pipiral formations). It has an east-west orientation and a length of 10 km, structurally controlling the flow of water, initially from the Rio Blanco and then from the Rio Negro. Finally, over the formations of the Farallones Group, a variety of faults and folds are observed, including anticlines and synclines (INGEOMINAS, 1998; INGEOMINAS et al., 2001).

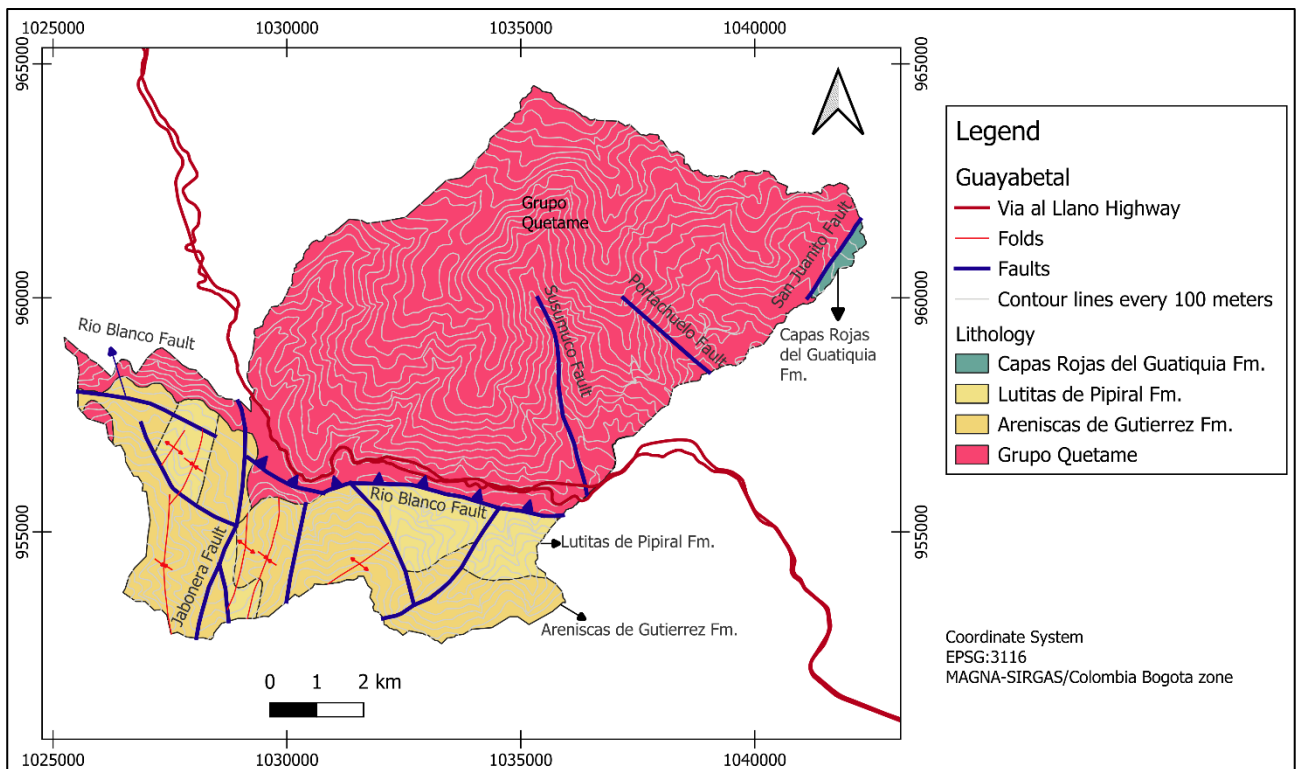


Fig. 9. Geological and structural setting in the Municipality of Guayabetal. Modified from INGEOMINAS, (1998)

Finally, in the Villavicencio area (Fig. 10), the Susumuco Fault continues to affect the formations of the Farallones Group, with a movement considered dextral strike-slip. Additionally, the Rio Blanco Fault continues to control the course of the Rio Negro, and this reverse fault now extends to the northeast, maintaining the contact between the Quetame Group and the Farallones Group. However, to the east, it allows contact between the Capas Rojas del Guatiquia Formation and the Areniscas de Gutiérrez Formation. Another significant fault facilitating the contact between these two formations is the Portachuelo Fault. Also noteworthy is the Servita Fault, connecting the Devonian-age Lutias de Pipiral Formation with the Lower Cretaceous Lutitas de Macanal Formation, given its main inverse component. It is also observed a faulted contact between the Cretaceous-age Lutitas de Macanal and the Brechas de Buenavista Formation through the Buenavista Fault. Finally, there is the El Buque Fault, displacing the aforementioned formations from east to west due to its sinistral strike-slip component. Additionally, over the las Lutitas de Macanal, significant deformation is observed due to the presence of several synclines and anticlines within it (INGEOMINAS, 1998; INGEOMINAS et al., 2001).

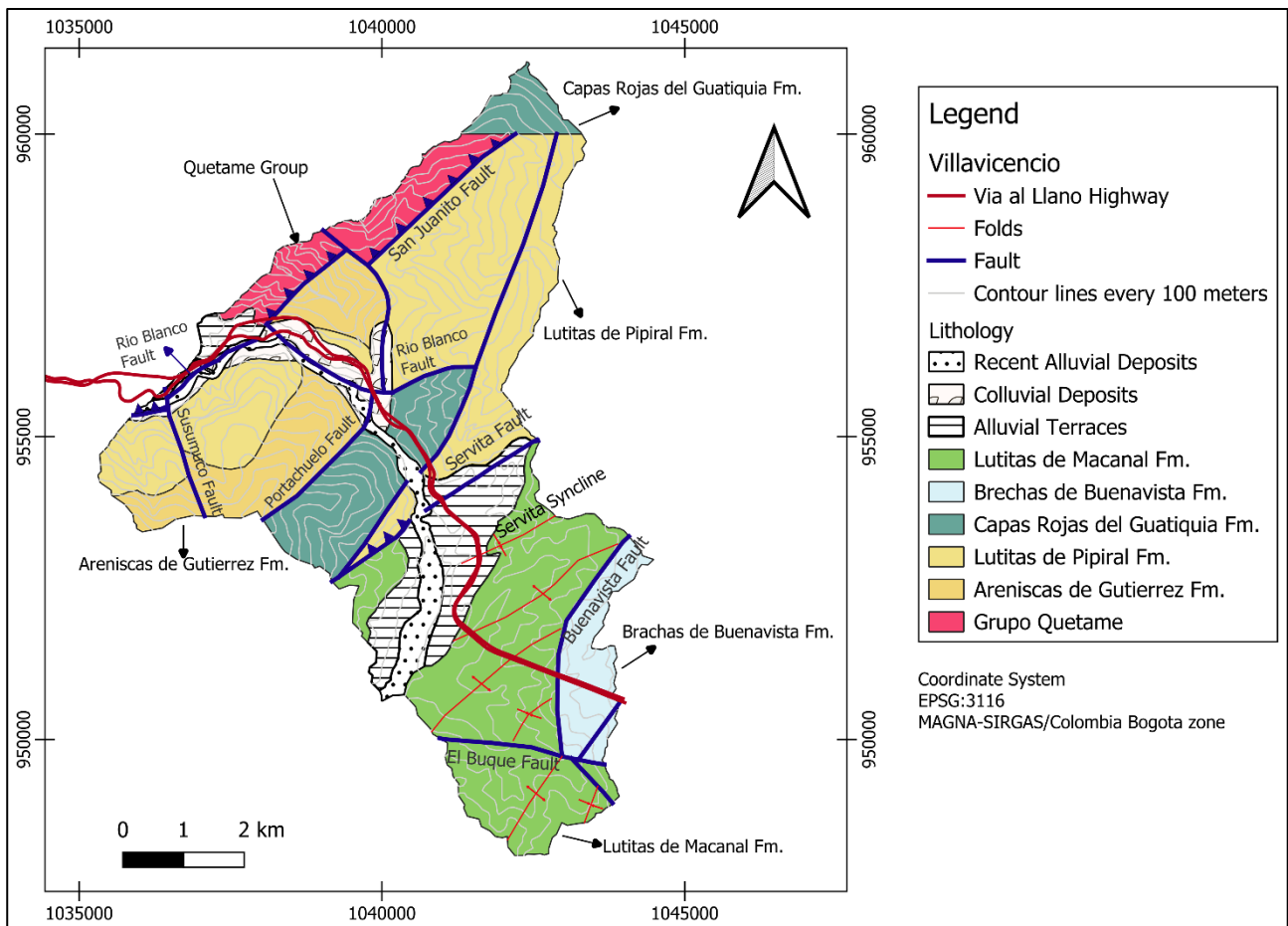


Fig. 10. Geological and structural setting in the Municipality of Villavencio. Modified from INGEOMINAS, (1998)

2.3. Geomorphology

Geomorphology is the scientific discipline that studies the landforms of the Earth's surface and their spatial combinations (Ciccacci, 2010). Thus, the discipline aims to describe terrain features, explaining their origin and evolution over geological time. Additionally, it seeks to classify landscapes based on the dominant natural processes and agents shaping them, called morphogenetic environment (Servicio Geologico Colombiano et al., 2012).

A morphogenetic environment encompasses the physical, chemical, biotic, and climatic conditions under which landforms were formed. According to the recompilation made by Servicio Geologico Colombiano et al., (2012) the morphogenetic environments are categorized into structural, volcanic, denudational, fluvial, deep-sea and coastal marine, glacial, aeolian, karstic, anthropogenic, and/or biological.

In the study area, the *Servicio Geologico Colombiano* (SGC, Colombian Geological Survey) published geomorphological maps for sheets 247 and 266 in 2018, following the methodological proposal of Servicio Geologico Colombiano et al., (2012). In this context, the morphogenetic environments highlighted in the area are structural, denudational, fluvial, and glacial (Table 1, 2 and 3).

- The structural environment corresponds to landforms generated by active tectonics resulting from the Earth's internal dynamics. Folding and faulting in rocks are associated with this environment, and cartographically, it is represented by purple.
- The denudational environment is determined by weathering processes, predominantly hydro-erosive processes, and phenomena of transposition or mass removal acting on pre-existing landforms. For this type of region, the adopted cartographic color is brown.
- The fluvial environment, differentiated by blue, corresponds to landforms generated by processes related to fluvial activity.
- The glacial environment is distinguished by landforms formed by glacial action in high mountains. In cartography, it is differentiated by the color gray.
- The anthropic environment refers to forms generated and modified by human activity on the land surface. In cartography, it is designated by the color black.

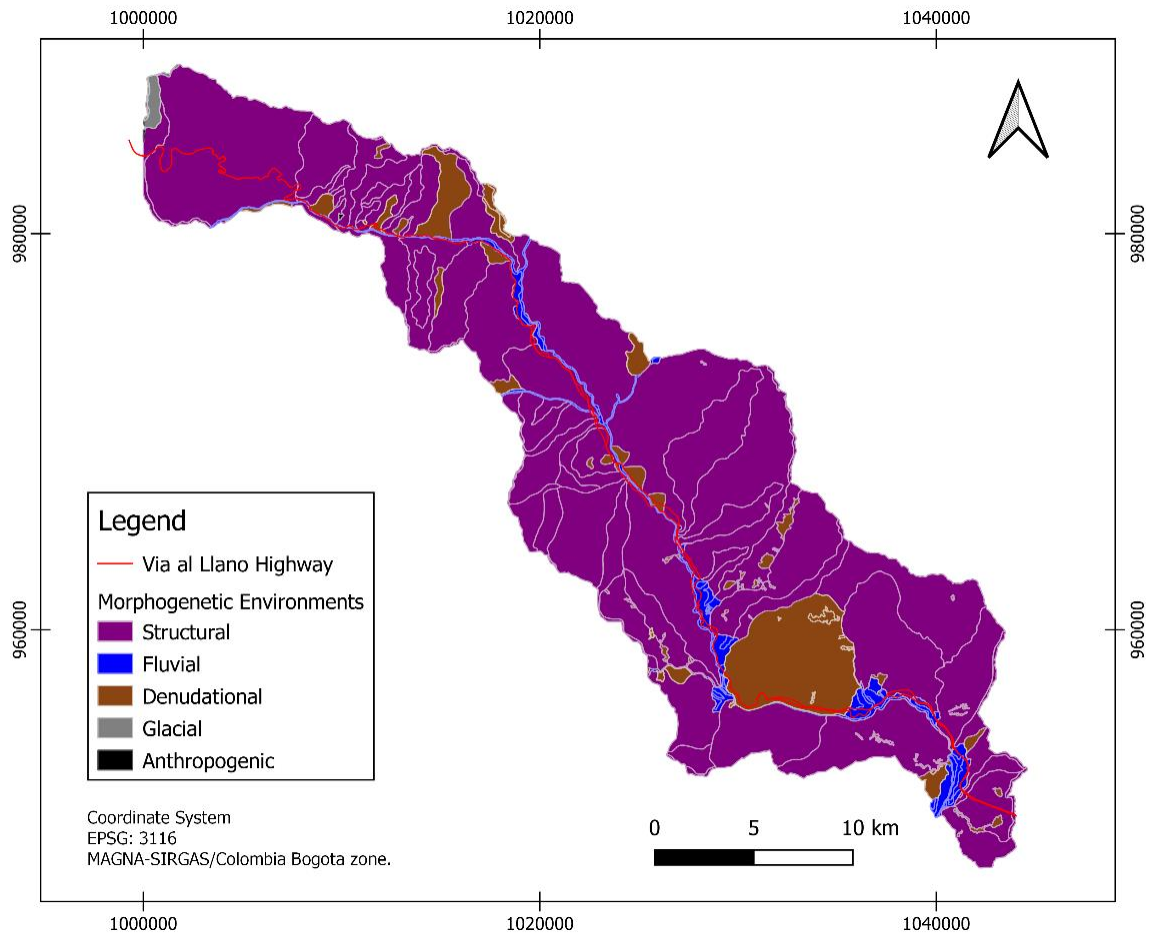


Fig. 11. Distribution of morphogenetic environments in the study area of “Via al Llano” highway. Modified from Servicio Geologico Colombiano & Universidad Pedagogica y Tecnologica de Colombia, (2018a, 2018b).

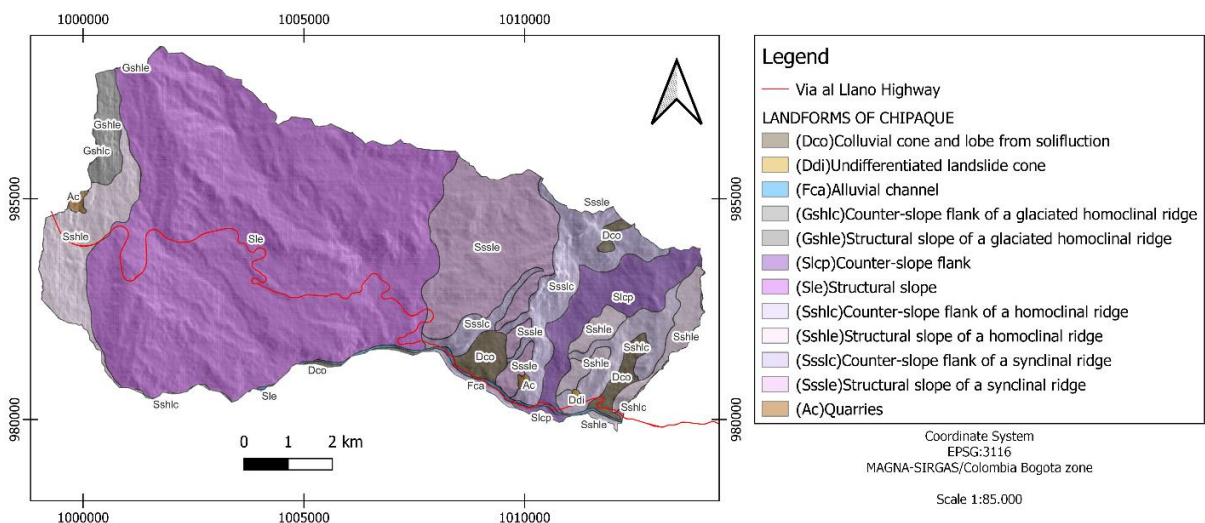


Fig. 12. Map of Landforms in the Municipality of Chipaque. Modified from Servicio Geologico Colombiano & Universidad Pedagogica y Tecnologica de Colombia (2018a).

Table 1. Denudational, Glacial and Anthropogenic landforms in the Study area. Modified from Servicio Geologico Colombiano et al., (2012)

	Acronym	Unit	Definition
Denudational Environment	Dldebl	Denuded ridge system with long length	They are systems or sets of ridges or crests located at different altitudes; with a relative relief index of less than 250 m and the length of the main axis greater than 1000 m; they are elongated forms perpendicular to the main drainage. The top or upper part can have different shapes depending on the degree of drainage incision, the type of saprolite developed by the dominant rock, and the erosive processes that have shaped it. The slope and orientation of the ridge axis can provide information on uplift processes and rates of the mountain range as a whole or the erosion speed of the main river or geomorphological axis
	Dsd	Denuded ridge	Topographic prominence with mountainous and elongated morphology, featuring long to extremely long slopes, concave to convex, with very steep to abrupt slopes, where pronounced erosion or mass movement processes prevail. Its origin is related to pronounced erosion processes in igneous and metamorphic rock substrates
	Dlo	Undulating slope	Sloping surface with hummocky or hilly morphology, inclined to steep slope, varying in length from short to very long. The drainage pattern is subdendritic to subparallel. These slopes can form on residual soils and colluvial deposits.
	Dts	Elevated 'hanging' terraces	Flat or denuded surface with hummocky and hilly morphology, gently inclined slopes that appear as relics of ancient terraces and fluvial landforms, located at a higher elevation than the current riverbed base level. They correspond to areas affected by tectonism or regions where erosion processes are more influential than deposition.
	Dco	Colluvial cone and lobe from solifluction	Structure in the form of a cone or lobe with low hummocky morphology. Its origin is related to processes of transportation and deposition of materials on slopes and due to hydrogravitational processes in saturated and unsaturated soils. Its deposit consists of heterometric blocks and fragments of pre-existing rocks, embedded in a generally clayey to clayey sandy matrix
	Ddi	Undifferentiated landslide cone	Structure in the form of a cone or lobe with low, concave to convex morphology, featuring a stepped slope, semicircular niches, inclined blocks, irregular relief, the formation of cracks, and sudden changes in slope. Its origin is related to mass movements of soil or rock, where displacement occurs predominantly along a fault surface or in areas with high shear deformation.
	Deem	Major erosion scarp	Steep or sheer slope, of variable height, that can be formed by various causes: tectonic, by abrasion (fluvial and marine erosion), by gravitational and glacial processes. It can eventually range from short to long, with a concave, convex, or straight shape, featuring a steep to very steep slope.
	Def	Faceted scarp	Triangular or trapezoidal surface, with a wide base and narrow top, featuring hummocky, concave morphology of short to moderately long length and steep to very steep slopes. Its origin is related to erosion, incision, and mass movements on relict slopes appearing around structural reliefs composed of fractured materials.
Glacial Environment	Gshlc	Counter-slope flank of a glaciated homoclinal ridge	Slopes defined by the inclination of strata against the slope, of moderate to very long length, with concave to irregular stepped forms and steep to very steep slopes locally associated with snow accumulation depressions and glacial cirques. They exhibit sharp ridges (glacial arêtes), glacial cirques, and locally valleys of the same origin, transverse, giving it an irregular appearance in profile. The irregular 'U'-shaped morphology of glacial arêtes is a characteristic feature.
	Gshle	Structural slope of a glaciated homoclinal ridge	Slopes defined by the inclination of strata in the same direction as the slope, ranging from steep to very steep, of moderate to very long length, with concave-convex morphologies and undulating surfaces, and slopes ranging from steep to very steep. They exhibit sharp ridges (glacial arêtes), delimiting glacial valleys in a 'U' shape.
Anthropic Environment	Ac	Quarries	Steep excavation with a height on the order of decimeters, irregularly shaped or terraced on slopes for the extraction of construction materials such as stone, sand, and gravel. This definition includes excavations carried out for the extraction of clays commonly referred to as brick clay pits

Table 2. Structural landforms in the Study area. Modified from Servicio Geologico Colombiano et al, (2012)

	Acronym	Unit	Definition
Structural Environment	Slcp	Counter-slope flank	Sloping surface, with regular to irregular morphology, defined by planes (strata, foliation, jointing, among others) arranged opposite to the slope. It can occur with a long to extremely long length and slopes ranging from gently inclined to steep. In this landform, structural data do not allow establishing an association with any regional-type structure (anticline, syncline, homoclinal, monocline, among others).
	Sle	Structural slope	Sloping surface, with regular to irregular morphology, defined by preferential planes (strata, foliation, jointing, among others) parallel to the slope. It can occur with a long to extremely long length and slopes ranging from gently inclined to steep. In this landform, structural data do not allow establishing an association with any regional-type structure (anticline, syncline, homoclinal, monocline, among others)
	Ss	Mountain range	Topographically prominent mountainous morphology, with long to extremely long, concave, convex, or straight slopes, featuring very steep to escarp slopes. Its origin is related to intense faulting processes in igneous, metamorphic, and sedimentary rock masses. In this landform, the absence of structural data does not allow establishing an association with any structure (anticline, syncline, homoclinal, monocline, among others)
	Ssan	Anticlinal ridge	Elongated topographic prominence with hilly to hummocky morphology, featuring sharp or rounded peaks or crests, limited by structural slopes ranging from inclined to very steep, straight or convex, and of long lengths. The axis of the structure is formed by the arching of strata or layers that diverge in inclination.
	Ssh	Homoclinal ridge	Symmetric or slightly symmetric elongated topographic prominence with mountainous to hilly morphology, featuring sharp peaks, defined by a sequence of stacked and inclined strata or layers (> 35°) in the same direction. Generally, it is the result of the development or erosion of a single flank of a geological structure
	Sshlc	Counter-slope flank of a homoclinal ridge	Moderate to long vertical to subvertical surface, concave in shape, stepped, scalloped, or irregular, with a steep to escarp slope, generated by strata arranged against the slope of the terrain, related to a homoclinal structure
	Sshle	Structural slope of a homoclinal ridge	Surface defined by the inclination of strata in favor of the slope, with short to moderately long length, straight to convex forms, and steep to very steep slopes, related to a homoclinal structure
	Sslp	Compressive ridge and pressure ridge	Ridge with hummocky to elongated topographic prominence, locally curved, associated with compressive zones. Its origin is related to truncation and vertical or lateral displacement due to intense faulting processes
	Ssslc	Counter-slope flank of a synclinal ridge	Short to moderately long vertical to subvertical surface, with convex to irregular stepped shape, featuring a steep to escarp slope, generated by strata arranged against the slope of the terrain, related to the flank of a synclinal structure
	Sssle	Structural slope of a synclinal ridge	Surface defined by strata inclined in favor of the slope of the terrain, with short to moderately long length, concave form, and inclined to steep slopes, related to the flank of a synclinal structure

Table 3. Fluvial landforms in the Study area. Modified from Servicio Geologico Colombiano et al., (2012)

	Acronym	Unit	Definition
Fluvial Environment	Fca	Alluvial channel	Irregularly shaped channel excavated by the erosion of perennial or seasonal flows within rocky masses and/or alluvial sediments. Depending on factors such as slope, bedrock resistance, sediment load, and flow, they can persist for long distances. Straight channels are confined to narrow V-shaped valleys, generally associated with structural control of faults or joints. These channels, when spanning long distances, can form ponds and rapids. When streams flow in semi-flat to flat areas (alluvial plain), channels are meandering or wandering, as a result of sudden changes in flow direction. Depending on the sediment load, slope, and flow, they can form anastomosed, braided, divergent, and other associated systems.
	Fpi	Floodplain	Surface with flat to low undulating morphology, eventually prone to flooding. It is located bordering river channels, locally limited by terrace scarps. It includes minor river plains in 'U' or 'V' shapes, as well as minor colluvial cones on the flanks of intramontane valleys. In mountainous regions, where river channels tend to merge with their tributaries to form the main channel, in a sub-parallel drainage network of medium density, they appear as narrow, elongated, and deep surfaces.
	Fta	Accumulation terrace	Elongated surface, flat to gently undulating, shaped over alluvial sediments, appearing in paired form, limited by scarps of different heights along the course of a river. Its origin is related to processes of erosion and alluvial accumulation within ancient floodplains. Its formation includes phases of accumulation, incision, and vertical erosion. These terraces can be part of meandering straight channels. Their deposit consists of gravel, sand, silt, and clay, with a decrease in size as one moves away from the river channel.
	Ftae	Escarpment of accumulation terrace	Vertical to subvertical, stepped plane excavated in alluvial sediments bordering accumulation terraces. Its origin is related to the incision and deepening of the channel. The height of the scarps can reach tens of meters.
	Ftb	Tilted terrace	Flat to gently inclined surface, a remnant of an eroded, tilted, and/or folded terrace, with gently undulating morphology and inclinations between 5° to 10° in the upper parts, limited by scarps of varying height. Its origin is related to processes of uplift and tectonic folding affecting the bedrock.
	Ftbe	Escarpment of tilted terrace	Vertical to subvertical plane of short lengths, stepped, excavated in alluvial sediments bordering tilted accumulation terraces. Its origin is related to the incision and deepening of the channel in these terraces. The height of the scarps can reach tens of meters.

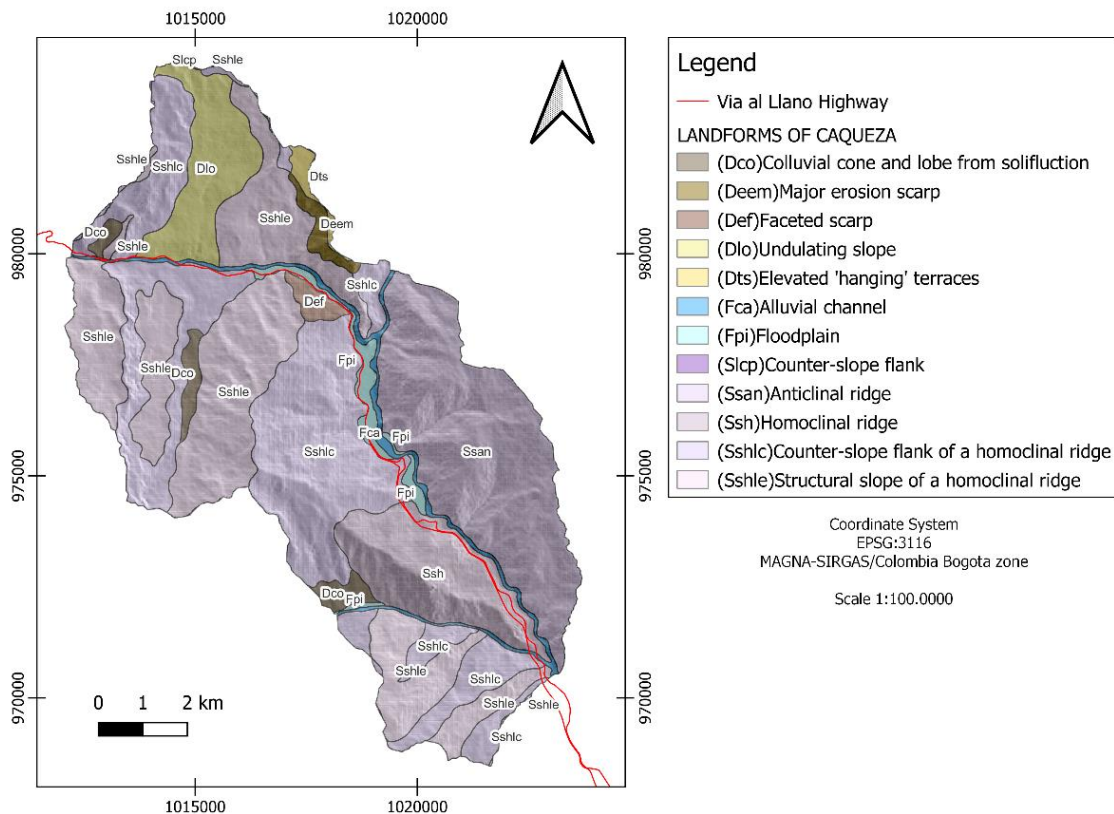


Fig. 13. Map of Landforms in the Municipality of Caqueza. Modified from Servicio Geologico Colombiano & Universidad Pedagógica y Tecnológica de Colombia (2018a).

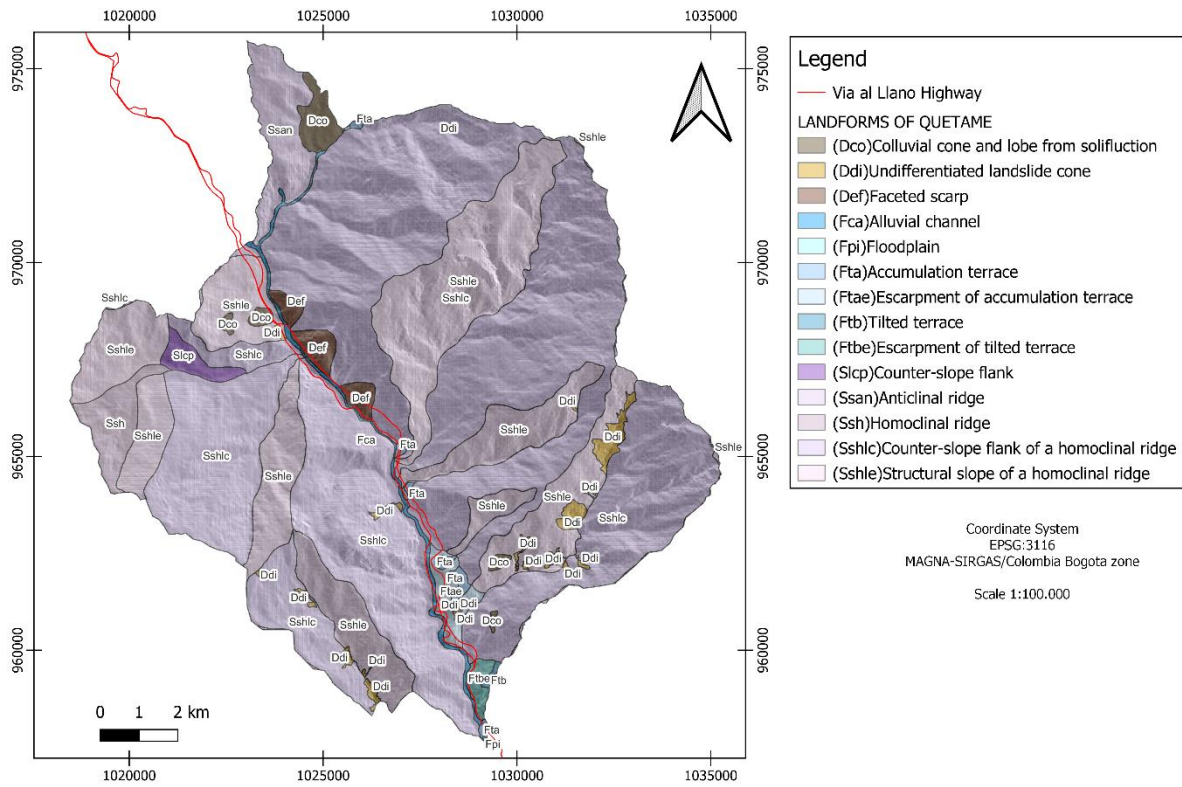


Fig. 14. Map of Landforms in the Municipality of Quetame. Servicio Geologico Colombiano & Universidad Pedagogica y Tecnologica de Colombia (2018b).

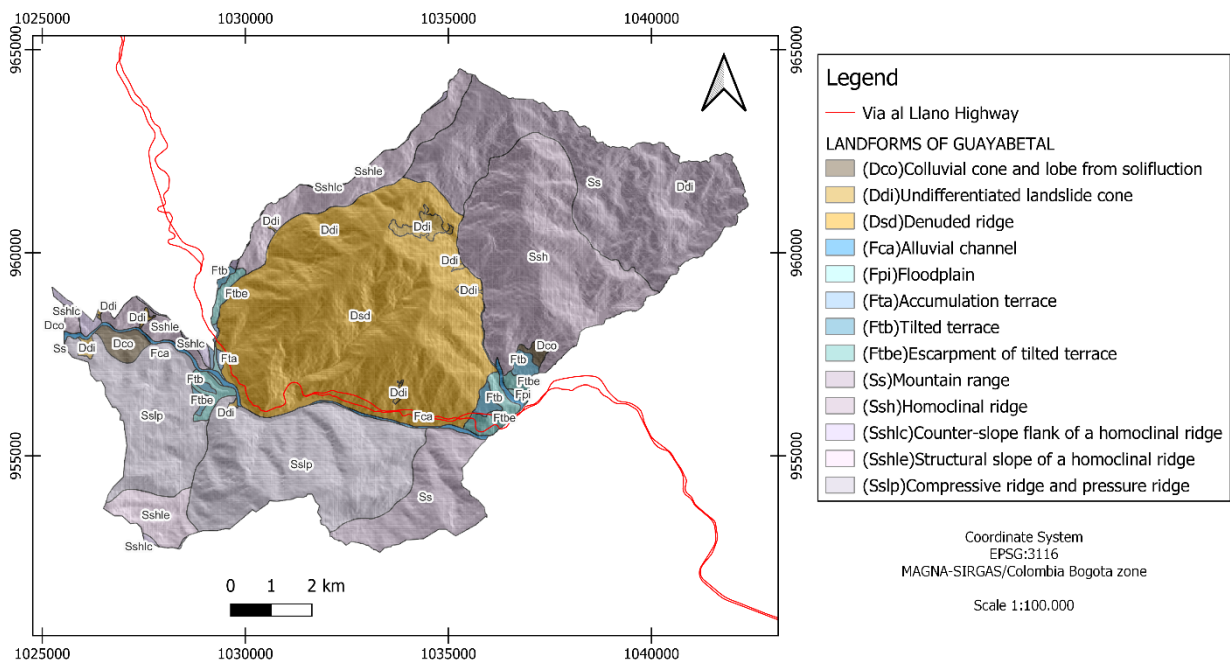


Fig. 15. Map of Landforms in the Municipality of Guayabetal. Servicio Geologico Colombiano & Universidad Pedagogica y Tecnologica de Colombia (2018b).

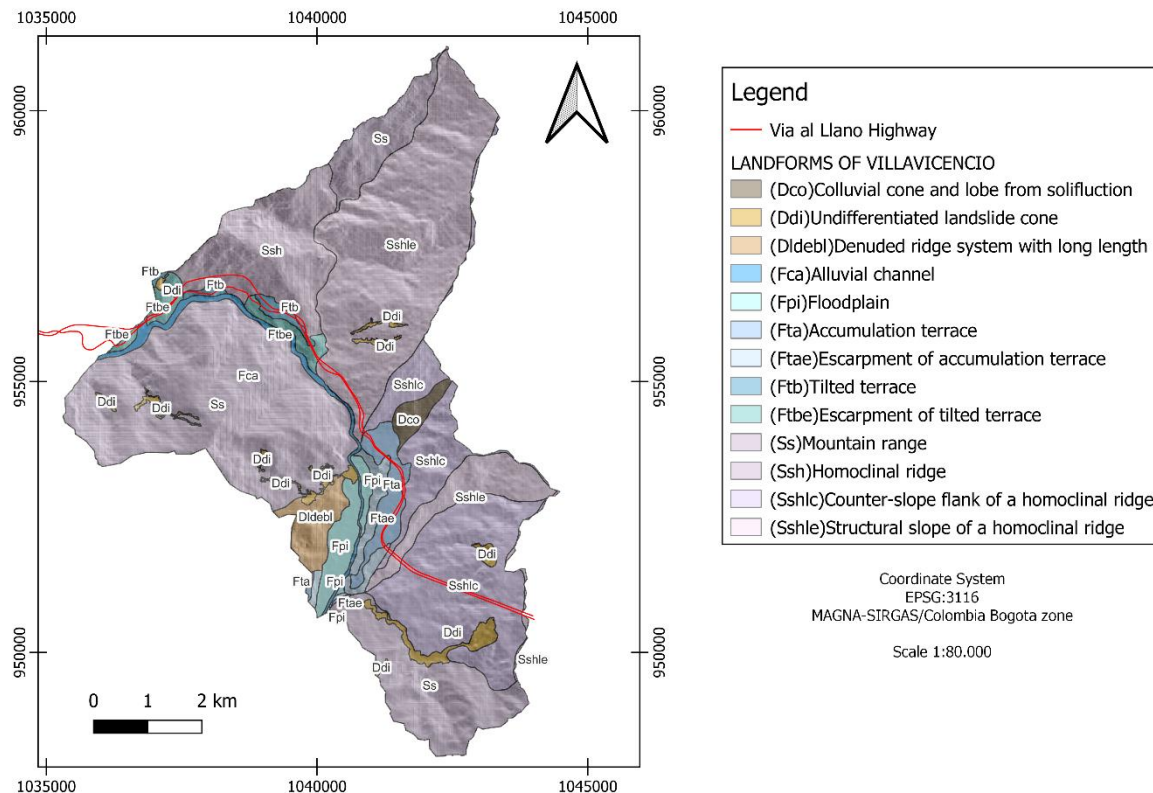


Fig. 16. Map of Landforms in the Municipality of Villavicencio. Modified from Servicio Geologico Colombiano & Universidad Pedagógica y Tecnológica de Colombia (2018b).

2.4. Historic landslides

The Colombian Geological Service (SGC) has developed a digital platform that includes a huge catalog of mass wasting phenomena that have occurred in Colombia. This platform is known as the “*Sistema de información de Movimientos en Masa*” (SIMMA). The database is subdivided by municipalities (the political subdivision of Colombian states). For each municipality, there is a multi-temporal inventory of landslides that have occurred in the last 70 years, indicating the type of movement, their location, the date, and additional information. The latest update of the available inventory shapefile was in 2020 (Servicio Geologico Colombiano, 2020). According to the inventory, 377 landslides were identified. Of these, 206 were located in the municipality of Caqueza, making it the municipality with the highest number of recorded landslides. (Table 4). Additionally, according to the database, the most frequently type of landslide was slides, followed by falls (Table 4). The period with the highest quantity of landslides was between 2015 and 2020 (Table 5).

Another source of landslides event data is the National Unit of disaster Risk Management, or *Unidad Nacional para la Gestión del Riesgo de Desastres* (UNGR). This database includes information on mass movements that directly affect the population. While this database provides a description the situation, it does not contain specific information about the type of movement or the exact location with coordinates. Between 2017 and 2023, 42 emergency cases due to landslides was recorded in the study area (Table 3). The year with the most mass movements was 2011 and the municipality with the most frequent and consistent landslides between 2017 and 2023 was Quetame (Table 6).

According to news or public information there are certain areas along the highway that are highly susceptible or prone to landslide (RCN Radio, 2018). These areas are identified by the number of kilometers between Bogota, from 0 to 86 in Villavicencio. The most well-known critical zones are located at 4 km, 26 km, 46 km, 51 km, 52 km, 55 km, 56 km, 58 km, 60 km, 62 km, 63 km, 64 km, 65 km, 68 km, 70 km (RCN Radio, 2018) (Fig. 17).

Table 4. Type of landslide on the study area from SIMMA database.

Type	Study Area	Chipaque	Caqueza	Quetame	Guayabetal	Villavicencio
Slide	138	18	50	45	13	12
Fall	108	0	81	16	9	6
Soil Creep	67	5	60	1	0	1
Flow	52	5	15	12	11	8
Topple	12	0	0	8	1	0
TOTAL	377	28	206	82	34	27

Table 5. Date of landslides from SIMMA database.

Date (year)	Study Area	Chipaque	Caqueza	Quetame	Guayabetal	Villavicencio
1960-2000	12	10	0	2	0	0
2001-2005	9	0	0	9	0	0
2006-2010	23	4	0	14	5	0
2011-2015	49	3	31	8	7	0
2016-2020	51	2	4	28	17	0
No data	233	9	171	21	5	27
TOTAL with data	144	19	35	61	29	0

Table 6. Date of landslides from UNGR database.

Date UNGR	Study Area	Chipaque	Caqueza	Quetame	Guayabetal	Villavicencio
2017	8	1	0	4	1	2
2018	7	1	2	1	3	0
2019	3	0	0	2	1	0
2020	3	0	1	2	0	0
2021	11	0	4	2	0	5
2022	6	0	3	1	0	2
2023	4	0	1	3	0	0
TOTAL	42	2	11	15	5	9

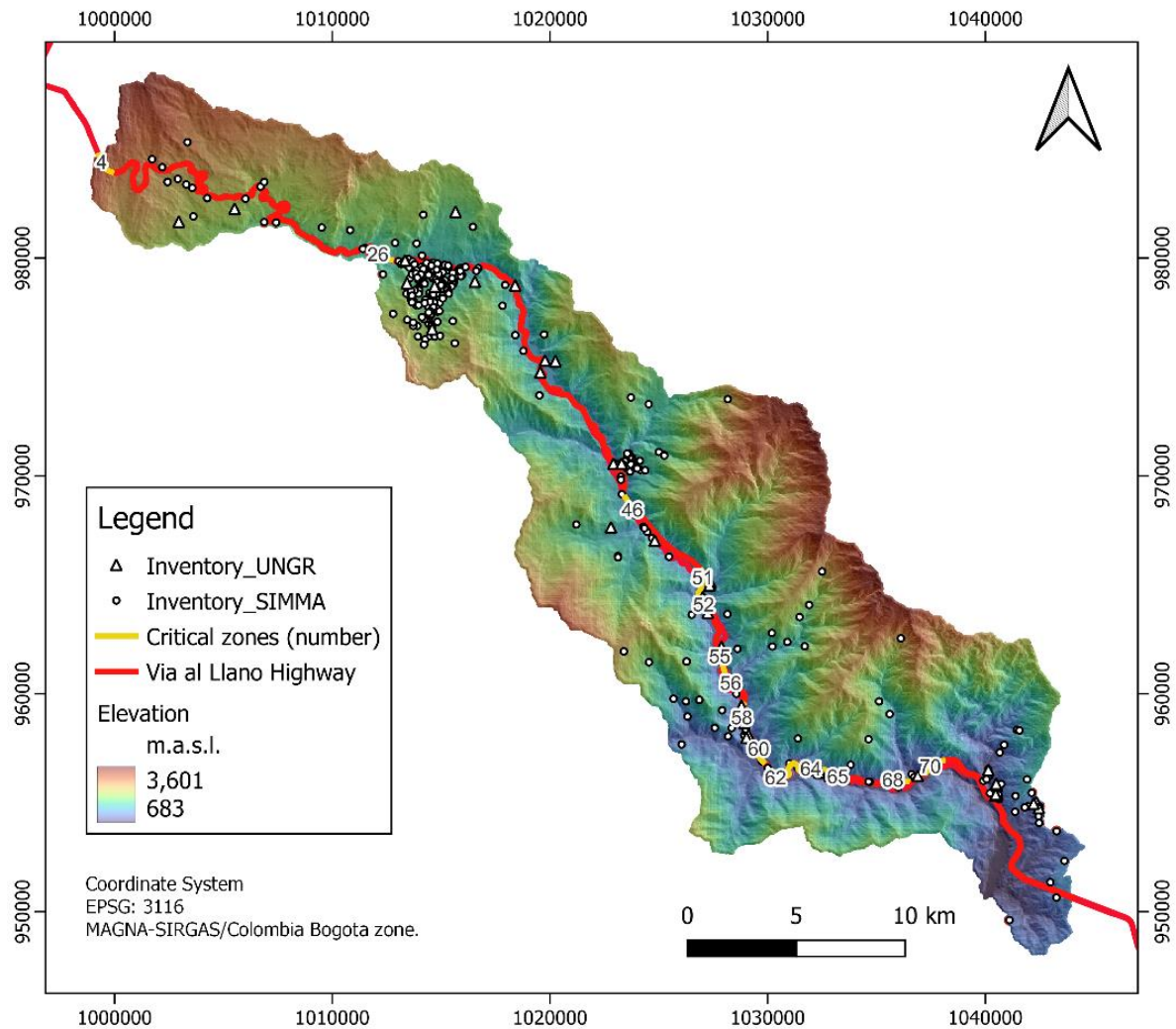


Fig. 17. Map of mass movements from SIMMA and UNGR on the “Via al Llano” highway. The numbers over the road indicate the respective kilometer of each critical zone, starting from kilometer 0 in Bogotá and ending at kilometer 86 in Villavicencio.

According to the historical inventory obtained by SIMMA and UNGR, a total of 419 landslides have been identified (Fig. 17). In the Chipaque area, the predominant landslides are “slides” that are located on the south side of the road near the urban area of Chipaque, and on the north side near to Abásticos. “Flows” and “soil creep” prevail in the central area south of the road (Fig. 18). Although areas at kilometer 4 and 26 have been identified as critical, no points from the inventory are observed in these areas.

In the Cáqueza area, the largest number of landslides is found in the urban area, with a significant prevalence of “fall” type landslides, followed by “soil creep” and “flows” (Fig. 19). In the southern part of the area, specifically around Puente Quetame, “topples” have been recorded. In the rest of the area, especially in the central part and near the urban area of Cáqueza and El Tablon, “slides” have occurred (Fig. 19). The kilometer 26 near the urban area of Cáqueza is the only critical point on the road mentioned by the media.

In the Quetame area, numerous mass movements are observed on and near the road, mainly of the "slide" type (Fig. 20). In the urban area of Quetame, a wide variety of landslides are grouped, including "flows", "topples," and "slides". Most "fall" type landslides are found in high and remote areas from the road. Six critical points have been identified, with kilometer 58 being the most unstable since 2019, when a landslide completely covered the road (Fig. 20).

In the Guayabetal area, "slide" is the type of mass movements predominate in the urban area (Fig. 20). "Flows" and "falls" have been recorded on the road, while "slides" prevail in the high areas north of the road (Fig. 21). There are 6 critical areas of the road in this municipality, corresponding to kilometers 60, 62, 63, 64, 65, and 68. Kilometer 64 has been the most unstable since 2017, presenting "falls" and "slides" (Fig. 21).

Finally, in the Villavicencio area, the old road to the Llano has been the most affected. Continuous mass movements from Servita to the Pipiral area have affected populations and transporters using this road (Fig. 22). The most prominent mass movement occurred in 2017 on the road near the urban area of Servita. This can be easily observed in satellite images from 2018 onwards.

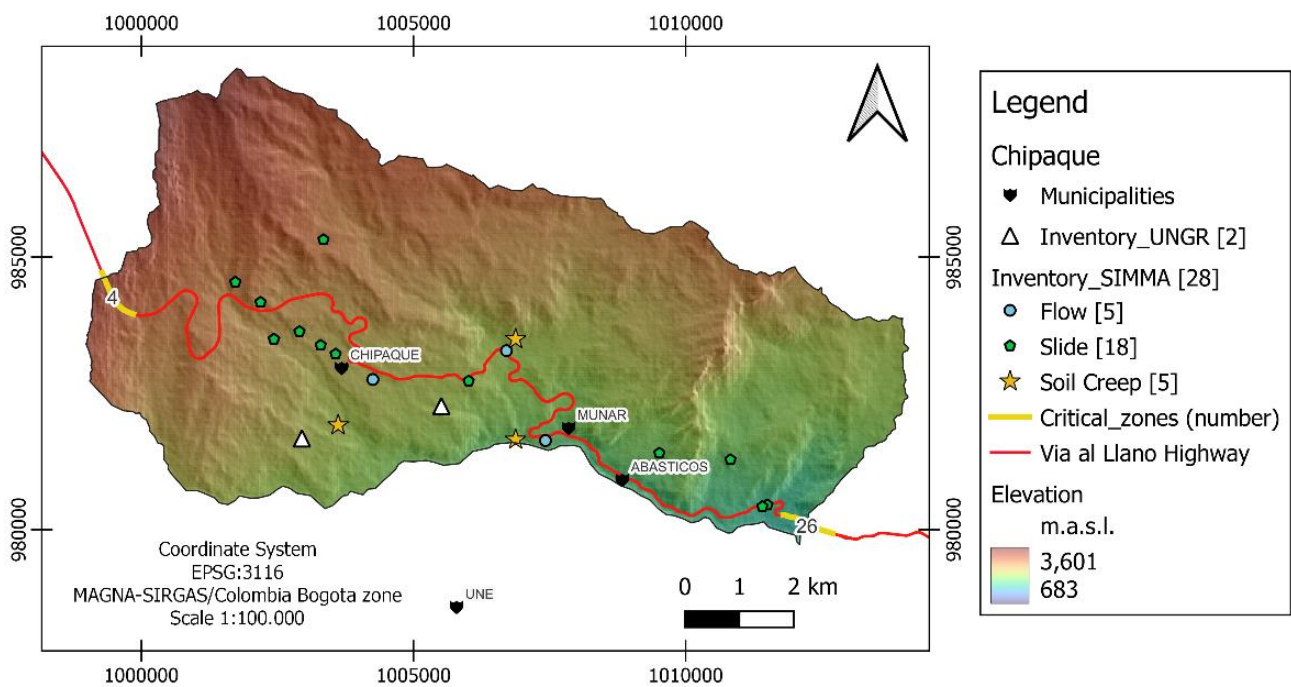


Fig. 18. Map of mass movement events in the municipality of Chipaque, obtained from SIMMA and UNGR.

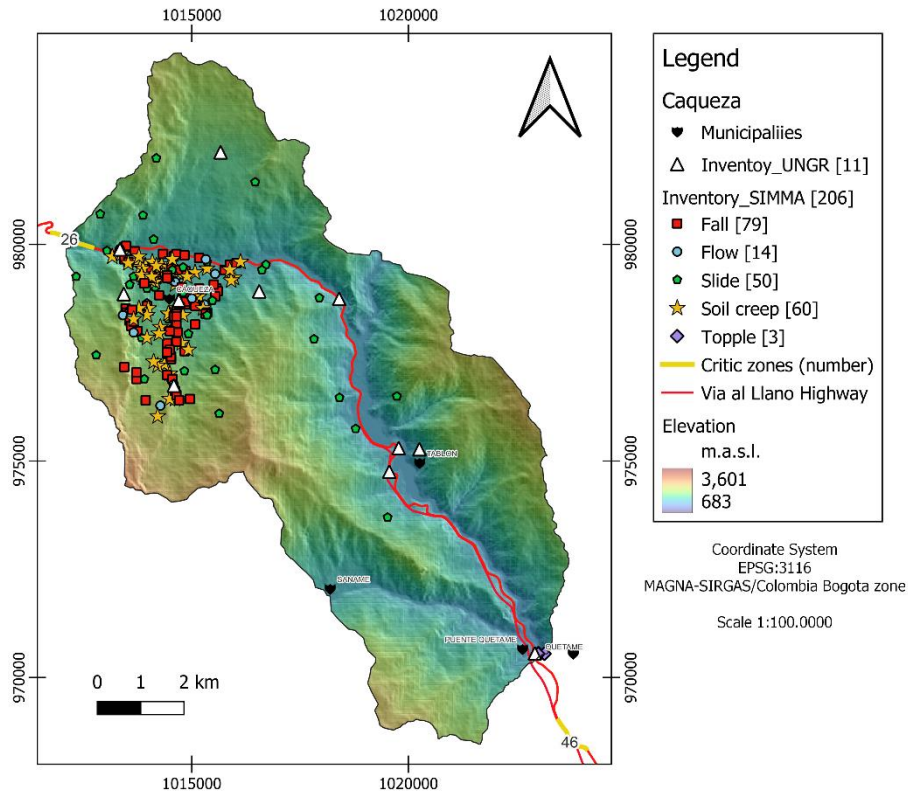


Fig. 19. Map of mass movement events in the municipality of Caqueza, obtained from SIMMA and UNGR.

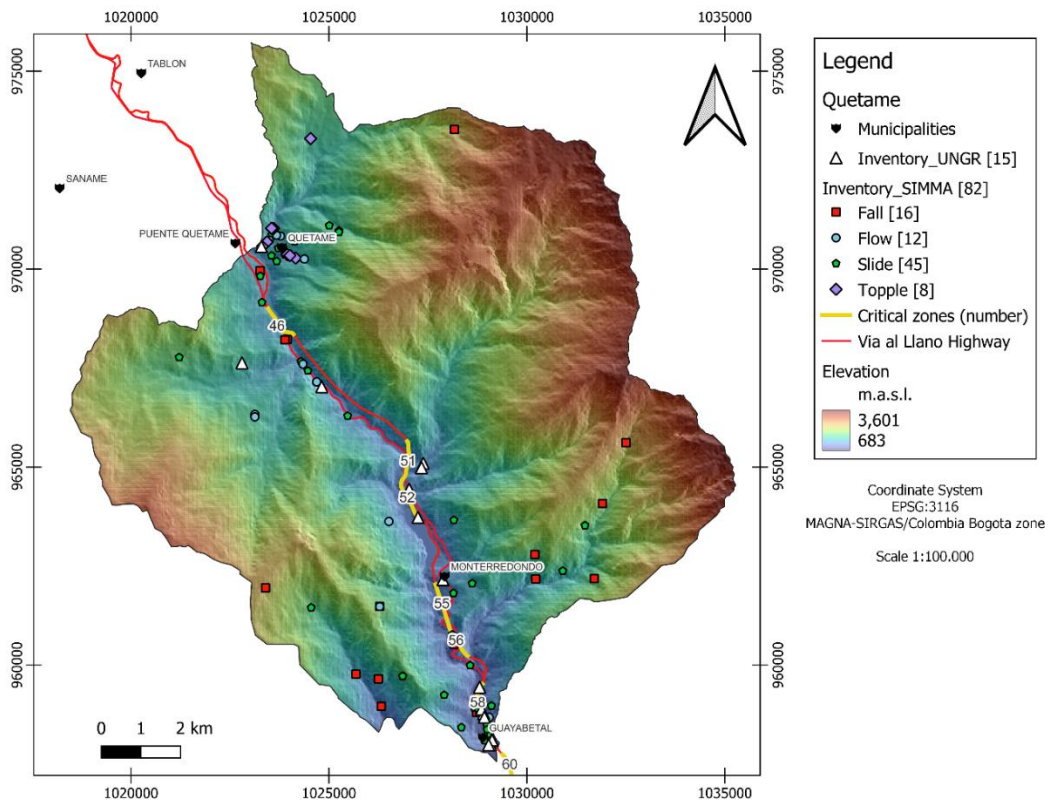


Fig. 20. Map of mass movement events in the municipality of Quetame, obtained from SIMMA and UNGR.

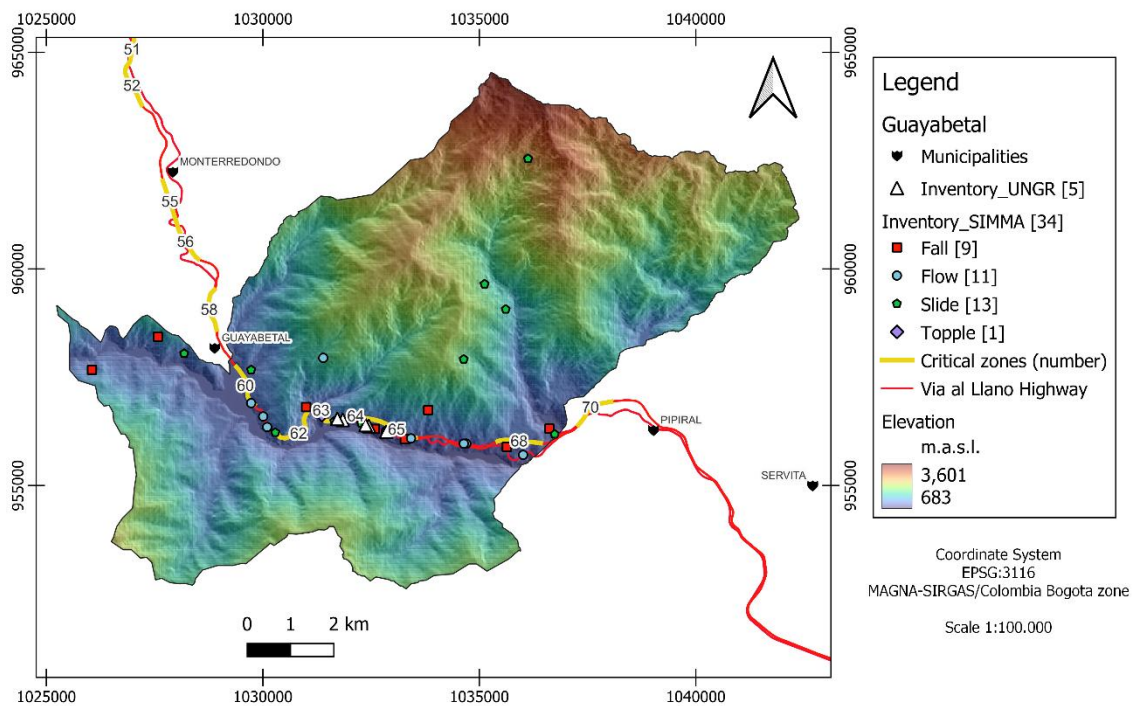


Fig. 21. Map of mass movement events in the municipality of Guayabetal, obtained from SIMMA and UNGR.

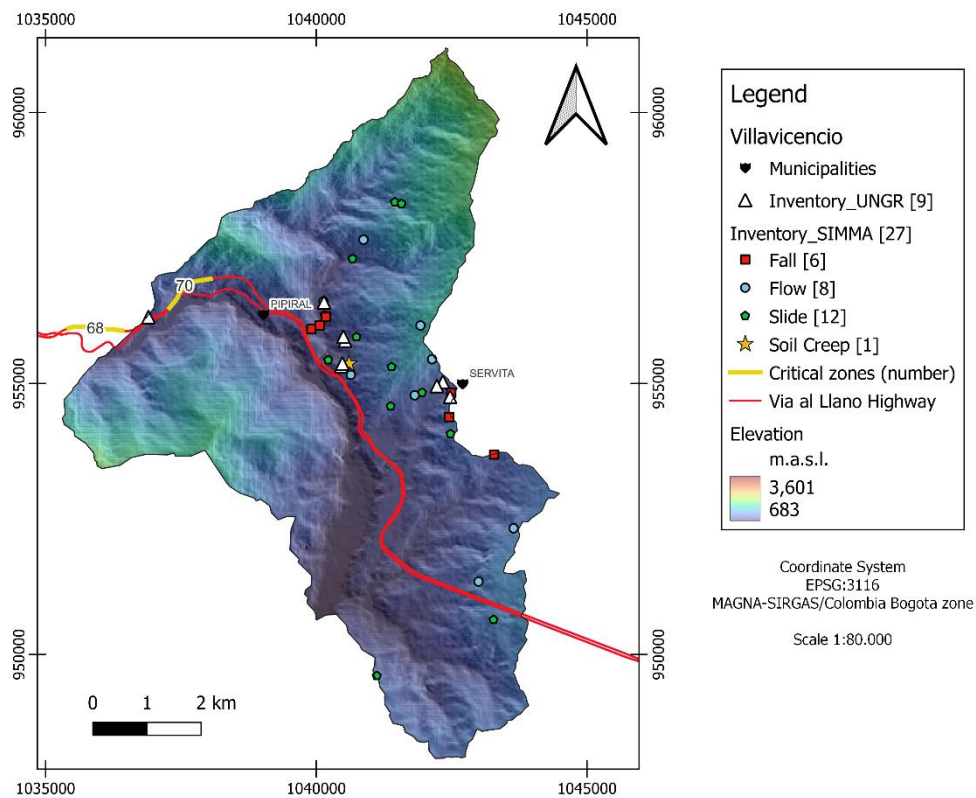


Fig. 22. Map of mass movement events in the municipality of Villavicencio, obtained from SIMMA and UNGR.

2.5. Previous landslides susceptibility studies in the study area

In the study area, various susceptibility and hazard studies for mass movements have been conducted through different methodologies. Published and publicly available works cover from the year 2010 to the present, addressing different challenges and yielding diverse results. Below, we will explore the nine most relevant works that have contributed to the advancement and development in the study area.

The analysis carried out by INGEOMINAS and IDEAM in 2010 resulted in the publication of the national map of Relative Hazard for mass movements at a scale of 1:500,000. Within this study, the segment corresponding to the road to Llano covers sheets 5-09 and 5-14 (Fig. 23). In sheet 5-09, which includes municipalities from Chipaque to Quetame, an orange shade indicates a "High" hazard of landslide (Fig. 23-A). Further along, between the areas of Quetame and Guayabetal, small areas with red shading are identified, indicating a "Very High" hazard of landslides (Fig. 23-A). Similarly, in sheet 5-14, encompassing the municipalities of Guayabetal and Villavicencio, the entire area shows a red shade, suggesting a "Very High" hazard (Fig. 23-B).

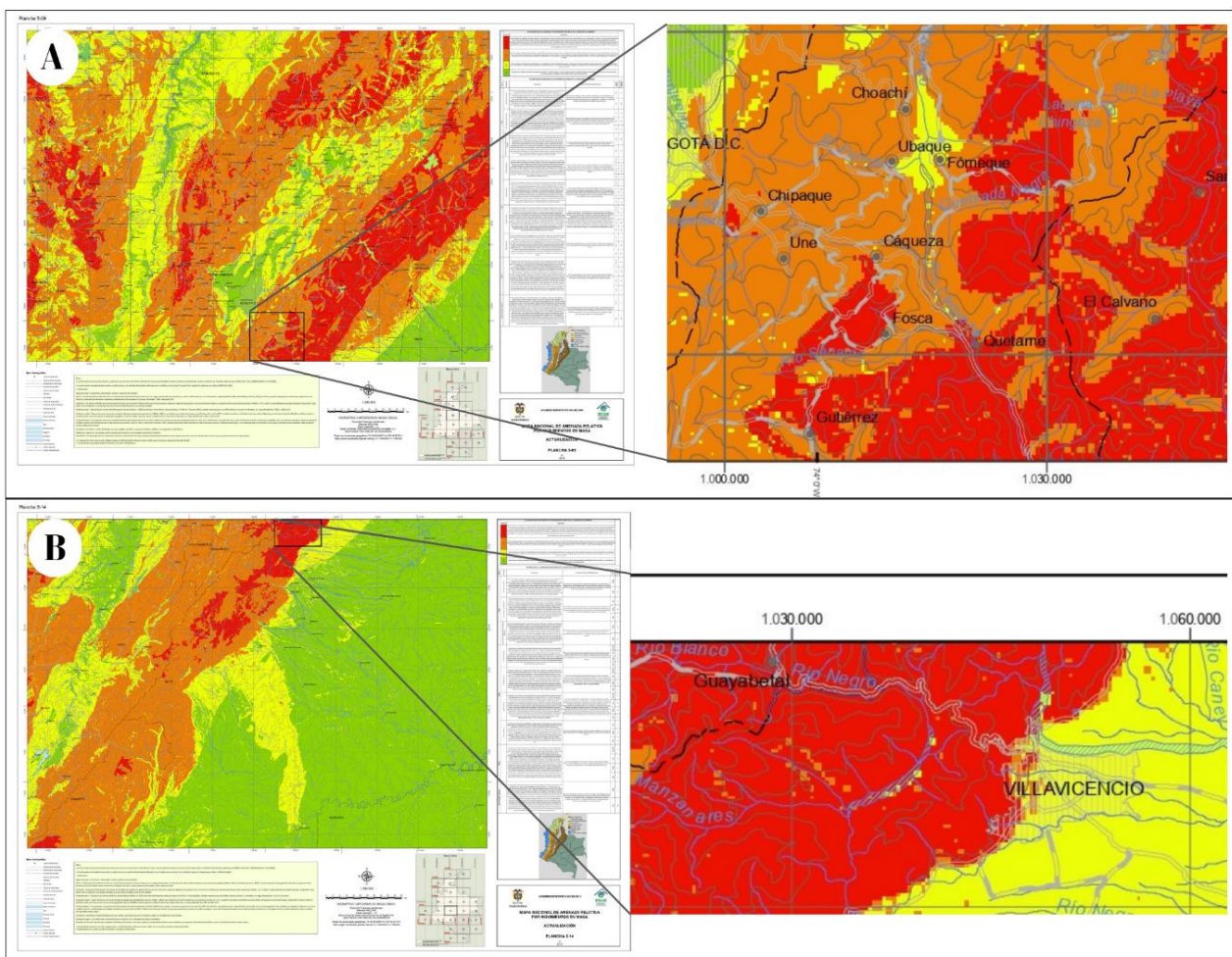


Fig. 23. Maps of Relative Hazard for mass movements, obtained from INGEOMINAS and IDEAM (2010). (A) Sheet 5-09, scale 1:500,000. (B) Sheet 5-14, scale 1:500,000.

In 2011, Sánchez and Urrego presented in their Civil Engineering thesis the hazard area in a section of the "Vía al Llano" highway, using rainfall intensity values and relying on a terrain susceptibility map (Fig. 24-C). The latter was obtained by them through a heuristic method that combines various terrain variables such as slope, deposit characteristics, land cover type, and distance to faults. As a result, two hazard maps for deep and shallow landslides were generated in the study area (Fig. 24-A and B), along with a terrain susceptibility map (Fig. 24-C). This study area covers the stretch between kilometers 50 and 63.

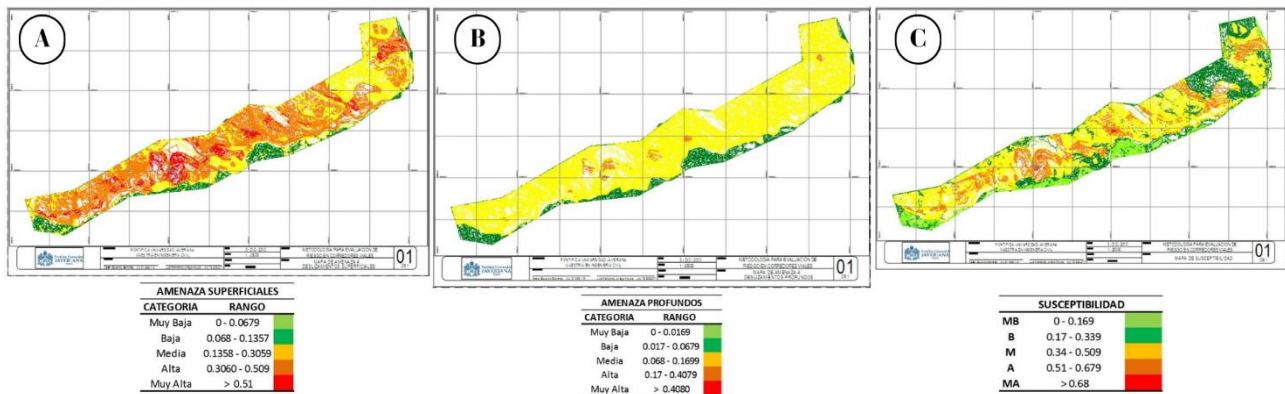


Fig. 24. Maps of Hazard for landslides and Susceptibility terrain, obtained from Sanchez & Urrego (2011). (A) Hazard map of shallow landslides. (B) Hazard map of deep landslides. (C) Susceptibility Terrain Map.

Ramírez (2012) carried out a compilation and analysis of geotechnical research conducted at the National University of Colombia. Among these investigations, two of 192 were distinguished because they focus on the area of the "Vía al Llano". The first, conducted by Rodríguez, (2001) is focuses on evaluating the stability of certain landslides located in the Municipality of Cáqueza along the "Vía al Llano". In this study, a probabilistic analysis was carried out to evaluate the resistance and seismic acceleration of each sector. Subsequently, Díaz (2002) conducts a hazard study of mass movements in the initial section of the "Vía al Llano" road. In this work, different types of landslides were identified, including landslides and rotational slides. It is noted that, in most of the slopes studied, there is a medium hazard of mass movements. The results of these investigations were not available on the web.

Ruiz et al. (2018), carried out a study as part of the agreement between the "Servicio Geológico Colombiano (SGC)" and the "Instituto Geográfico Agustín Codazzi (IGAC)", resulting in the creation of a landslide hazard map at a scale of 1:25,000 in an area belonging to the municipality of Villavicencio (Fig. 25). Additionally, maps of surface geological units, geomorphological subunits, and land cover and land use were generated. To determine the zoning of landslide susceptibility, the bivariate method was employed, considering triggering variables such as rainfall and seismicity, along with other geo-environmental variables. This study identified 646 landslides, with rotational slides and flows being the most predominant. Furthermore, a hazard map was generated for the area from Pipiral to Servita (old road of Via al Llano), providing valuable information for our study. This map belongs to sheet 266-II-A (Fig. 25).

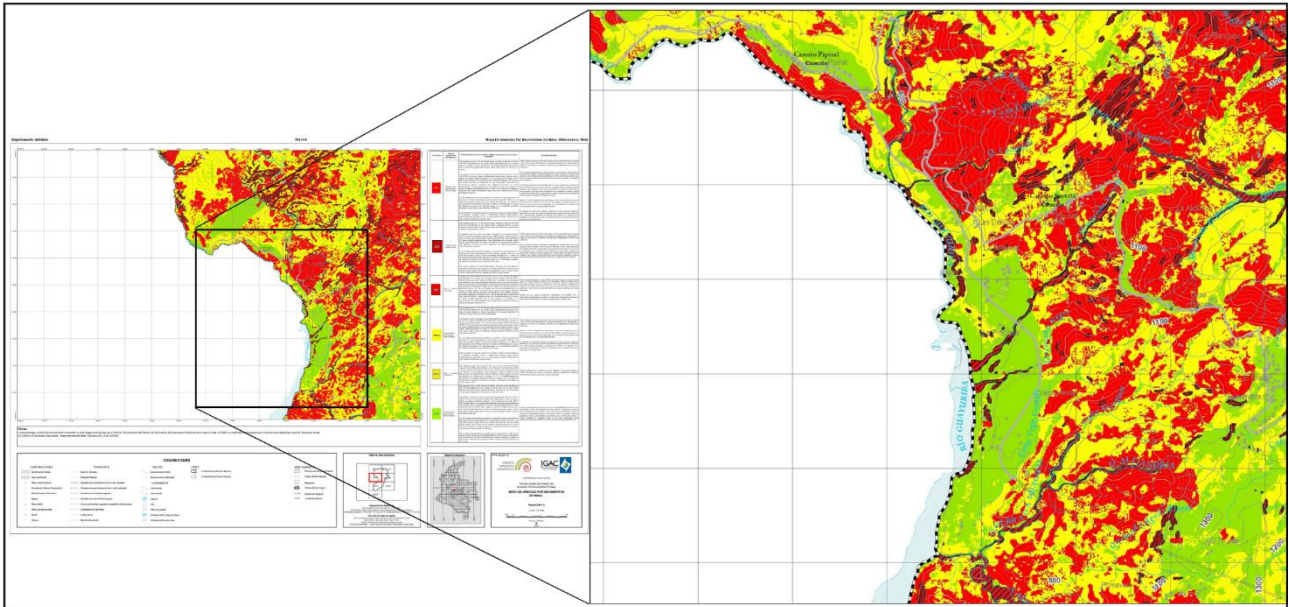


Fig. 25. Landslide hazard map at a scale of 1:25,000, sheet 266-II-A, from SGC and IGAC (2018).

Navarro et al. (2019) produced geological, geomorphological, and geological hazard maps at a scale of 1:100,000 for the affected area around kilometer 58 on the “Via al Llano”. This was done to support decision-making processes of state entities facing this impact. They include information on seismicity, tectonic analysis of the area, landslide inventory available in SIMMA, as well as hydrodynamic modeling of the Rio Negro and maps of flash flood hazards in the Rio Negro River basins. In this work, they concluded that hazard maps for mass movements across the entire area had already been generated in 2016, and the area has a high level of susceptibility to landslides. Furthermore, it was identified that the slope at kilometer 58 is an old terrace with low cementation. They recommended to assess the causes leading to its destabilization, especially the increase in water or moisture within it.

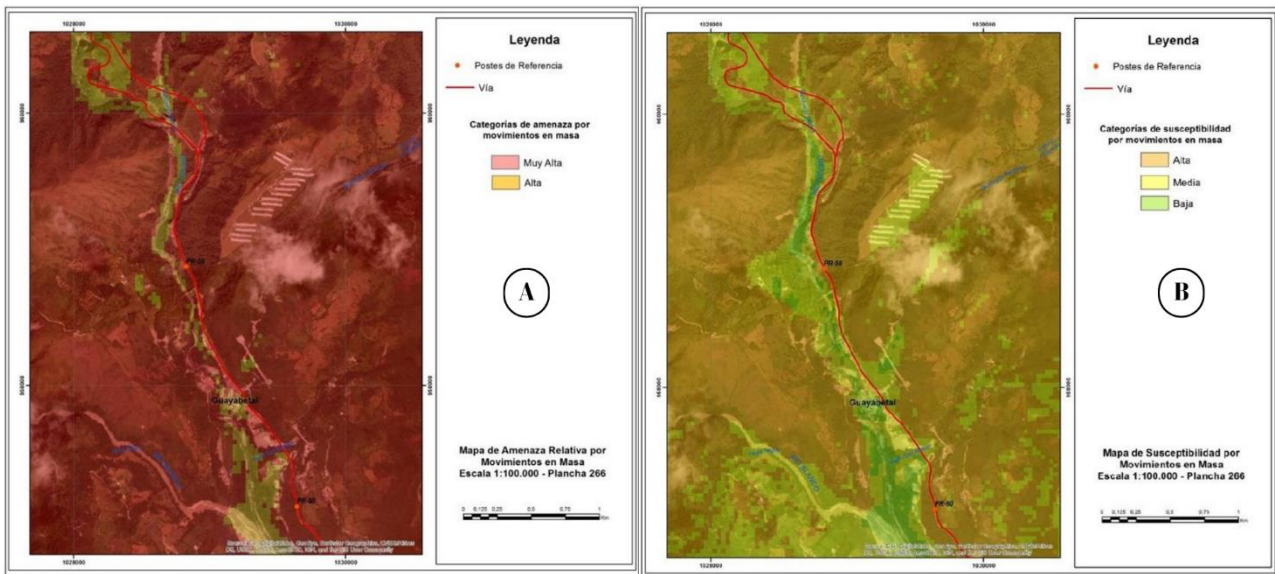


Fig. 26. (A) Landslide hazard map at a scale of 1:100,000, sheet 266. (B) Landslide Susceptibility map at a scale of 1:100,000, sheet 266. Taken from Navarro et al. (2019).

In her engineering thesis conducted in 2019, Pineda focused on the hazard area in the Servita sector (old road to Llano), located within the municipality of Villavicencio. This thesis proposes engineering solutions to address the effects of a debris flow that affected both the road and the population in 2017. Additionally, the thesis concluded that the triggering factor of this landslide was the increase in precipitation during that year. The author also emphasized that ground vibrations caused by vehicular traffic and constructions in the area are significant conditioning factors to consider. Furthermore, Pineda (2019) determined that 80% of the study area is affected by soil creep and that there is a high threat in the zone (Fig. 27).



Fig. 27. The landslide classification in the area of Servitá, from Pineda (2019).

Chaparro et al. (2020) carried out a heuristic analysis of landslide inventories located in Mocoa, Cajamarca, Villavicencio, and Popayán, relating them to four predictor variables: lithology, slope, relief, and frequency-area distribution. In the Villavicencio area, they primarily focused on the zone affected by the Servitá Fault. Although this area is not well-defined, it covers approximately 294.6 km². During the analysis, 334 "slide" type landslides were identified. Additionally, they observed that most of these landslides commonly occur in residual soils.

Calderón-Guevara et al. (2022) conducted a landslide susceptibility study using statistical and machine learning methods. This work was carried out on the southeastern side of Cundinamarca department and the northwestern side of Meta department, encompassing the entire area of the "Via al Llano". The authors utilized geological, topographic, hydrological, anthropic, and soil cover factors as variables, and performed modeling using the Weight of Evidence (WOE), Artificial Neural Networks (ANN), Gradient Boosted Regression Trees (GBRT), and Random Forest (RF) methods. While generally distinguishing landslides between soil translational, rock wedge, and soil rotational slide, all of these were collectively selected for prediction in the area. The quality of the four methods was compared, and Random Forest emerged as the most effective method due to its higher prediction accuracy with an ROC value of 93.73%, followed by Artificial Neural Network. The latter was effective using both categorical and continuous variables, while the other three remaining models performed better using only continuous variables. The landslide susceptibility map obtained with Random Forest is shown in Fig. 28.

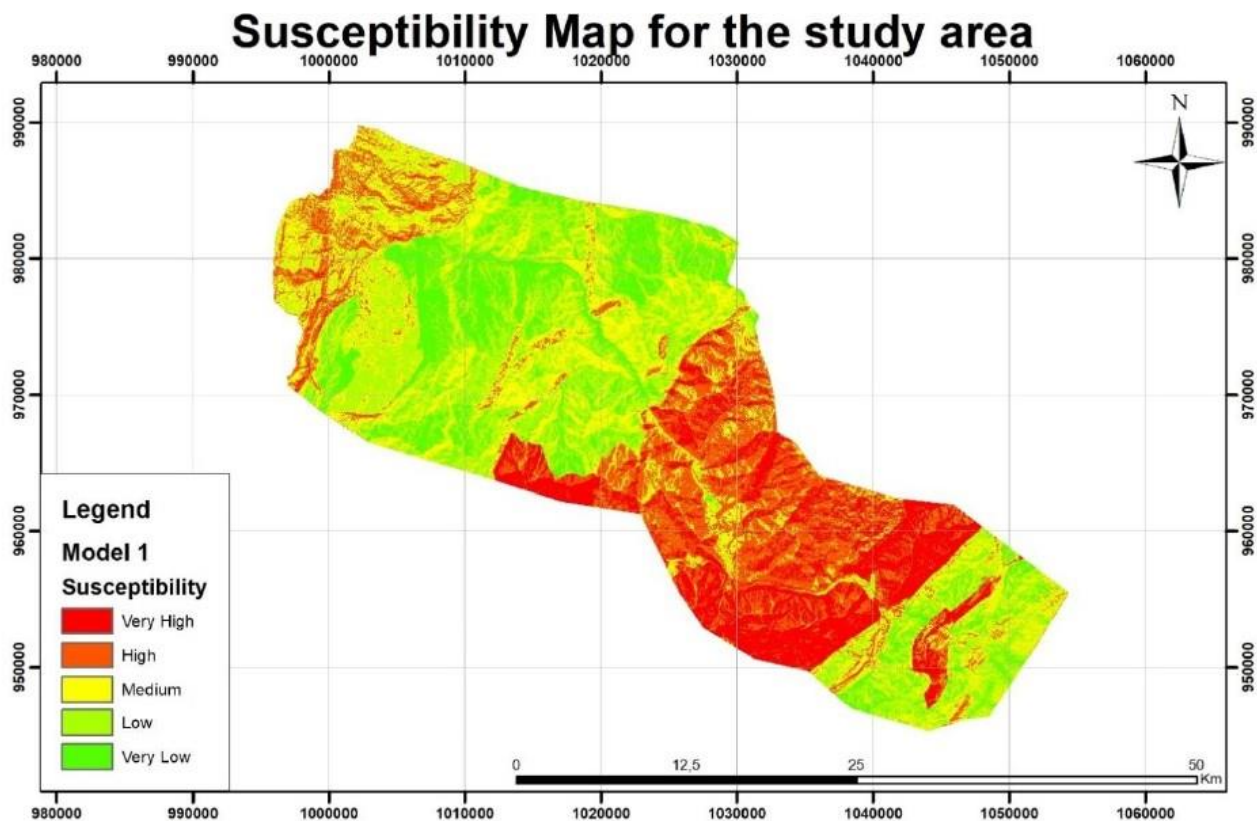


Fig. 28. Landslide susceptibility map from Calderón-Guevara et al., (2022).

Herrera-Coy et al. (2023) conducted a landslide susceptibility model focusing on the area encompassing the Bogota-Villavicencio Highway or Via al Llano. To develop this model, they first obtained an inventory of 2506 landslides, differentiating them into 5 typologies: "debris avalanches", "debris flows", "slides", "earth flows", and "soil creep". They distinguished that debris flows and debris avalanches mainly occur in metamorphic materials, areas with sparse vegetation, steep slopes, and the lower sections of hillsides. Meanwhile, "slides", "earth flows", and "soil creep" primarily occur in Cretaceous mudstones, cultivated lands/pastures, medium to low slopes, and lower and middle sections of hillsides. The modeling methods used were discriminant analysis, random forest, neural networks, and matrix. They concluded that modeling obtained with machine learning, specifically random forest, was the most appropriate due the prediction accuracy exceeding 90%. They generated two landslide susceptibility maps: one for shallow movements, which corresponds to debris flows and debris avalanches (Fig. 29-a), and the other for deeper movements, corresponding to slides, earth flows, and creep processes (Fig. 29-b). The resulting maps in the area revealed a strong geological influence on susceptibility estimation.

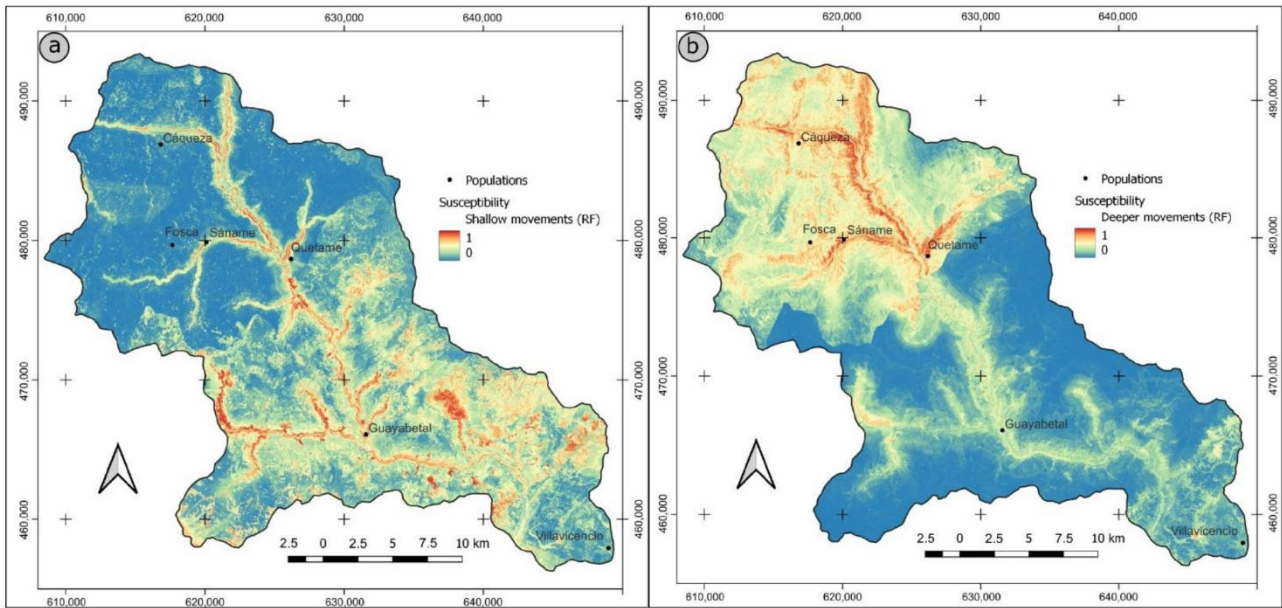


Fig. 29. (a) Landslide susceptibility maps of shallow movements. (b) Landslide susceptibility maps of deeper movements. Taken from Herrera-Coy et al. (2023).

2.6. Pluviosity

In 2017, IDEAM released a compilation of meteorological data for Colombia, based on historical information covering from 1981 to 2010. This Climatological Atlas describes each meteorological variable spatially and temporally across the Colombian territory. The majority of the "Via al Llano Highway" is in the department of Cundinamarca, passing through the municipalities of Chipaque, Cáqueza, Quetame, and Guayabetal, and only entering the department of Meta in the municipality of Villavicencio in its final kilometers. Therefore, the meteorological information for this area encompasses parts of both departments.

It is important to note that the "Via al Llano," starting in the municipality of Chipaque at an approximate altitude of 2,500 meters above sea level, and gradually descends to an altitude of approximately 500 meters above sea level in the municipality of Villavicencio (Fig. 2). Being in the equatorial zone, Colombia receives nearly the same amount of solar energy throughout the year, resulting in uniform temperatures with little variation. The temperature fluctuates within a range of 1 to 3°C, with the average temperature being mainly influenced by the altitude of the site above sea level, among other related factors (IDEAM, 2017). Accordingly, the municipality of Chipaque experiences temperatures ranging between 8-12°C in its western part and 12-16°C in the eastern part (Fig. 30-A). Subsequently, the municipalities of Cáqueza and Quetame present a temperature range between 16-20°C (Fig. 30-A). Then, in Guayabetal, the temperature range increases to 20-22°C, and in Villavicencio, the area reaches temperatures between 22-24°C (Fig. 30-B).

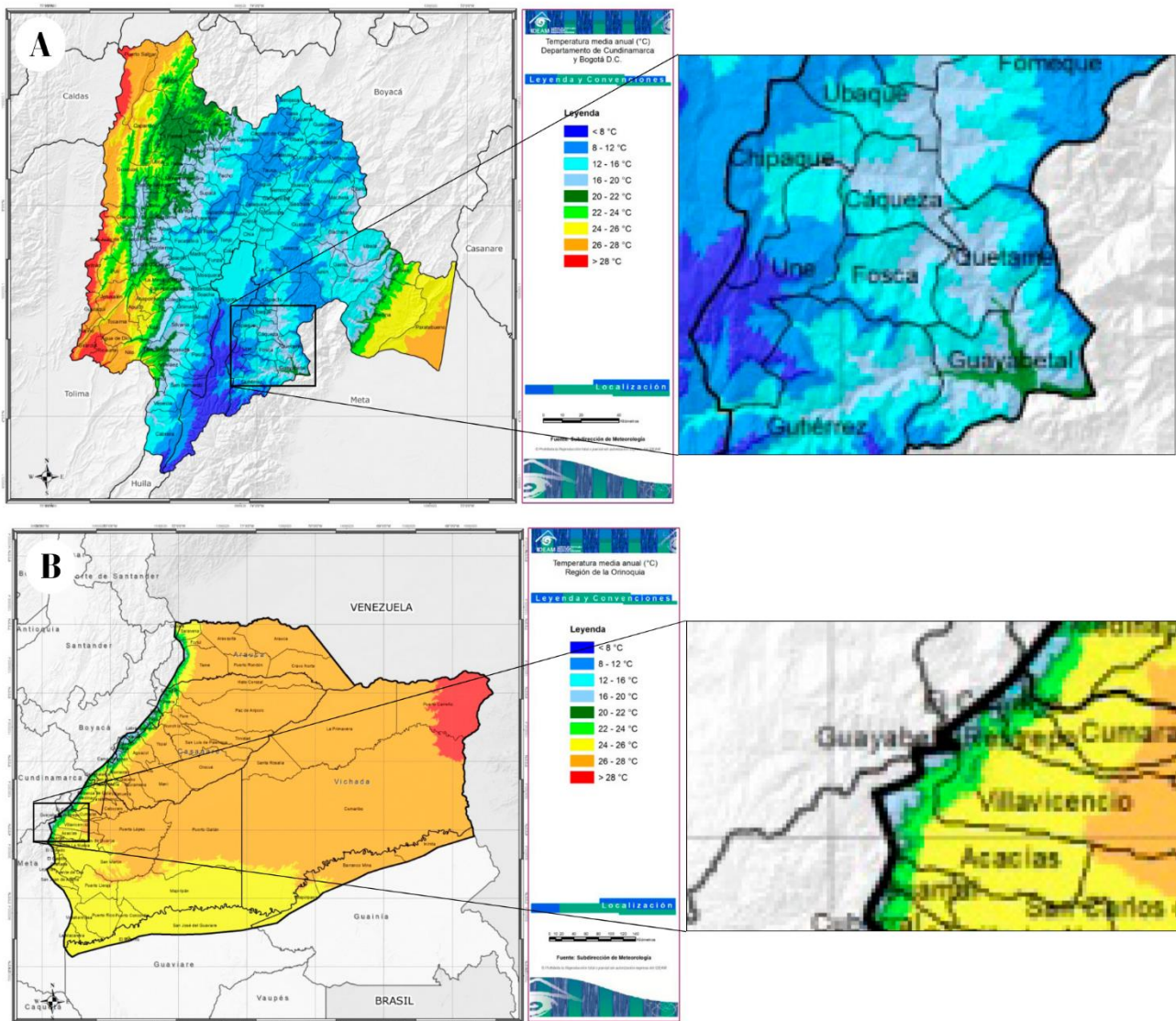


Fig. 30. (A) Annual average temperature in °C of the Cundinamarca department. (B) Annual average temperature in °C of Meta department. Taken from IDEAM (2017).

In Colombia, climate classification is based on humidity and temperature characteristics, according to the Caldas-Lang classification, one of the most widely used due to its simplicity, which divides climates into 25 types (IDEAM, 2017). According to this classification, the area traversed by the "Via al Llano" begins in the Chipaque area with a very cold and humid climate in the western part, transitioning to a semi-humid cold climate in the eastern part (Fig. 31-A). This climate persists in the high parts of the municipality of Cáqueza, while in the valley, a temperate desert climate predominates (Fig. 31-A). Then, in the municipality of Quetame, the valley transitions to a humid and super-humid temperate climate, which extends into Guayabetal, while the high parts of these two municipalities experience a super-humid cold climate (Fig. 31-A). Similarly, the municipality of Villavicencio maintains a humid and super-humid temperate climate (Fig. 31-B).

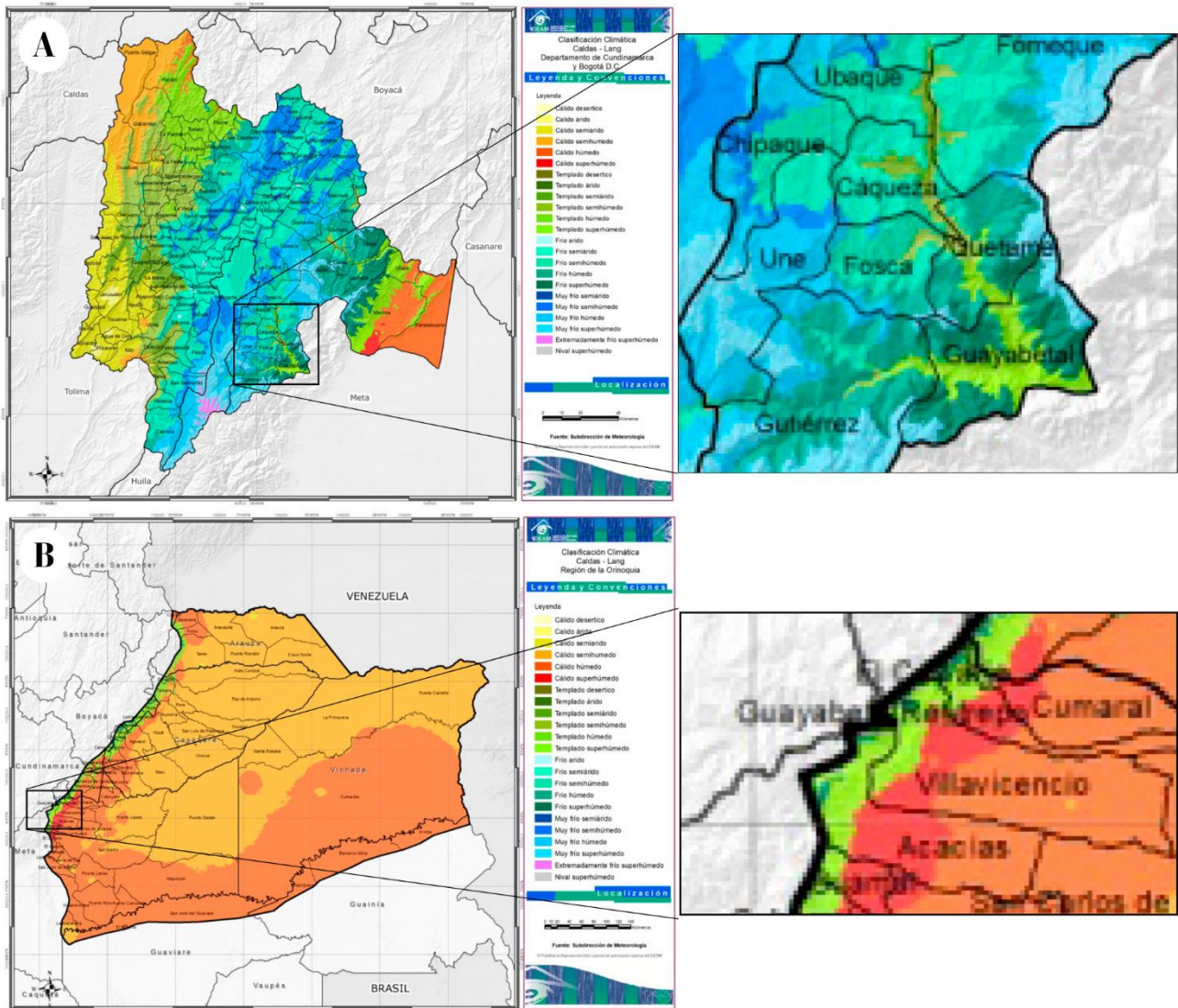


Fig. 31. (A) Caldas-Lang climatic classification of the Cundinamarca department. (B) Caldas-Lang climatic classification of Meta department. Taken from IDEAM (2017).

Precipitation, like temperature, altitude, and climate, exhibits significant variation from Chipaque to Villavicencio. According to the annual precipitation map of the Cundinamarca department, the municipalities of Chipaque and Cáqueza experience a range between 1000 to 1500 mm/year, while Quetame ranges from 1500 to 2500 mm/year (Fig. 32-A). In Guayabetal, the range varies from 2500 to 4000 mm/year, and in the Villavicencio region, the annual precipitation range is from 4000 to 5000 mm (Fig. 32-B). The precipitation regime is predominantly unimodal, with peak precipitation in the middle of the year (highest accumulations in May, June, and July), and minimum precipitation at the beginning of the year (lowest accumulations in December, January, and February). However, the slight increase in precipitation in the months of October and November suggests a bimodal regime (Fig. 33).

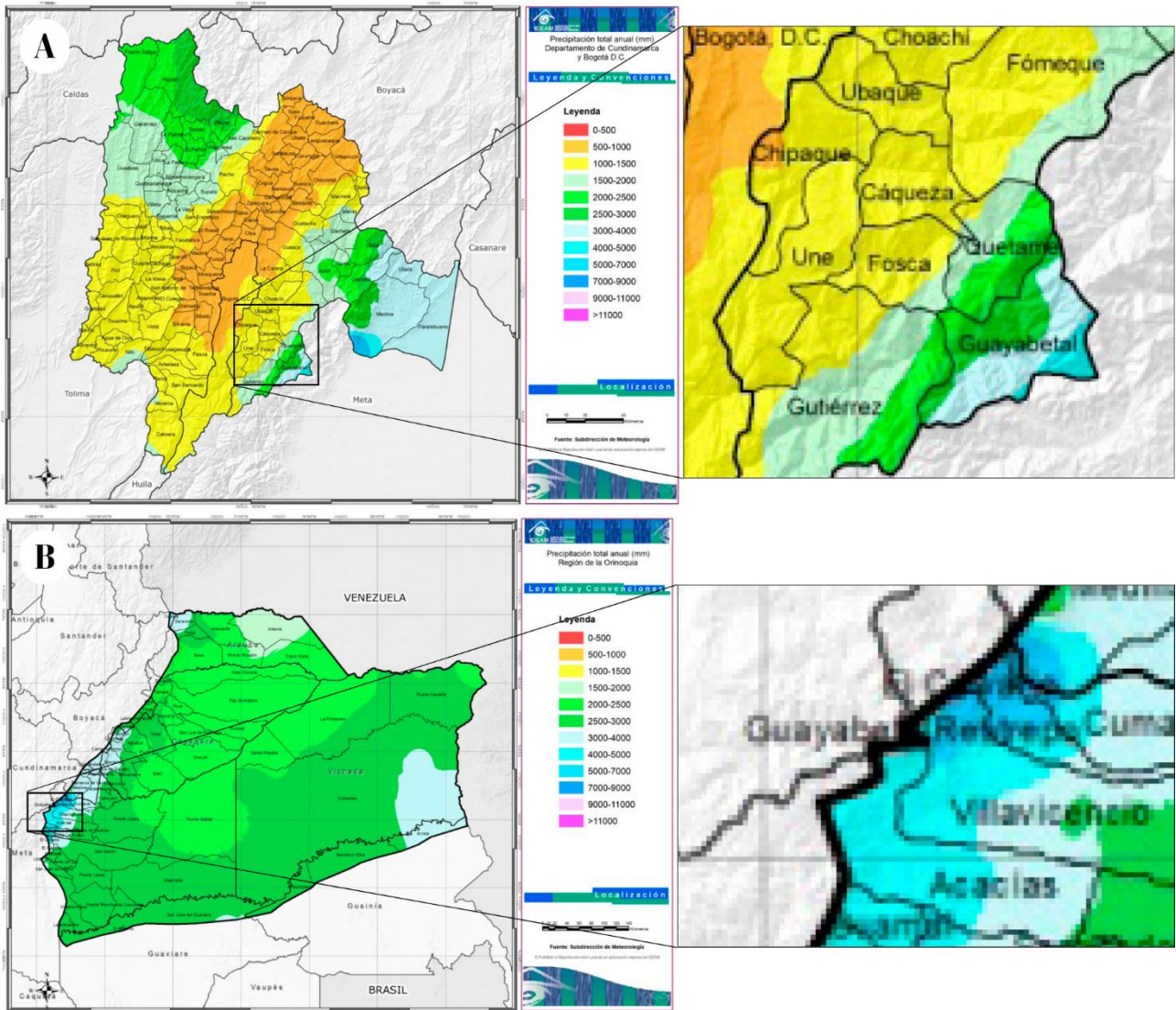


Fig. 32. (A) Total annual precipitation in mm for the Cundinamarca department. (B) Total annual precipitation in mm for Meta department. Taken from IDEAM (2017).

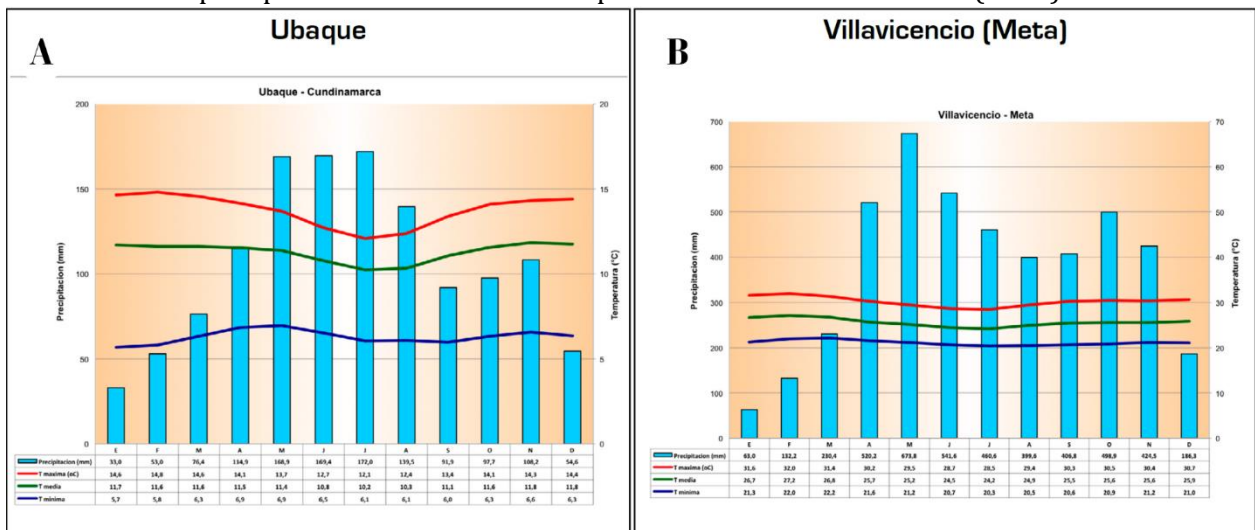


Fig. 33. Bar chart showing monthly precipitation and annual average, maximum, and minimum temperatures (A) Municipality of Ubaque, located north of Chipaque and Cáqueza. (B) Municipality of Villavicencio. Taken from IDEAM (2017).

CHAPTER 3. LANDSLIDES, REMOTE SENSING AND SOFTWARE

Landslides are processes that result in the displacement of materials such as rock, debris, or soil down a slope, under the influence of gravity (Cruden & Varnes, 1996). This phenomenon involves an initial deformation, followed by rupture, and results in displacement (Hungr et al., 2014). These events can occur both on land surfaces and in submerged underwater areas. Additionally, phenomena such as intense or prolonged rainfall, earthquakes, rapid thawing, volcanic activity, and various human actions can trigger landslides (Guzzetti et al., 2012).

3.1. Landslides classification

Mass movements can be classified in multiple ways, according to the relevant characteristics to emphasize or the specific purpose (Varnes, 1978). Some attributes that have been used for their classification include the type of movement, type of material, rate of movement, geometry of the displacement area, and shape of the deposit. Other criteria encompass the age of the movement, its causes, the degree of distortion of the displaced mass, the relationship or lack of relationship between the sliding geometry and geological structure, the degree of development, geographic location, and the state of activity (Varnes, 1978).

The classification proposed by Cruden & Varnes (1996) has gained widespread global adoption. It distinguishes between the type of movement and the type of material. Movements are categorized into five fundamental classes: falls, topples, slides, spreads, and flows; while materials are classified as rock, debris, and soil (Cruden & Varnes, 1996; Varnes, 1978).

Landslides encompass the following types of motion distinguished by their kinematic style. Falls occur when there is a detachment of rock or soil on inclined surfaces, descending mostly through the air. Topple involves the forward rotation of a mass out of an inclined surface, primarily in resistant consolidated materials such as rocks. Slides entail a shearing effort that displaces a mass on surfaces, subdividing into rotational and translational types. Spread result from the liquefaction of soft material beneath a coherent mass. Flows, characterized by continuous movements, occur in unconsolidated materials, sharing similarities with viscous liquids in terms of speed. Lastly, slope deformation are large-scale gravitational movements on steep slopes exhibit scarps, cracks, and bulges without a well-defined rupture surface, with extremely slow movement rates and no documented record (Cruden & Varnes, 1996; Hungr et al., 2014; Varnes, 1978).

Subsequently, Hungr et al. (2014) introduced modifications to the classification, grouping materials into two main classes: rock and soil. These encompass geologically defined rocks, and unconsolidated materials, respectively. Additionally, they define the classification into 32 types of movements. The mechanisms governing the motion, conditioning factors, triggering factors, and other important data for each of these 32 types of landslides are explained in Fig. 34 to 44. These figures maintain the same numbering scheme for the landslides classified by Hungr et al. (2014).


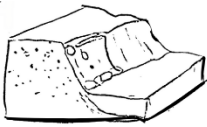
<p style="text-align: center;">ROCK FALL</p> <p style="text-align: center;">1</p> 	<p style="text-align: center;">MECHANISM</p> <p>Begins when there is a detachment of the rock substrate or ice fragment, which falls, bounces, and/or rolls.</p>	<p style="text-align: center;">CONDITIONING FACTORS</p> <p>Steep slope.</p> <p>Discontinuities due stratification or fractures on rocks.</p>	<p style="text-align: center;">TRIGGERING FACTORS</p> <p>Atmospheric degradation weakens the rock, breaking the adhesion between discontinuities.</p> <p>Undercut at the base by agents such as the sea, watercourses, or the wind.</p>	<p style="text-align: center;">KEY DATA</p> <p>If in a talus cone the fragments become to bounced and rolled the motion is call as rock fall.</p>
<p style="text-align: center;">BOULDER/ DEBRIS/SILT FALL</p> <p style="text-align: center;">2</p> 	<p style="text-align: center;">MECHANISM</p> <p>Detachment, fall, rolling and/or bouncing of soil fragments (large clast detached from the soil deposits, or a coherent block of soil).</p>	<p style="text-align: center;">CONDITIONING FACTORS</p> <p>Steep slope.</p>	<p style="text-align: center;">TRIGGERING FACTORS</p> <p>Undercut at the base by agents such as the sea, watercourses, the wind, or artificial cuts or other excavation.</p>	<p style="text-align: center;">KEY DATA</p> <p>They are less common because they degrade rapidly owing to minimal cohesion.</p>

Fig 34. Type of fall movements. (1)Rock fall, and (2) boulder/debris/silt fall. Adapted from Hungr et.al., (2014).

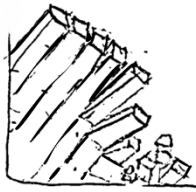
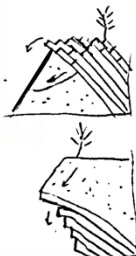
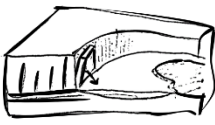
<p style="text-align: center;">ROCK BLOCK TOPPLE</p> <p style="text-align: center;">3</p> 	<p style="text-align: center;">MECHANISM</p> <p>Forward rotation and overturning of rock columns or plates.</p> <p>The center of mass shifts outside the support base, leading to instability.</p>	<p style="text-align: center;">CONDITIONING FACTORS</p> <p>Highly inclined tensional fractures, perpendicular to the slope.</p> <p>Well-defined discontinuities and tension cracks on the surface.</p>	<p style="text-align: center;">TRIGGERING FACTORS</p> <p>Water pressure in tension cracks (degradation).</p> <p>Destabilization at the base.</p> <p>Earthquake acceleration.</p>	<p style="text-align: center;">KEY DATA</p> <p>Stabilizing stresses at the rock bases outweigh frictional forces between adjacent blocks.</p> <p>At the base of large toppling blocks, rock fragments can be observed.</p>
<p style="text-align: center;">ROCK FLEXURAL TOPPLE</p> <p style="text-align: center;">4</p> 	<p style="text-align: center;">MECHANISM</p> <p>Bending and forward rotation of a rock mass.</p> <p>The zone of maximum bending curvature of the strata, known as 'the hinge zone,' can develop joints. These fractures, in turn, lead to the rotation of rock blocks.</p>	<p style="text-align: center;">CONDITIONING FACTORS</p> <p>Relatively weak and fissile rock.</p> <p>Very closely spaced and highly inclined joints or schistose parting, perpendicular to the fall line of the slope.</p>	<p style="text-align: center;">TRIGGERING FACTORS</p> <p>Steep enough inclination to break the tensile strength</p> <p>Absence of any support at the base.</p>	<p style="text-align: center;">KEY DATA</p> <p>The movement is generally slow and tends to self-stabilize.</p> <p>Vegetation-enhanced horizontal lines crossing the upper part of the slope are commonly observed.</p>
<p style="text-align: center;">GRAVEL/SAND /SILT BLOCK TOPPLE</p> <p style="text-align: center;">5</p> 	<p style="text-align: center;">MECHANISM</p> <p>Block toppling of columns of cohesive (cemented) soil.</p> <p>Highly inclined tensional discontinuities and tension cracks on the surface.</p>	<p style="text-align: center;">CONDITIONING FACTORS</p> <p>Instability at the support base promoted by the low strength of weakly cemented or partially saturated soil columns.</p>	<p style="text-align: center;">TRIGGERING FACTORS</p> <p>Undercut at the base by agents such as the sea, watercourses, the wind, or artificial cuts or other excavation.</p>	<p style="text-align: center;">KEY DATA</p> <p>They are less common because they can develop in the fall.</p>

Fig 35. Type of topple movements. (3) Rock block topple, (4) rock flexural topple, and (5) gravel/sand/silt block topple. Adapted from Hungr et.al., (2014).

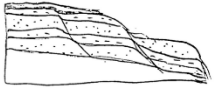
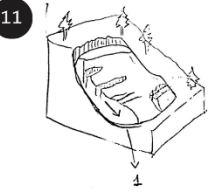
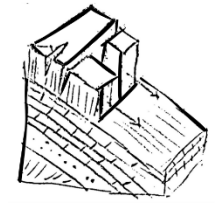
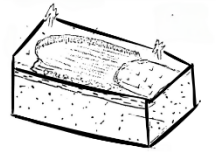
ROCK ROTATIONAL SLIDE	MECHANISM	CONDITIONING FACTORS	TRIGGERING FACTORS	KEY DATA
<p>6</p> 	<p>Sliding of a mass of weak rock on a rotational rupture surface which is not structurally controlled.</p>	<p>Very weak rock masses, often under a stronger cap rock surcharge.</p> <p>Weak rock under shear stress tends to fail ductilely, losing cohesion.</p> <p>The weak rock layer above clay deposits contributes to weakening as the clays deform.</p>	<p>An increase in precipitation can infiltrate undrained failures, initiating the onset of sliding.</p>	<p>Characterized by a prominent main scarp, back-tilted bench at the head and limited internal deformation.</p> <p>Usually slow to moderately slow.</p>
<p>CLAY/SILT (SOIL) ROTATIONAL SLIDE</p> <p>11</p> 	<p>Sliding of a mass of (homogeneous and usually cohesive) soil on a rotational rupture surface.</p>	<p>Undrained failures.</p> <p>Saturated soils of low permeability (clays or silts).</p>	<p>Earthquake acceleration.</p>	<p>Little internal deformation.</p> <p>Prominent main scarp and back-tilted landslide head.</p> <p>Normally slow to rapid, Extremely rapid in sensitive or collapsive soils.</p>
<p>ROCK PLANAR SLIDE</p> <p>7</p> 	<p>Sliding of a mass of rock on a planar rupture surface.</p> <p>A moderate slope can facilitate brittle behavior.</p>	<p>Surface stepped forward.</p> <p>Little or no internal deformation.</p> <p>Layered folded sedimentary rocks, or schistosity on metamorphic rocks, or in intrusive rocks with stress relief joints (exfoliation).</p>	<p>A rise in pore pressure, caused by an increase in water, can weaken frictional strengths.</p>	<p>The slide head may be separating from stable rock along a deep, vertical tension crack.</p> <p>Usually extremely rapid.</p> <p>A 'toe breakout' mechanism on an intact rock mass can develop the planar slide.</p>
<p>CLAY/SILT (SOIL) PLANAR SLIDE</p> <p>12</p> 	<p>Sliding of a block of cohesive soil on an inclined planar rupture surface, formed by a weak layer (often pre-sheared)</p>	<p>Weak layer.</p> <p>Discontinuity inclined at an angle greater than the friction angle.</p>	<p>Earthquake forces can destabilize the frictional strength, leading to block sliding</p>	<p>The head of the slide mass separates from stable soil along a deep tension crack (no active wedge).</p> <p>Slow or rapid movement.</p> <p>Cohesive materials typically prefer curved sliding.</p>

Fig 36. Type of slide movements. (6) Rock rotational slide, (7) rock planar slide, (11) clay/silt (soil) rotational slide, and (12) clay/silt (soil) planar slide. Adapted from Hungr et.al., (2014).

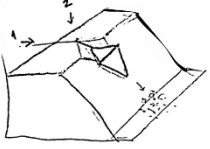
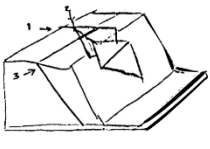
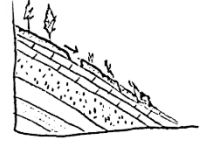
<p>ROCK WEDGE SLIDE</p> <p>8</p> 	<p>MECHANISM</p> <p>Sliding of a mass of rock on a rupture surface formed of two planes with a downslope-oriented intersection.</p>	<p>CONDITIONING FACTORS</p> <p>Well-defined discontinuities on rocks</p>	<p>TRIGGERING FACTORS</p> <p>Increase in pore-pressure by an increase in water</p> <p>Earthquake forces.</p>	<p>KEY DATA</p> <p>No internal deformation. Usually extremely rapid.</p> <p>Greater resistance is exhibited in the discontinuities and pore-pressure than in planar rock slides.</p>
<p>ROCK IRREGULAR SLIDE (COLLAPSE)</p> <p>10</p> 	<p>MECHANISM</p> <p>Sliding of a rock mass on an irregular rupture surface consisting of a number of randomly oriented joints, separated by segments of intact rock ("rock bridges").</p>	<p>CONDITIONING FACTORS</p> <p>Occurs in strong rocks with non systematic structure.</p> <p>The rupture surface forms by connecting many randomly oriented and non-persistent discontinuities.</p>	<p>TRIGGERING FACTORS</p> <p>Increase in pore-pressure by an increase in water.</p> <p>Earthquake forces.</p>	<p>KEY DATA</p> <p>The existence of discontinuities is essential, because strong rock at shallow depths is rarely stressed close to failure.</p> <p>May include elements of toppling.</p> <p>Occurs very sudden and extremely rapid.</p>
<p>GRAVEL/SAND /SILT DEBRIS SLIDE</p> <p>13</p> 	<p>MECHANISM</p> <p>Sliding of a mass of granular material on a shallow, planar surface parallel to the ground.</p> <p>Such planar sliding represents the initial phase of a dry granular flow.</p>	<p>CONDITIONING FACTORS</p> <p>Layer of coarse colluvium, weathered soil, or pyroclastic deposits over a stronger substrate.</p> <p>Layer of soil covering steep slopes.</p>	<p>TRIGGERING FACTORS</p> <p>Extreme rainfall triggers debris slides in areas affected by the loss of natural protection (vegetation).</p>	<p>KEY DATA</p> <p>Many debris slides become flow-like after moving a short distance, and transform into extremely rapid debris avalanches due to the loss of cohesion and partial or full spontaneous liquefaction.</p>

Fig 37. Type of of slide movements. (8) Rock wedge slide, (10) rock irregular slide, and (13) gravel/sand/silt debris slide. Adapted from Hungr et.al., (2014).


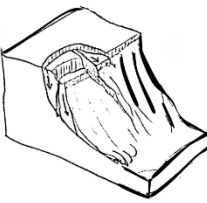
ROCK COMPOUND SLIDE	MECHANISM	CONDITIONING FACTORS	TRIGGERING FACTORS	KEY DATA
<p>9</p> 	<p>Sliding of a mass of rock on a rupture surface consisting of several planes, or a surface of uneven curvature (irregular curvature)</p>	<p>A rupture surface following a horizontal, or gently inclined plane of weakness such as a bedding plane or a weak layer in the stratigraphy, daylighting at the toe.</p> <p>Rupture surface in profile may be bi-linear or curved (listric), but noncircular.</p>	<p>An increase in precipitation can infiltrate undrained failures, initiating the onset of sliding.</p>	<p>The motion is kinematically possible only if accompanied by significant internal distortion of the moving mass.</p> <p>Horst-and-graben features at the head and many secondary shear surfaces are typical.</p> <p>Slow or rapid.</p>
<p>14</p> 	<p>Sliding of a mass of soil on a rupture surface consisting of several planes, or a surface of irregular curvature</p>	<p>Weak horizons.</p> <p>Saturated soils of low permeability (clays or silts).</p>	<p>Earthquake acceleration.</p>	<p>The basal segment of the rupture surface often follows a weak horizon in the soil stratigraphy.</p> <p>Steep main scarp and a horst-and-graben structure form at the head.</p>

Fig 38. Type of slide movements.(9)Rock compound slide, and (14) clay/silt compound slide. Adapted from Hungr et.al., (2014).




<p style="text-align: center;">ROCK SLOPE SPREAD</p> <p style="text-align: right;">15</p> 	<p style="text-align: center;">MECHANISM</p> <p>Near-horizontal stretching (elongation) of a mass coherent blocks of rock as a result of intensive deformation of an underlying weak material.</p>	<p style="text-align: center;">CONDITIONING FACTORS</p> <p>Sedimentary sequences characterized by weak strength often undergo severe plastic deformation.</p> <p>This phenomenon is prevalent in horizontally bedded formations.</p>	<p style="text-align: center;">TRIGGERING FACTORS</p> <p>Water infiltration increases soil plasticity, raising pore pressure and weakening slope stability.</p> <p>Base erosion undermines slope stability.</p>	<p style="text-align: center;">KEY DATA</p> <p>It is identified when a substantial and clearly defined portion of the slope exhibits displacements, allowing the definition of a 'rupture surface' that separates the zone that has moved from the one that has remained stationary.</p>
<p style="text-align: center;">SAND/SILT LIQUEFACTION SPREAD</p> <p style="text-align: right;">16</p> 	<p style="text-align: center;">MECHANISM</p> <p>Extremely rapid lateral spreading occurs when a layer of saturated (loose) granular soil, prone to liquefaction, causes the upper blocks to become fractured.</p>	<p style="text-align: center;">CONDITIONING FACTORS</p> <p>Plastic, soft, and unstable clay tends to liquefy beneath a layer of rock.</p>	<p style="text-align: center;">TRIGGERING FACTORS</p> <p>Spontaneous liquefaction due to pore pressure resulting from a sudden rise in water levels due to rainfall.</p> <p>Liquefaction can occur as a result of motion, such as during an earthquake.</p>	<p style="text-align: center;">KEY DATA</p> <p>The classic example occurred in 1964 after the Alaska Earthquake in Turnagain Heights, Anchorage, Alaska.</p>
<p style="text-align: center;">SENSITIVE CLAY SPREAD</p> <p style="text-align: right;">17</p> 	<p style="text-align: center;">MECHANISM</p> <p>Extremely rapid lateral spreading of a series of coherent clay blocks, floating on a layer of remoulded sensitive clay.</p>	<p style="text-align: center;">CONDITIONING FACTORS</p> <p>Sensitive marine clay, under the ground or deposits.</p>	<p style="text-align: center;">TRIGGERING FACTORS</p> <p>The liquefaction of clays can occur due to an increase in weight or loss of confinement caused by anthropogenic activities such as excavation, or natural causes, such as erosion along the banks of a river.</p>	<p style="text-align: center;">KEY DATA</p> <p>The lateral displacement due to sensitive clays will be active only until the entire package of sensitive clays is evacuated.</p>

Fig 39. Type of spread movements.(15)Rock slope spread, (16) sand/silt liquefaction spread, and (17) sensitive clay spread. Adapted from Hungr et.al., (2014).


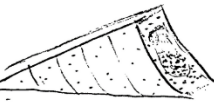
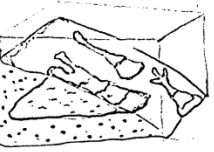
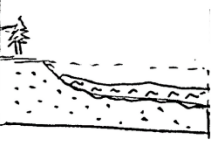
<p style="text-align: center;">ROCK/ICE AVALANCHE</p> <p style="text-align: left;">18</p> 	<p style="text-align: center;">MECHANISM</p> <p>Massive flow of rapidly fragments of rock that travel down mountain slopes as extremely rapid flows, surpassing the frictional flow of dry and angular fragments. Mobility systematically increases with the volume of the event.</p>	<p style="text-align: center;">CONDITIONING FACTORS</p> <p>Potential rock fall or rock slide in an area with steep slopes and rock discontinuities</p>	<p style="text-align: center;">TRIGGERING FACTORS</p> <p>The avalanche typically begins with a triggering event, such as a large rock slide or fall from a cliff or steep slope.</p>	<p style="text-align: center;">KEY DATA</p> <p>Extremely rapid.</p> <p>The avalanche remains dry in motion due to extensive rock fragmentation, creating large pore spaces that cannot fill with water in the brief duration of the event.</p>
<p style="text-align: center;">DRY FLOWS (NON-LIQUEFIED)</p> <p style="text-align: left;">19</p> 	<p style="text-align: center;">MECHANISM</p> <p>Flow-like movement of loose, dry, sorted or unsorted granular material without excess pore-pressure.</p> <p>The motion of dry granular material transitions into shear distortion, resembling a flow.</p>	<p style="text-align: center;">CONDITIONING FACTORS</p> <p>Loose granular material on talus deposits or lee slopes of sand dunes.</p> <p>Inclined slope angle with a few degrees below the upper angle of repose.</p>	<p style="text-align: center;">TRIGGERING FACTORS</p> <p>The triggering factor is the exceeding of the angle of repose of the loose material.</p>	<p style="text-align: center;">KEY DATA</p> <p>Slow or rapid motion.</p> <p>In the absence of pore-pressure change, the movement tend to be slow</p>
<p style="text-align: center;">SAND/SILT/DEBRIS FLOWSLIDE</p> <p style="text-align: left;">20</p> 	<p style="text-align: center;">MECHANISM</p> <p>Flow of sorted or unsorted saturated granular material on moderate slope.</p> <p>Loose, saturated granular soils can fully or partially liquefy during or after failure and create extremely rapid flowslides.</p>	<p style="text-align: center;">CONDITIONING FACTORS</p> <p>Liquefiable materials: loose sands or gravels under water (or under the water table), loose glacio-fluvial silts or loess with basal saturation, loose man-made fills, mining waste, or mine tailings or air fall pyroclastic soils.</p>	<p style="text-align: center;">TRIGGERING FACTORS</p> <p>Cohesion loss and spontaneous liquefaction, caused by over-stressing of loose-saturated soil.</p> <p>Liquefaction induced by an earthquake.</p>	<p style="text-align: center;">KEY DATA</p> <p>Very rapid to extremely rapid.</p> <p>May occur subaerially, or under water.</p>
<p style="text-align: center;">SENSITIVE CLAY FLOWSLIDE</p> <p style="text-align: left;">21</p> 	<p style="text-align: center;">MECHANISM</p> <p>Flow of liquefied sensitive clay, due to a sudden "phase change" of the material from solid to liquid.</p>	<p style="text-align: center;">CONDITIONING FACTORS</p> <p>Very sensitive clays or "quick" clays, often leached marine clays in terraces created by isostatic uplift.</p>	<p style="text-align: center;">TRIGGERING FACTORS</p> <p>Sudden remolding during failure at natural moisture content, a behavior similar in its effect to liquefaction</p>	<p style="text-align: center;">KEY DATA</p> <p>Very rapid to extremely rapid.</p>

Fig 40. Type of flow movements. (18) Rock/Ice avalanche, (19) sand/silt/debris dry flow, (20) sand/silt/debris flowslide, and (21) sensitive clay flowslide. Adapted from Hungry et al., (2014).

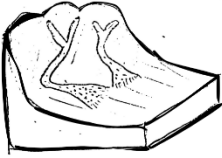

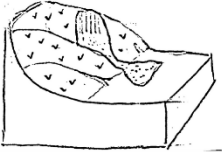
<p style="text-align: center;">DEBRIS FLOW</p> <p style="text-align: left;">22</p> 	<p style="text-align: center;">MECHANISM</p> <p>Surging flow of saturated debris in a steep channel.</p> <p>The surges travel down the channel on slopes steeper than 10–20° and entrain saturated soil, as well as surface water present in the channel.</p>	<p style="text-align: center;">CONDITIONING FACTORS</p> <p>It occurs periodically on established paths, usually gullies and first- or second order drainage channels.</p>	<p style="text-align: center;">TRIGGERING FACTORS</p> <p>The flow may be initiated by a slide, debris avalanche or rock fall from a steep bank, or by spontaneous instability of the steep stream bed.</p>	<p style="text-align: center;">KEY DATA</p> <p>Very rapid to extremely rapid.</p> <p>Intense entrainment of material and water in the flow path, causing liquefaction or a notable rise in pore pressure, even affecting coarse materials.</p>
<p style="text-align: center;">DEBRIS FLOOD</p> <p style="text-align: left;">24</p> 	<p style="text-align: center;">MECHANISM</p> <p>Flow of water, heavily charged with debris, in a steep channel.</p> <p>Peak discharge similar to a flash flood, with deposits extending further downslope than debris flows, often on smaller slope angles (less than 5°).</p>	<p style="text-align: center;">CONDITIONING FACTORS</p> <p>Established paths, usually gullies and first- or second order drainage channels.</p>	<p style="text-align: center;">TRIGGERING FACTORS</p> <p>Extreme flooding in steep channels due to a high quantity of added water, by rainstorms.</p> <p>Stream bed destabilized, causing massive movement of sediment.</p>	<p style="text-align: center;">KEY DATA</p> <p>Very rapid flow of water.</p> <p>Intense entrainment of material and water in the flow path, causing liquefaction or a notable rise in pore pressure, even affecting coarse materials.</p>
<p style="text-align: center;">DEBRIS AVALANCHES</p> <p style="text-align: left;">25</p> 	<p style="text-align: center;">MECHANISM</p> <p>Shallow flow of partially or fully saturated debris on a steep slope, without confinement in an established channel.</p> <p>Very rapid to extremely rapid.</p>	<p style="text-align: center;">CONDITIONING FACTORS</p> <p>Debris avalanches initiate as debris slides and are associated with failures of residual soil, colluvial, pyroclastic, or organic veneer.</p>	<p style="text-align: center;">TRIGGERING FACTORS</p> <p>A failure of thicker accumulations of granular material on steep slopes, such as deep pockets of residual soil or artificial loose fills, may initiate large debris avalanches.</p>	<p style="text-align: center;">KEY DATA</p> <p>Occurs at all scales. Is a unique event that can be found anywhere on steep slopes.</p> <p>In many cases, debris avalanches enter established channels, de-stabilize channel infills, and become debris flows.</p>

Fig 41. Type of flow movements.(22)Debris flow, (24) debris flood, and (25) debris avalanches. Adapted from Hungr et.al., (2014).




<p style="text-align: center;">MUD FLOW</p> <p style="text-align: left;">23</p> 	<p style="text-align: center;">MECHANISM</p> <p>Surging flow of saturated plastic soil in a steep channel, with significantly higher water content than the source material (Plasticity Index > 5%)</p>	<p style="text-align: center;">CONDITIONING FACTORS</p> <p>Materials with fine grain size, comprising only a small proportion of silt and clay, which exhibit measurable plasticity.</p> <p>It occurs on established paths.</p>	<p style="text-align: center;">TRIGGERING FACTORS</p> <p>The supply of large volumes of water needed for mud flow generation may be from precipitation, from melting of summit ice, or snow, or from glacier outburst flooding.</p>	<p style="text-align: center;">KEY DATA</p> <p>Very rapid to extremely rapid.</p> <p>This type is usually on stratovolcanoes ("lahars"), where they exploit the abundance of fine-grained deposits of pyroclastic material and ash.</p>
<p style="text-align: center;">EARTH FLOW</p> <p style="text-align: left;">26</p> 	<p style="text-align: center;">MECHANISM</p> <p>Intermittent flow-like movement of plastic, clayey soil, facilitated by a combination of sliding along multiple discrete shear surfaces, and internal shear strains.</p> <p>Rapid or slower</p>	<p style="text-align: center;">CONDITIONING FACTORS</p> <p>Plastic, disturbed, and mixed soils, whose consistency lies close to the Plastic Limit.</p> <p>Slopes typically inclined at less than about 12°</p>	<p style="text-align: center;">TRIGGERING FACTORS</p> <p>Surging takes place as the source slide becomes destabilized, (rise in pore pressure).</p> <p>Overriding or compressing soil masses downslope, thereby increasing pore pressure through undrained loading.</p>	<p style="text-align: center;">KEY DATA</p> <p>Materials do not experience excessive moisture absorption (Liquidity Index < 0.5).</p> <p>The earthflow body slowly deforms, resulting in lobate morphology</p>
<p style="text-align: center;">PEAT FLOW</p> <p style="text-align: left;">27</p> 	<p style="text-align: center;">MECHANISM</p> <p>Rapid flow of liquefied peat, caused by an undrained failure.</p>	<p style="text-align: center;">CONDITIONING FACTORS</p> <p>The presence of organic fibres and mineral grains.</p> <p>Undrained loading.</p> <p>Slope angles which often exceed 30°</p>	<p style="text-align: center;">TRIGGERING FACTORS</p> <p>Rapid placement of artificial fill on organic substrates by human activity.</p> <p>Natural processes leading to the failure of over-saturated peat accumulations.</p>	<p style="text-align: center;">KEY DATA</p> <p>The extreme compressibility and high water content, however, make the material susceptible to dramatic weakening.</p>

Fig 42. Type of flow movements.(23)Mud flow, (26) earth flood, and (27) peat avalanches. Adapted from Hungr et.al., (2014).

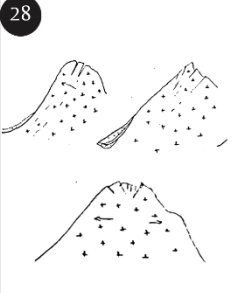
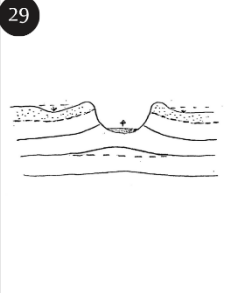
<p>MOUNTAIN SLOPE DEFORMATION</p> <p>28</p> 	<p>MECHANISM</p> <p>Large-scale gravitational deformation of steep, high mountain slopes, manifested by scarps, benches, cracks, trenches and bulges, but lacking a fully defined rupture surface.</p>	<p>CONDITIONING FACTORS</p> <p>Highly stressed rock masses forming mountain slopes, with vertical relief of the order of 1 km or more.</p> <p>Mountain topographic surface features such as scarps, benches, cracks, trenches, and bulges.</p>	<p>TRIGGERING FACTORS</p> <p>Changes in groundwater levels, accelerated during spring periods.</p> <p>Earthquakes which allow discrete movements.</p> <p>Mining operation that induce subsidence.</p>	<p>KEY DATA</p> <p>Movement rates are extremely slow or unmeasurable. There is no record documenting the full development.</p> <p>Gravitational slope deformation features are often misidentified as tectonic fault displacements.</p>
<p>ROCK SLOPE DEFORMATION</p> <p>29</p> 	<p>MECHANISM</p> <p>Deformation of valley or hill slopes, characterized by the sagging of slope crests and the development of cracks or faults, without a well-defined rupture surface.</p>	<p>CONDITIONING FACTORS</p> <p>Slopes made of weak claystones and marls, especially if capped by a massive layer of stronger rock.</p>	<p>TRIGGERING FACTORS</p> <p>Glacial thawing.</p> <p>Flow of ice-rich clayey rocks during periglacial conditions.</p>	<p>KEY DATA</p> <p>Extremely slow movement rates.</p> <p>Deformations include: sagging of slope crests, separation and toppling, flexural pre-shearing of bedding planes and uplift of valley floors.</p>

Fig 43. Type of slope deformation.(28)Mountain slope deformation, and (29) rock slope deformation. Adapted from Hungr et.al., (2014).




<p style="text-align: center;">SOIL SLOPE DEFORMATION</p> <p>30</p> 	<p style="text-align: center;">MECHANISM</p> <p>Deep-seated, slow to extremely slow deformation of valley or hill slopes formed of (usually cohesive) soils.</p>	<p style="text-align: center;">CONDITIONING FACTORS</p> <p>Slopes of valleys or hills composed of cohesive soils.</p> <p>Slopes affected by permafrost, characterized by a high content of ice.</p>	<p style="text-align: center;">TRIGGERING FACTORS</p> <p>Actively eroding slopes.</p> <p>Soils adjacent to steep slopes.</p>	<p style="text-align: center;">KEY DATA</p> <p>An example is the waste piles constructed on steep terrain foundations, which can deform by several tens of meters due to a combination of volumetric consolidation.</p>
<p style="text-align: center;">SOIL CREEP</p> <p>31</p> 	<p style="text-align: center;">MECHANISM</p> <p>Extremely slow movement of surficial soil layers on a slope (typically less than 1 m deep).</p> <p>Result of climate-driven cyclical volume changes (wetting and drying, frost heave).</p>	<p style="text-align: center;">CONDITIONING FACTORS</p> <p>Soil or weak rock layers with a thickness of approximately less than one meter, located near the surface.</p>	<p style="text-align: center;">TRIGGERING FACTORS</p> <p>Swelling and shrinkage with moisture changes, freezing and thawing, and plant and animal activity.</p>	<p style="text-align: center;">KEY DATA</p> <p>The rates of movement are extremely slow (0.5 to 10 mm/year).</p>
<p style="text-align: center;">SOLIFLUCTION</p> <p>32</p> 	<p style="text-align: center;">MECHANISM</p> <p>Very slow but intensive shallow soil creep involving the active layer in Alpine or polar permafrost.</p> <p>Deformation of permafrost under constant stress.</p>	<p style="text-align: center;">CONDITIONING FACTORS</p> <p>Alpine or polar permafrost under soil.</p>	<p style="text-align: center;">TRIGGERING FACTORS</p> <p>Thawing season: the active layer overlying the impervious permafrost table becomes charged with water and contributes to normal movements due to volume changes.</p>	<p style="text-align: center;">KEY DATA</p> <p>Forms characteristic solifluction lobes</p>

Fig 44. Type of slope deformation.(30)Soil slope deformation, (31) soil creep, and (32) solifluction. Adapted from Hungr et.al., (2014).

3.2. Landslides susceptibility maps

Landslides play a crucial role in shaping the landscape and they are particularly prevalent in mountainous regions worldwide. This inherent characteristic makes them one of the most significant natural hazards, resulting in numerous fatalities, infrastructure damage, and substantial economic consequences (Lima et al., 2021; Petley, 2012). In contrast to random events, landslides are governed by the interplay of physical processes and mechanical laws dictating slope stability or failure (Guzzetti et al., 2012). Therefore, accurately predicting their spatial distribution is essential to mitigate adverse impacts. To achieve this, the development of models capable of identifying areas prone to landslides is crucial for effective spatial planning and policy formulation, particularly in mountainous terrain (Lima et al., 2021). The primary aim of landslide susceptibility models is to forecast the likely locations of landslides or specific types by analyzing local terrain characteristics (Guzzetti, 2005).

Various approaches have been utilized to evaluate landslide susceptibility in spatial terms. These methodologies generally fall into two categories: qualitative and quantitative methods (Corominas et al. 2014, Lima et al., 2021, Shano et al. 2020). Qualitative methods, also known as knowledge-driven or heuristic methods, rely on expert judgment, where experts assign values or weights to predisposing factors based on their understanding of geomorphological processes. Such heuristic methods are subjective, as they are based on expert opinions regarding terrain characteristics that may contribute to instability (Lima et al., 2021; Shano et al., 2020).

Within quantitative methods, physically-based models often involve spatial infinite slope models that are frequently coupled with geo-hydrological modules, typically described by complex algorithms (Lima et al., 2021, Soeters and van Westen 1996). In contrast, statistically based and machine learning predictive models, known as Data-driven Landslide Susceptibility Models (DdLSM), utilize empirical relationships between observations and underlying ground features (e.g., lithological or land cover layers) rather than the intricate physical relationships required in physically-based models (Brenning, 2005, Lima et al., 2021, Magliulo 2008, Regmi 2014, Vorpahl et al., 2012). In recent years, data-driven landslide susceptibility models, have gained popularity for estimating the relative spatial probability of landslide occurrence (Conoscenti et al., 2015, Lima et al., 2021, Martinello et al., 2022, Mercurio et al., 2021, Rotigliano et al., 2019).

The standard process of Data-driven Landslide Susceptibility Models (DdLSM) typically involves the following steps: (i) compilation of landslide inventory data, which includes identifying both landslide and non-landslide sampling points, followed by partitioning the dataset into test and training sets. (ii) identification and collection of relevant geoenvironmental factors influencing slope stability. (iii) selection and implementation of a suitable classification method (statistical-based or machine learning). (iv) evaluation of the models' performance quality, (v) production of a map indicating areas susceptible to landslides (Conoscenti et al., 2015, Lima et al., 2021, Mercurio et al., 2022).

3.3. Landslides inventory

A 'landslide inventory' typically comprises location data, movement type, and potentially the occurrence date (Lima et al., 2021). This inventory may be compiled using multi-temporal (historical), event-based, or seasonal approaches (Guzzetti et al., 2012; Lima et al., 2021).

A historical inventory reflects the cumulative impact of numerous landslide events over decades, centuries, or millennia, drawing from literature or archival sources (Guzzetti et al., 2012). Age differentiation in historical inventories is often limited to broad categories such as recent, old, or very old, and they encompass landslides triggered by multiple events spanning years to decades (Guzzetti et al., 2012).

An event inventory, as described by Lima et al. (2021), are landslides triggered by singular events like earthquakes, rainfall, or snowmelt, with the landslide date aligning with the triggering event date.

A seasonal inventory, outlined by Fiorucci et al. (2011) and Guzzetti et al. (2012), captures landslides triggered during one or more seasons. In these inventories, landslide dates are attributed based on the triggering event date and the timing of imagery or field surveys used for compilation. Seasonal landslide maps are crucial in areas prone to recurring landslides, facilitating erosion studies, and temporal landslide analysis, integral components of probabilistic landslide hazard and risk assessments.

Lima et al. (2021) found that event-based inventories are more commonly used than multi-temporal inventories. This is because traditional mapping techniques for producing seasonal and multi-temporal landslide maps are both time-consuming and resource-intensive (Guzzetti et al., 2012). Additionally, the production of seasonal and multi-temporal inventories requires the ability to recognize landslides (or portions of landslides) that leave faint, subtle topographical or land cover changes (Guzzetti et al., 2012).

3.4. Mapping units

A mapping unit, also known as a modelling unit, refers to a delineated portion of terrain with clear boundaries, capturing internal homogeneity within its confines while exhibiting external heterogeneity in comparison to adjacent units (Alvioli et al., 2016). These units encapsulate varied geo-environmental conditions from neighboring areas (Carrara et al., 1999) and may represent categorical, binary, or continuous variables (Lima et al., 2021). They play a crucial role in both predicting model performance and generating output results, exerting significant influence on the design of landslide susceptibility maps (Martinello et al., 2021).

Modeling units typically fall into two categories: (i) pixel or grid cell-based units, and (ii) polygon-based units, such as slope units, unique condition units, and terrain units (Alvioli et al., 2016; Guzzetti, 2005; Lima et al., 2021). The literature on pixel-based units discusses various landslide sampling strategies, including: (a) sampling multiple points throughout the entire landslide body, (b) selecting multiple points within the landslide scarp, (c) placing a single point at the scarp centroid, (d) positioning a single point at the landslide centroid, and (e) distributing

multiple points in the vicinity of the landslide to mimic the original landslide conditions, also known as seed cells (Lima et al., 2021).

In Lima et al. (2021) survey, 88% of the studies utilize pixel-based units as the standard modeling approach, while 10% utilize polygon-based units. The remaining percentage accounts for studies where the modeling unit used was unclear. Typically, pixel-based are derived directly from Digital Elevation Models (DEMs), with predictor variables assumed to have the same resolution as the DEM grid cells. Pixel-based partitioning is efficient and generally yields high modeling performance (Martinello et al., 2021). However, pixel-based units may be too localized to effectively represent unstable conditions, especially when predicting larger landslide events, and may present difficulties for interpretation, particularly for land use planners (Lima et al., 2021).

Alternatively, slope-units (SLUs), defined as slope sectors delineated by drainage and water divide lines, are favored because it is assumed that the entire landslide kinematics (initiation, propagation, and accumulation) occur within them (Martinello et al., 2021). Although polygon-based modeling units, given their generally larger size, may prompt discussions regarding the heterogeneity of large internal features. Therefore, some contributors (e.g., Camilo et al., 2017; Jacobs et al., 2020) suggested to utilize multiple summarizing values to represent predictors within the slope units (e.g., mean, median, standard deviation, among others) (Lima et al., 2021). Subsequently, the most effective metrics can be selected based on their mathematical significance in describing the phenomena (Lima et al., 2021).

Ideally, a complete, accurate and unbiased inventory is essential to build a robust relationship between the landslides and the geo-environmental predictors (Steger et al., 2017). Some publications advocate for the use of multiple points per landslide feature, highlighting a positive impact on prediction outcomes (Lima et al., 2021). However, this approach may lead to an overrepresentation of large landslides compared to small ones, as demonstrated by (Steger et al., 2017) through the artificial simulation of systematic scarcity (undersampling bias). On the other hand, in cases with a low number of landslide samples, confidence and reliability in predictions may be reduced, according with Hussin et al., (2016), who demonstrate that the validation of a model is not substantially influenced by undersampling (e.g., reducing the number of samples by half), but Petschko et al., (2014) argue that the lower number of landslide samples can influence the appearance of the map output and, consequently, its interpretation.

Considering the advantages and disadvantages of each strategy, the representation of landslides should take into account: (i) the characteristics of the available inventory (e.g., point-based or polygon-based) and (ii) the resolution (i.e., pixel size) of the landslide predictors; since high-resolution predictors associated with inaccurate inventories could lead to uncertain predictions. When the use of such inaccurate inventories is unavoidable, adopting a slightly larger modeling unit is recommended to limit the spread of uncertainty (Lima et al., 2021).

3.5. Remote sensing techniques

Landslide inventories can be obtained through a variety of techniques, depending on the specific purpose, the size of the study area, and the resources available (Guzzetti et al., 2012; Lima et al., 2021). Among the most employed methods are field mapping, remote sensing techniques, interpretation of aerial photographs, incident reports, bibliographic analysis, and semi-automatic extraction from high-resolution Digital Terrain Models (DTMs) (Lima et al., 2021).

Traditionally, the compilation of landslide inventories relied on visual interpretation of stereoscopic aerial photography, which enabled the recognition of landslides and related surface processes due to its three-dimensional effect, supplemented by field surveys. However, these methods are both time-consuming and resource-intensive, compounded by the irregular availability of aerial photographs (Guzzetti et al., 2012).

3.5.1. Digital Terrain Models (DTMs)

Currently, digital elevation models (DEMs) have replaced aerial photography due to their advantages as accurate 3D representations of an area. This provides interpreters with a unified, comprehensive view of the study area, enabling them to map both small and large landslides as well as other geological features (such as fault lines and traces of bedding planes) without the need to alter viewpoints or switch between pairs of aerial photographs. This enhances efficiency for the interpretation task and accelerates the acquisition of geomorphological information (Guzzetti et al., 2012).

Moreover, DEMs facilitate the derivation of terrain characteristics such as slope, curvature, and topographic roughness. These digital representations of the topographic surface can be derived from various sources, including LiDAR surveys, stereoscopic or pseudo-stereoscopic images captured by satellite sensors (e.g., ASTER, SPOT-5, Cartosat-1/2 satellites), and SAR satellite sensors. Very High-Resolution (VHR) LiDAR terrain models are preferred due to their ease of use and precision in preparing geomorphological landslide inventories and extracting contour maps covering large areas. However, obtaining VHR LiDAR digital models remains a challenge due to the costs associated with data acquisition and processing time. Therefore, exploring the use of elevation data captured by SAR sensors as an alternative should be considered (Guzzetti et al., 2012).

3.5.2. Optical images

Additional information that cannot be obtained from aerial photographs, LiDAR, or DEM data, which can be utilized to recognize landslides, comes from multispectral information acquired by optical satellite sensors. An important advantage of optical images is that they include reflectance or radiance values in specific (narrow to very narrow) portions of the spectral range, typically ranging from the blue to near-infrared wavelengths, especially for Very High-Resolution (VHR) sensors (e.g., from 450 to 510 μm to 780–920 μm for GeoEye). Optical images allow for the measurement of variations in the spectral signature of the land surface, which is useful for landslide detection through: (i) the creation of derivative images and maps (e.g., maps of the Normalized Difference Vegetation Index, NDVI), and (ii) the semi-automatic classification (segmentation) of satellite images into landslide (failed) and stable (not failed) areas, exploiting their different radiometric signatures (Guzzetti et al., 2012).

In semi-automatic detection and mapping of landslides using radiometric information from optical satellite sensors, careful attention to preliminary image processing steps is crucial. Pre-processing of raw satellite images, such as pansharpening, orthorectification, image co-registration, atmospheric and radiometric correction, is often overlooked by landslide investigators. However, these steps require external information, specific software, skills, and experience. Neglecting the pre-processing phase can lead to changes in the original image, impacting the interpretation and resulting landslide map (Guzzetti et al., 2012).

3.5.3. Radar images

While optical satellite images provide high-quality data, they can be affected by the absence of daylight since they rely on passive sensors. Additionally, cloud cover during and after a landslide event entails an additional challenge as it obstructs visibility and impedes the accurate assessment of affected areas. (Mondini et al., 2021). Immediate response to natural hazard events is crucial for assessing damage and saving lives (Handwerger et al., 2022). Moreover, numerous response efforts face challenges due to a lack of recent and detailed information on the condition or location of damaged areas (Handwerger et al., 2022). Therefore, to overcome these problems, a viable alternative is the use of radar sensors, which do not rely on sunlight for illumination and can penetrate through clouds (Aukema et al., 2019).

Synthetic Aperture Radar (SAR) sensors, operating in the microwave spectral range– between 0.23 GHz (130 cm, P-band) and 40 GHz (0.65 cm, Ka-band), are equipped with side-looking antennas that illuminate the ground surface using single-band pulses (Aukema et al., 2019). These platforms are capable of measuring surface deformations and constructing time series of surface movements using Differential Synthetic Aperture Radar Interferometry (DInSAR), with centimeter to millimeter accuracy. The enhanced capabilities of modern SAR sensors methods are expected to improve mapping of event landslides particularly where the slope failures result in land cover changes e.g., from forest to bare soil or rock (Guzzetti et al., 2012).

SAR sensors have the unique ability to illuminate areas during the night and through cloud cover, making them valuable for detecting fresh landslides during or immediately after a triggering event. However, limitations in ground resolution, acquisition geometry, and data processing hinder the detection and mapping of small to medium-sized landslides in rugged terrain. Nevertheless, SAR data can still provide valuable and timely information for post-event relief efforts and erosion studies (Guzzetti et al., 2012).

3.6. Predictors

The prediction of Spatial Data-driven Landslide Susceptibility Models (DdLSM) is based on the empirical relationship between the response variable (in this case, landslide observations) and the landslide predictors. These predictors are also commonly referred to as "conditioning," "environmental," or "predisposing" factors, and they are used to describe typical terrain conditions that influence slope instability for landslide occurrence. The selection of a predictor is not only related to data availability at the appropriate scale but should also adequately describe landslide occurrence (Lima et al., 2021). The inclusion of biased or irrelevant predictors, as well as the omission of appropriate ones, may significantly interfere with the prediction accuracy of the assessment (Lima et al., 2021; Steger et al., 2016).

Landslide predictors can be categorized into several types: (i) thematic variables, (ii) topographical factors, (iii) climatic elements, (iv) hydrological aspects, and (v) proximity variables. According to a survey by (Lima et al., 2021), thematic variables such as lithological layers, land cover, soil type, and the Normalized Difference Vegetation Index (NDVI) were most frequently utilized. Among topographical variables, slope angle, aspect, curvature, elevation, and soil thickness were commonly employed. The Topographic Wetness Index (TWI) emerged as the predominant hydrological factor, followed by the Stream Power Index (SPI) and Drainage Density (DDe). Proximity-related variables like Distance to Drainage (DDr), Distance to Faults (DF), Distance to Roads (DRo), and Distance to Lineaments (LB) were frequently utilized. Additionally, some studies incorporated various measurements of rainfall (R) to analyze their relationship with landslide occurrences (Lima et al., 2021).

In the study conducted by Lima et al., (2021) of research studies on DdLSM, it was found that, on average, seven variables were used as predictors. Some studies used only one or two predictors, while others utilized up to twenty. Thematic and topographical variables were identified as the most employed.

3.7. Modeling techniques

The modeling approach encompasses a variety of predictive techniques, including both mathematically oriented methods (such as statistical approaches) and adaptable strategies (like machine learning methods) known for their proficient pattern recognition. While there are numerous options for selecting classifiers to delineate landslide susceptibility, standardized criteria for choosing a specific one are lacking. The choice of modeling approach depends on factors such as the scale of the study area and the availability and quality of data necessary for the analysis (Lima et al., 2021).

Historically, simpler yet effective classifiers like the weight of evidence have been widely used. However, in recent years, there has been a surge in the popularity of typical machine learning algorithms, such as random forest, neural networks, decision trees, support vector machines, and artificial neural networks, as well as Generalized Additive Models. Common choices for statistical methods include logistic regression, discriminant analysis, splines, generalized linear models (GLM), and generalized additive models (GAM). These classifiers estimate relative probabilities of landslide occurrence, typically ranging from 0 to 1, based on the relationships

between observations and predictors. To obtain an unbiased assessment of the predictive capability of the model, it is essential to test them using a separate set of observations (test sample), distinct from the data used to train the model (training sample) (Brenning, 2005; Chung & Fabbri, 2003).

The selection of a sampling partitioning strategy plays a crucial role in the validation process of DdLSM. Typically, testing and training samples are chosen using three primary strategies: random, temporal, and spatial partitioning (Chung & Fabbri, 2003). Random sampling was identified as the most prevalent method according to the survey of Lima et al. (2021). It involves an exclusive division of the inventory into training and test samples (e.g., 70% for training and 30% for testing) (Chung & Fabbri, 2003). Temporal partitioning entails testing a model with observations occurring under different conditions than those used for training the model, often involving distinct triggering events (Brenning, 2005; Chung & Fabbri, 2003). Spatial partitioning utilizes landslides within specific area(s) as training samples and the remaining landslides as test samples (Chung & Fabbri, 2003). Utilizing multiple partitioning algorithms (e.g., spatial and non-spatial cross-validation) for training/test partitioning is preferable (Lima et al., 2021).

According to the survey of Lima et al. (2021), the Receiver Operating Characteristic (ROC) curve is mostly used as performance evaluator for most DdLSM, alongside other evaluation techniques including the R^2 coefficient, confusion matrix interpretation, and Cohen Kappa coefficient-based methods. ROC curves are constructed by analyzing multiple confusion matrices, which examine the classification of samples into true positives, false positives, true negatives, and false negatives (Beguería, 2006). Sensitivity, measured by the true positives to false negatives ratio, and specificity, measured by the true negatives to false positives ratio, determine the values within the 0-1 range that form the basis of the ROC curve. This range typically indicates the model's ability to predict landslide occurrences (Lima et al., 2021).

For the development of these prediction and evaluation techniques, the use of modern statistical software and related programming languages (especially open-source ones like R and Python) is essential. These tools provide an abundance of online resources, packages, and scripts for landslide susceptibility modeling (Lima et al., 2021).

3.8. Software

3.8.1. R and RStudio

R is a system for statistical computation that provides a programming language, high-level graphics, interfaces to other languages, and tools for identifying and fixing errors (R Core Team, 2024). The R language, developed in the 1980s by Rick Becker, John Chambers, and Allan Wilks at Bell Laboratories, is a dialect of S and has since been widely used in the statistical community (R Core Team, 2024). Furthermore, the R environment is an integrated suite for data manipulation, calculation, and graphical display. It is a fully planned and coherent system that has undergone rapid development and expansion, facilitated by a large collection of packages (Venables et al., 2024).

On the other hand, RStudio is an integrated development environment (IDE) designed to support multiple languages, including both R and Python. It is available as open-source

software and includes a console, a syntax-highlighting editor that supports direct code execution, and a variety of robust tools for plotting. Additionally, it allows users to manage their workspace efficiently by providing features such as viewing history, debugging data, and managing the code console (Posit, 2024).

3.8.2. QGIS

QGIS, or Quantum GIS, is an open-source software platform that provides a map server (WMS), a feature server (WFS), an implementation of OGC API for Features 1.0 (WFS3), and a coverage server (WCS). Developed as a FastCGI/CGI application written in C++, QGIS Server operates in conjunction with web servers such as Apache or Nginx. QGIS platform offers support for Python plugins, enabling rapid and efficient development and deployment of new features (QGIS Community, 2024).

QGIS Server uses QGIS as a back end for GIS logic and map rendering. Additionally, it makes use of the Qt library for graphics and platform-independent C++ programming. Unlike other map server software, QGIS Server uses cartographic rules as a configuration language, both for server configuration and user-defined cartographic rules (QGIS Community, 2024).

3.8.3. SAGA GIS

The System for Automated Geoscientific Analyses (SAGA) is an open-source geographic information system (GIS), predominantly licensed under the GNU General Public License. Programmed in C++ with an object-oriented design, SAGA operates on various operating systems, including Windows and Linux (Conrad et al., 2015).

SAGA was designed to be simple and efficient implementation of spatial algorithms, serving as a framework for developing and deploying geoscientific methods and models. Presently, this modularly organized GIS software offers over 600 methods, encompassing the entire range of contemporary GIS functionality, from file operations and referencing to topological and geometric analyses of raster and vector data, and comprehensive modeling applications across diverse geoscientific domains (Conrad et al., 2015).

3.8.4. Google Earth Engine (GEE)

GEE is a free academic and research computing platform that allows users to run geospatial analysis in Google infrastructure. This platform boasts a catalog of multi-petabyte satellite imagery and provides libraries of JavaScript code for performing planetary-scale analysis. Users can leverage the power of JavaScript within the Earth Engine Code Editor, a web-based Integrated Development Environment (IDE), to develop custom scripts for processing and analyzing geospatial data (Google Earth Engine, n.d.).

GEE enables users to perform advanced spatial analysis, such as detecting changes in land use, monitoring deforestation, and predicting environmental phenomena, utilizing predefined algorithms and models or by developing their own JavaScript scripts. Additionally, GEE provides access to an active community of users and learning resources to facilitate the development and collaboration in geospatial projects (Google Earth Engine, n.d.).

CHAPTER 4. METHODOLOGY

4.1. Geomorphology Mapping

Geomorphology explores landforms on the surface as well as the continuous natural and anthropic processes that shape them. Moreover, the essential tool for representing them is Geomorphological mapping. This method provides accurate and scaled representations of landform shapes and associated deposits using specific symbols (morphography) (ISPRA et al., 2021).

The Geomorphological map provides valuable information about the geometric characteristics of landforms (morphometry), their origin and evolution in relation to past and ongoing genetic agents and processes (morphogenesis), their age (morphochronology), and their state of activity. It enables the distinction between landforms in evolution and those that are no longer active (morphodynamics). Additionally, the map reveals details about the nature of associated surface deposits and the lithotypes belonging to substrate formations (ISPRA et al., 2021).

Observing the limited amount of symbology on the current geomorphological maps of the area, published by the Geological Service in 2018 (Servicio Geologico Colombiano & Universidad Pedagogica y Tecnologica de Colombia, 2018a, 2018b), an effort is made to enhance them using the "Geomorphological Maps Guide of Italy," known as "*Cuaderno 13*." This guide is the official reference for the accurate representation of landforms on geomorphological maps of Italy at a 1:50,000 scale, developed by the Italian Geological Service (ISPRA et al., 2021).

Firstly, the guide emphasizes the importance of indicating the substrate, the lithology, on which the landforms develop. This substrate should be represented by a uniform color established in the guide (Table 7), without reference to geochronology. Additionally, the process of degradation, erosion, deformation, or rupture can be indicated through the color tone. In other words, darker tones indicate less erodible lithotypes, while lighter tones indicate lithotypes more prone to erosion or with degradation processes (ISPRA et al., 2021).

Table 7. The category in which lithotypes are grouped with their respective colors for cartographic representation. Modified from ISPRA et al., (2021).

Lithotypes	Color	Hexadecimal code
Predominantly calcareous rocks, anhydrite, and gypsum	Brown	#71431D
Predominantly dolomitic rocks	Pink	#D2655E
Predominantly siliceous rocks	Green	#00A15E
Marl, marl-pelitic, and pelitic rocks	Gray	#808080
Rocks consisting of alternations. (e.g., arenitic-pelitic and pelitic-arenitic, marly arenitic, etc.).	Sky blue	#0063A0
Predominantly sandstone rocks (Arenites and sands).	Yellow	#FFD100
Rudite rocks (gravel and conglomerates)	Ochre	#F47321
Effusive and volcanoclastic rocks	Orange	#FFA500
Massive intrusive and metamorphic rocks	Bordeaux	#8B2635
Schistose metamorphic rocks.	Purple	#745399

Respect to the landforms and deposits, it is necessary to delineate them with continuous or discontinuous lines (in the case of uncertain or buried boundaries). Likewise, they should use a color corresponding to the morphogenetic process that generated them (Table 8), employing areal, linear, or point symbols. Shapes characterized by their own configuration will be represented on a white background, such as cones, debris cones, landslide bodies, and rock

glaciers. Additionally, to indicate the morpho-evolution of the landform, two categories are distinguished: active or relict. In this regard, active processes should be represented with more intense or darker colors, while relict forms should have lighter or clearer tones (ISPRA et al., 2021).





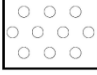
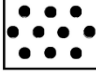

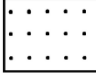
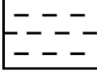
Surface deposits are represented by symbols selected based on the predominant particle size and their degree of cementation. Table 9 provides basic symbology (patterns) to represent various grain size classes. In the case of deposits composed of mixed grain size classes, they should be represented by combining the symbols mentioned above. Similar to landforms, the color of the symbols indicates the predominant morphogenetic process that generated the deposits and their level of activity (ISPRA et al., 2021).

Following the division by municipalities (Chipaque, Caqueza, Quetame, Guayabetal, and Villavicencio) in the study area, geomorphological mapping will be carried out at a scale of 1:100,000 for each of them. Consequently, symbols provided by the 'Cuaderno 13' guide will be used to represent those landforms with lengths greater than 100 meters, indicating point features, as well as linear features for those with lengths greater than 500 meters, and areal features larger than 250,000 m² or 0.25 km². This ensures that these identified features can be easily distinguishable on the map.

Table 8. Landforms grouped based on the morphogenetic process that generated them and their corresponding colors employed in cartographic representation. Modified from ISPRA et al., (2021).

		Morphogenesis	Type of forms	Color	hexadecimal color
NATURAL	Forms related to endogenous dynamics	Tectonic forms		Dark brown	#462810
		Volcanic forms	destruction	Light brown	#9F8047
	costruction				
	Forms related to exogenous dynamics	Litho-structural forms		Ochre	#CC8E35
		Gravitational forms	erosion	Red	#FF0000
			accumulation		
			deformation		
		Fluvial, fluvio-glacial due to runoff forms	erosion	Green	#008000
			accumulation		
		Karstic forms	erosion	Orange	#FFA500
			accumulation		
		Elements of current glacialism and nivation		Turquoise	#40E0D0
		Glacial forms	erosion	Purple	#800080
			accumulation		
		Periglacial and nival forms	erosion	Blue	#0000FF
			accumulation		
			deformation		
	Coastal forms	emerged and submerged erosion	Azure	#007FFF	
		accumulation			
	Eolic forms	erosion	Yellow	#FFFF00	
accumulation					
Forms of other origin		Fuchsia	#FF00FF		
ANTHROPOGENIC	Anthropic forms	erosion	Black	#000000	
		accumulation			

Table 9. Symbolism of the prevalent grain size of deposits. Modified from ISPRA et al., (2021).

Granulometric classes	Loose deposit	Cemented deposit
Boulders (>256mm)		
Cobbles (64-256mm)		
Pebbles (4-64mm) and Gravel (2-4mm)		
Sand (0.0625 - 2mm)		
Silt (0.004 - 0.0625mm) and Clay (<0.004mm)		

4.3. Pluviosity

The precipitation is the process by which water falls to the land surface in the form of rainfall, snowfall, hail, and sleet. This process requires the condensation of water molecules, which are usually attracted to particles of dust in the air (Chow et al.,1971).

To measure precipitation at a specific station (point in space), a variety of instruments or gauges are used. Generally, there are two types: non-recording (storage) gauges and recording gauges. Point-precipitation is typically expressed in depth units (volume divided by collector cross-sectional area) (Hornberger et al., 2014). The typical funnel used for precipitation measurement represents depth units in millimeters (mm), where 1 millimeter of precipitation is equal to one liter of water per square meter of area.

The average annual precipitation on the land surface of the Earth is about 800 mm, but there are some places with great variability, such as Arica in Chile with an annual average of 0.5 mm and Mt. Waialeale in Hawaii, which receives 11,680 mm per year on average (Chow et al.,1971).

In each catchment area, we aim to determine the average precipitation. However, in most cases, there is only one rain gauge within the catchment of interest. Consequently, there is no option but to assume that a single point of measurement represents the mean value over the catchment. Another option is to increase the coverage area to include more station points.

In our pluviometric analysis was included rainfall-data from 19 station points provided by the *Instituto de Hidrología, Meteorología y Estudios Ambientales* (IDEAM) (Fig. 45). However, only three pluviometric stations- Las Casas, Monterredondo, and Susumuco- are located within the study area limits (Fig. 45). To fully understand the rainfall behavior in the study area, we also incorporated pluviometric data from stations surrounding the study area limits, including: Acueducto la Esmeralda, Australia, Bolsa La, Buenavista, Choachi 40, Choachi 80, Cisaca, El Calvario, Fomeque, Gutierrez, Juan Rey, Llano Largo, Monfort, Parrados de San Isidro, Servita, Une (Fig. 45).

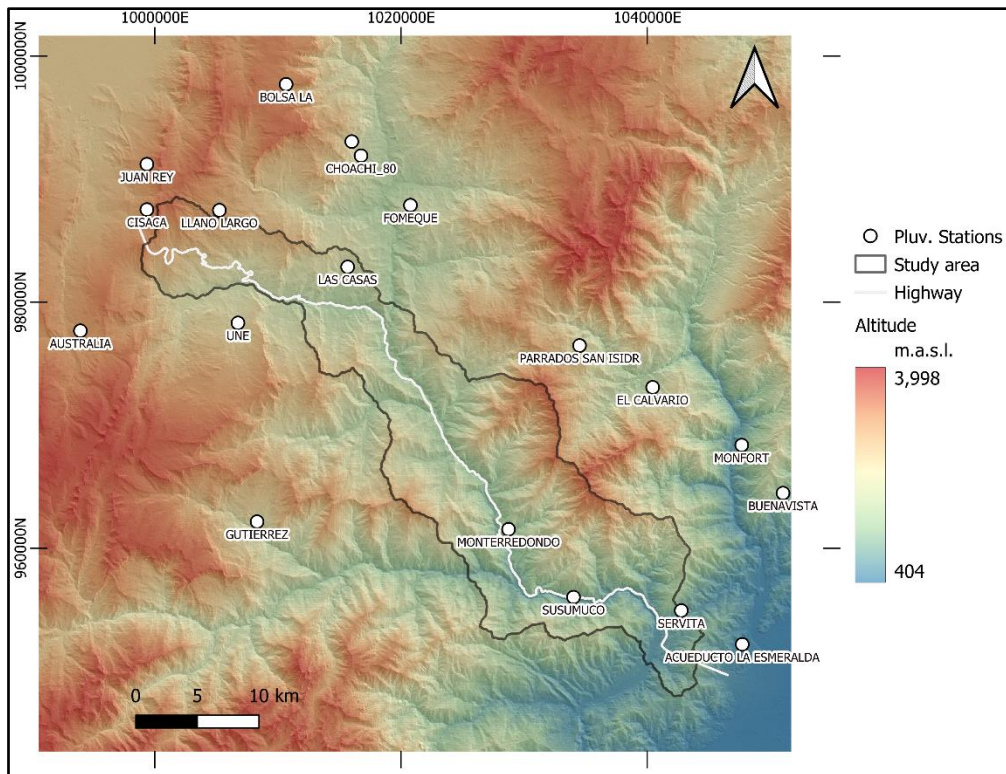


Fig. 45. Pluviometric stations inside and surrounding the study area.

At each station, monthly precipitation data were extracted for the period from 2007 to 2022, providing a dataset spanning 15 years. This statistical technique known as frequency analysis allows us to describe the temporal characteristics of precipitation at a particular station (Hornberger et al., 2014).

During this statistical analysis and data refinement process, the monthly average for each month over a 15-year period is calculated, resulting in 12 values per station known as "**multi-year monthly mean precipitation**". Additionally, the "**mean total annual precipitation**" is determined by averaging the rainfall across all months of the year. It is important to note that if any year lacked data for a particular month, it was not possible to calculate the annual average for that year. Subsequently, the average of the years is calculated from the annual averages, thus yielding a final data point of annual precipitation per station. The summary information of the 19 pluviometric station is in the Table 10.

To estimate the true distribution of precipitation over an area, the isohyetal method is recommended to be applied (Chow et al., 1971). Isohyets are contour lines that represent constant rainfall, identifying areas with equal precipitation levels. This method involves interpolating pluviometric data between adjacent stations (Hornberger et al., 2014). Typically, it is performed through automated interpolation techniques such as Inverse Distance Weighting (IDW) or Kriging.

The isohyets of monthly mean precipitation and mean total annual precipitation in the study area are derived using the Inverse Distance Weighting (IDW) method. This approach estimates values between points with known (measured) values, assigning weights to each measurement based on its distance from the analyzed point. Closer points to the stations are given greater weight (Hartkamp et al., 1994; Hennemuth et al., 2013).

Table 10. Multi-year monthly mean precipitation (Jan. to Dec.) and the mean total annual precipitation (Mean Year) across 19 pluviometric station.

	<i>Name Station</i>	<i>ID Station</i>	<i>Jan</i>	<i>Feb</i>	<i>Mar</i>	<i>Apr</i>	<i>May</i>	<i>Jun</i>	<i>Jul</i>	<i>Aug</i>	<i>Sep</i>	<i>Oct</i>	<i>Nov</i>	<i>Dec</i>	<i>Mean Year</i>
1	Acueducto La Esmeralda	35030040	69.74	88.85	297	548.71	720.47	589.81	503.89	474.42	381.64	496.68	464.59	236.25	4915.18
2	Australia	21201300	30.18	38.22	76.92	134.52	167.48	169.5	174.89	129.86	90.4	100.81	101.42	40.58	1254.76
3	Bolsa La	35025060	38.48	60.27	105.12	164.69	168.11	157.69	153.04	120.7	86.97	138.49	163.72	55.06	1419.46
4	Buenavista	35030090	178.71	163	457.98	866.99	1025.15	961.99	925.47	700.48	623.59	778.55	800.61	480.88	7997.19
5	Choachi	35020240	21.58	38.62	90.5	181.32	167.1	177.12	141.52	118.4	63.32	110.97	124.45	51.88	1213.67
6	Choachi	35020280	16.86	28.56	61.81	121.19	145.06	127.04	117.4	97.64	71.08	78.36	85.97	34.26	997.77
7	Cisaca	21200850	11.95	38.95	48.1	88.72	68.47	117.78	74.9	69.9	31.3	63.48	29.48	38.92	681.95
8	El Calvario	35030010	33.9	53.34	148.2	280.75	373.54	418.33	429.36	376.76	279.98	191.92	142.86	80.46	2809.4
9	Fomeque	35020290	19.76	39.38	81.99	139.06	180.66	158.17	156.41	122.43	82.88	110.14	96.57	41.97	1216.08
10	Gutierrez	35020300	47.6	79.3	118.56	188.04	249.59	275.09	286	206.66	123.54	123.79	129.86	64.22	1890.47
11	Juan Rey	21202040	36.7	63.96	80.54	125.98	122.86	122.15	114.72	93.45	53.52	118.47	136.32	90.17	1083.78
12	Las Casas	35030080	12.23	26.91	65.95	122.77	142.02	131.09	122.44	115.47	73.18	72.95	77.28	31.98	972.67
13	Llano Largo	35025050	27.8	49.51	105.2	157.56	180.68	201.04	195.88	157.35	82.17	114.11	142.94	67.73	1527.74
14	Monfort	35030020	108.29	131.31	293.06	607.27	861.88	766.38	759.75	641.13	635	535	372.36	218.6	5975.36
15	Monterredondo	35020010	42.81	61.19	144.06	251.94	367.88	367.27	426	381.06	252.5	184.25	133.5	87.93	2739.21
16	Parrados San Isidro	35030230	29.28	50.38	119.38	197.38	238.45	337.15	284.15	245.25	178.25	152.07	170.1	85.7	2087.52
17	Servita	35030290	123.15	120.36	407.95	756.19	953.65	834.58	760.34	629.91	556.64	616.96	676.62	370.25	6806.59
18	Susumuco	35020020	86.45	86.92	261.11	489.98	696.5	654.21	693.58	585.42	474.75	342.18	294.47	193.59	4923.31
19	Une	35020420	11.72	33.08	67.7	137.98	133.28	156.3	128.85	105.2	66.95	71.65	74.7	49.08	1036.47

4.4. Landslides inventory

In the study area, there is a variety of landslides triggered by multiple events occurring on dates that are unknown or not recorded. Consequently, the inventory within the study area of “Via al Llano” will be a multi-temporal inventory, reflecting the cumulative landslide events over the years. However, there are some challenges in creating the inventory due the presence of recent, old, or very old mass movements, as well as the challenge of identifying landslides (or portions thereof) that exhibit faint, subtle changes in topography or land cover (Guzzetti et al., 2012).

4.4.1. Google Earth

Through images available on Google Earth, which have very high resolution from MAXAR technologies, the visual inventory within the study area was created. The inventory consists of vector polygons that include the landslide source area, main pathway and depositional zone of each landslide. Mass movements were identified using the criteria as outlined in Rabby & Li, (2019), which include factors such as changes in vegetation (absence in subsequent images compared to prior ones), morphological features (concave and plate areas), elevation, slope characteristics, and the presence of deposits at the base of suspected areas. The absence of vegetation was considered the most important indicator of landslides, contrasting with stable slopes covered by vegetation. This assessment was further supported by the analysis of the 3D model provided by Google Earth, enabling a comprehensive view of slope morphology, elevation, and steepness.

4.4.2. Google Earth Engine

To overcome the time-consuming limitations of identifying each landslide on Google Earth, we created an inventory using optical and radar images available in Google Earth Engine (GEE). This platform allows us to write code that can analyze and process a large quantity of images, in less than 1-2 minutes, a key advantage compared to traditional download process.

To identify areas affected by landslides, we rely on the principle that commonly landslides leave a scar without vegetation with the exposed substrate (Guzzetti et al., 2012). To achieve this, we use optical images in which we apply the Normalized Difference Vegetation Index (NDVI). This index is based on the relationship between the reflectance of vegetation in the near-infrared (NIR) and red bands, allowing us to identify areas with and without vegetation in a range from -1 to 1 (Equation 1; Rouse et al. 1974). Additionally, we leverage radar images in the cross-polarization VH band, which helps us detect the backscattering of rough and vegetated areas, identified by high values, and areas with low backscattering, indicating flat or smooth areas with little or no vegetation (Handwerger et al., 2022).

$$NDVI = \frac{NIR-red}{NIR+red} \quad \text{Equation 1}$$

To compare the results of the inventory created on Google Earth with those created by GEE, we must define a period of a landslide event. However, as this is a multi-temporal inventory, since there is no single event that has created the mass removal phenomena in the area, it has been decided to provide a range as the period when the landslides have formed. "Firstly, the date of the image available in Google Earth indicates a date following the event where landslides were created. Therefore, mass movements occurred in the months leading up to that date.

Consequently, to differentiate the characteristics of the terrain before and after the landslide on GEE, we defined a pre-event and post-event period. The pre-event period begins with the data available since Sentinel 2 images are available (2017) until one year before the image date in Google Earth. The post-event period begins with the data of the Google Earth image until the beginning of the rainy season in the area, which means until May of each year (Table 11).

Table 11. Date and range period of images used to create the landslide inventory.

DATASET	CHIPAQUE	CAQUEZA	QUETAME	GUAYABETAL	VILLAVICENCIO
Date Google Earth Image	Nov.2021	Dec.2022	Jan.2020	Feb.2021	Dec.2020
Pre-Event Range	Jan. 2017- Dec.2020	Jan. 2017- Dec.2021	Jan. 2017- Jan.2019	Jan. 2017- Jan.2020	Jan. 2017- Dec.2019
Post-Event Range	Nov. 2021- Apr.2022	Dec.2022- Apr.2023	Jan.2020- Apr.2020	Feb.2021- Apr.2021	Dec.2020- Apr.2021

On GEE, we selected the optical images from Sentinel 2 that are useful for the inventory, applying filters for the time period (pre-event and post-event) and a cloud cover filter indicating a maximum of ten percent. Additionally, we applied a cloud mask to hide these cloud values. Then, from each selected image, the red band (“B4”) and the NIR band (“B8”) were extracted to calculate the NDVI. Following the procedure outlined by Scheip et al. (2021), the NDVI image of each period stack was generated using the maximum NDVI value per pixel. Subsequently, the relative difference of NDVI (rdNDVI) was calculated using NDVI_{pre} and NDVI_{post} to express the gain or loss of NDVI in a normalized manner as a percentage (Equation 2). This procedure helps mitigate biases arising from seasonal variations. Finally, the negative values of rdNDVI represent vegetation loss, and the more negative the value, the more significant the loss.

$$rdNDVI = \left(\frac{NDVI_{post} - NDVI_{pre}}{\sqrt{NDVI_{pre} + NDVI_{post}}} \right) \times 100 \quad \text{Equation 2}$$

On the other hand, with SAR radar images from Sentinel 1, were applied filters to select cross-polarization band (vertical/horizontal “VH”) and to filter images for the specific time period (pre-event and post-event). The VH band are sensitive to forest biomass structure and roughness surfaces (Le Toan et al., 1992), therefore is useful to identifying landslides in vegetated areas. We followed the procedure outlined by Handwerger et al. (2022) to detect potential landslides, which involved calculating the difference in backscattering between pre- and post-event conditions using the mean of the periods stack. The coefficient of backscattering in dB, which is the intensity, can range from positive and negative values. High intensity backscattering represented by less negative values indicate areas with forest biomass and rough surfaces. Therefore, when landslide occur, the intensity of backscattering decreases to highly negative values because the surface becomes smoother. In line with this, when the difference between the mean of the pre- and post-event images is calculated, positive values correspond to a decrease in SAR backscattering intensity post-event (Handwerger et al., 2022).

Ground surface change due to flooding, agriculture, mining, deforestation, and more, can also be detected in the previous procedures, which could result in false positives (Handwerger et al., 2022). Therefore, to address this challenge Handwerger et al. (2022) and Scheip et al.

(2021), removed some areas that unlikely to correspond to landslides, such as those with low slope, by employing threshold-base masks of slope and curvature derived from topographic data from SRTM DEM available on GEE. In our study area, a slope mask was applied to cover areas with slope values below 10°, along with flat and convex areas.

4.5. Confusion Matrix

In remote sensing classification studies, the confusion or error matrix is widely used to assess classification accuracy. The class labels observed in the map and those in the reference dataset yield a basic 2×2 or binary confusion matrix (Foody, 2020). In each case (e.g., an image pixel), it either exhibits (+) a specific trait or does not (-), for example representing the presence or absence of a certain feature. For instance, in our scenario, it is denoted as landslides and non-landslides. The inventory obtained by GEE will be assessed using the confusion matrix, with the inventory generated on Google Earth serving as the reference.

	Reference (+)	Reference (-)
Predictive (+)	A True Positive (TP)	B False Positive (FP)
Predictive (-)	C False Negative (FN)	D True Negative (TN)

Fig. 46. Confusion matrix for a binary classification.

The binary confusion matrix consists of four elements that summarize every possible scenario of class labeling. "A" or true positives represent the cases classified as landslide presence in both image classification and reference data. "D" or true negatives represent the cases classified as non-landslide or landslide absence in both image classification and reference data. Thus, the cases lying in elements of the main diagonal, A and D, represent those that have been correctly classified. All the cases that have been incorrectly classified lie in the off-diagonal elements of the matrix B and C. "B" or false positives are those cases that have been classified as landslides but are not actually landslides. Such cases represent commission errors, or type I errors. "C" or false negatives have landslide presence according to the reference data but were classified as non-landslides; these cases represent omission errors, or type II errors (Foody, 2020; Stehman, 1997).

From this information, it is possible to obtain certain metrics or measures to evaluate accuracy, which include the following (Gu et al., 2009; Valero-Carreras et al., 2023):

- Sensitivity reflects the ability to classify positive cases (landslides). It is calculated as the proportion of truly positive cases relative to the total number of actual positive cases.

$$Sensitivity = \frac{TP}{TP + FN} \quad \text{Equation 3}$$

- Specificity is the capability to classify negative cases (non-landslides). It is the proportion between truly negative cases and the set of all the negative predictions.

$$Specificity = \frac{TN}{TN + FP} \quad \text{Equation 4}$$

- Precision is a measure used to evaluate landslide classification among the correctly classified as landslides. It is calculated as the proportion between truly positive classification and the set of all the real positive values.

$$Precision = \frac{TP}{TP + FP} \quad \text{Equation 5}$$

- Accuracy (ACC) is the proportion of correctly classification. It measures how well a classify the landslides.

$$Accuracy = \frac{TP+TN}{N} \quad \text{Equation 6}$$

- The kappa coefficient, κ , proposed by Cohen (1960), is a statistic that measures the agreement or disagreement between two classifiers. To do this, the probability of agreements that are not given by chance ($ACC - P_c$) and the probability of disagreement by chance ($1 - P_c$) are calculated (Valero-Carreras et al., 2023):

$$P_c = \frac{(TP+FN) * (TP+FP) + (TN+FN) * (TN+FP)}{N^2} \quad \text{Equation 7}$$

$$\kappa = \frac{ACC + P_c}{1 - P_c} \quad \text{Equation 8}$$

The magnitude of κ lies on a scale from -1 to $+1$ but interest is typically focused on only on positive values because negative values indicate a level of agreement less than that due to chance and can be difficult to interpret (Fig.47) (Foody, 2020; Sim and Wright, 2005). The maximum value of $\kappa = +1$ occurs when there is perfect agreement and a value of $\kappa = 0$ arises when the observed agreement equals that due to chance (Cohen, 1960; Foody, 2020). However, there are different scales for interpreting the kappa coefficient, as summarized by Foody, 2020, based on Czaplewski, 1994 (Fig.47).

	A	B	C
1.0	Almost perfect	Excellent	Excellent → Perfect
0.8			Very good
0.6	Substantial	Fair to Good	Good
0.4	Moderate		Fair
0.2	Fair	Poor	Poor
0.0	Slight		Very poor
	Poor		Very poor

Fig. 47. Scales for interpreting the kappa coefficient (A) Landis & Koch scale (1977). (B) Fleiss et al., scale (2013). (C) Monsrud & Leemans scale (1992). Modified from Foody (2020).

In addition, to evaluate whether there is a tendency of type I or type II error, or if the difference between them is due to chance, the McNemar test can help us identify it. This statistical test allows us to determine if there is a significant difference between the values of the two discordant cells (Fig.46, B and C), based on the null hypothesis that both types of discordance are equally probable (Pembury Smith & Ruxton, 2020).

4.6. Independent variables

Stochastic methods employed in landslide susceptibility mapping involve the selection of a set of independent variables used to predict the landslide occurrence (usually represented as a binary variable). These predictors are carefully chosen from a collection of geo-environmental variables that act as proxies for the factors believed to influence the primary mechanism of slope failure, as evidenced by prior research (e.g., Conoscenti et al., 2015; Costanzo et al., 2014; Rotigliano et al., 2019, and reference therein). Consequently, these statistical methods enable investigators to assess the probability of future mass movement by defining quantitative relationships between the spatial distribution of the independent and dependent variables (Conoscenti et al., 2015).

The geo-environmental variables associated with topographic attributes were derived from a 12.5m cell digital elevation model (DEM), from Also-Palsar taken in 2011. These variables were extracted using the open-source GIS software SAGA (Conrad et al., 2015). In total 11 variables were extracted from the DEM, and a summary of these variables is provided in Table 1.

Additionally, lithological units obtained by (INGEOMINAS, 1998, 2011), the mean total annual precipitation generated by the data precipitation of IDEAM and the NDVI obtained from Sentinel 2 images were included as predictor variables.

4.6.1. The elevation (ELE)

Altitude data above sea level is represented in the Digital Elevation Model (DEM) as the value of each pixel. However, there are some pixels that are inconsistent, as they are surrounded by cells with higher elevation, meaning they are depressed cells known as sink. These depressions in the DEM can be natural features of the terrain or suspicious artifacts, but they can also represent imperfections in the DEM due to errors during its generation. In our work, we have used the 'fill sinks' method by Wang and Liu (2006), which considers the relationship of depressed pixels with the flow pattern in the basin, in order to fill those sinks found in the study area.

4.6.2. The slope (SLO)

It is the maximal rate of change of elevation values, which indicates the angle between the horizontal plane and the one tangential to the surface (Zevenbergen & Thorne, 1987). Defined as:

$$\text{SLOPE} = \arctan(|(p, q)|) \quad \text{Equation 9}$$

$$p = \frac{\partial z}{\partial x} \quad q = \frac{\partial z}{\partial y} \quad \text{Equation 10}$$

4.6.3. The aspect (ASP)

It indicates the flow-line direction. It is a circular land-surface parameter and describes the same slope direction (Zevenbergen & Thorne, 1987). Defined as:

$$\text{ASPECT} = 180 - \arctan\left(\frac{q}{p}\right) + 90 * \frac{p}{|p|} \quad \text{Equation 11}$$

The Northness (N) and Eastness (E) are derived from the cosine and sine of the aspect (ASP) information.

4.6.4. Plan Curvature (PCV)

It is the second partial derivative of elevation. It is a normal section of a smooth surface and is known as the curvature of the contour line, so the flow lines can converge or diverge if the plane curvature is concave or convex, respectively (Dikau, 1988). Defined as:

$$r = \frac{\partial^2 z}{\partial x^2}, s = \frac{\partial^2 z}{\partial x \partial y}, t = \frac{\partial^2 z}{\partial y^2} \quad \text{Equation 12}$$

$$\text{PLANC} = -\frac{q^2 \cdot r - 2p \cdot q \cdot s + p^2 \cdot t}{\sqrt{(1+p^2+q^2)^3}} \quad \text{Equation 13}$$

4.6.5. Profile curvature (PRC)

It is the second partial derivative of elevation. The profile (or vertical) curvature can be used to distinguish (locally) convex and concave shapes. It describes the relative deceleration/acceleration of flow (Shary, 1995). Defined as:

$$\text{PROFC} = -\frac{p^2 \cdot r + 2 \cdot p \cdot q \cdot r \cdot s + q^2 \cdot t}{(p^2 + q^2) \cdot \sqrt{(1+p^2+q^2)^3}} \quad \text{Equation 14}$$

4.6.6. Convergence Index (CI)

It gives much smoother results of plan curvature, so it calculates an index of convergence/divergence to overland flow according to the slope gradient of surrounding cells. The result is given as a percentage. Convergent has negative values and divergent positive values (Köthe et al., 1996; Watkins, 2019).

4.6.7. LS Factor (LSF)

It determined the slope length by the slope gradient and the slope length factor (RUSLE equation) for a specific cell. On last, is taken in account the unit contributing area at the inlet and outlet grid cell. High values are related with the steepest slopes (Desmet & Govers, 1996). Is used to know the transport capacity and erosional forces.

4.6.8. Stream Power Index (SPI)

It describes the potential of flow erosion. Stream power and potential erosion increase by the steepness increase, that means the amount of water contributed by the upslope area and velocity of water flow is high (Gruber & Peckham, 2009). Is defined as:

$$SPI = A \cdot \tan(S) \quad \text{Equation 15}$$

Where A is the catchment area and S the slope.

4.6.9. Topographic Position Index (TPI)

It compares the elevation of each cell in a DEM to the mean elevation of a specified neighborhood around that cell. Positive TPI values represent locations that are higher than the average of their surroundings (ridge), and negative TPI values represent locations that are lower than their surroundings (valleys). TPI values near zero are either flat areas (slope near zero) or areas of constant slope. TPI values are an inherently scale-dependent phenomenon, according to the radio of the surrounding (Weiss, 2001).

$$TPI = \text{int}((dem - focalmean(dem, annulus, irad, orad)) + 0.5) \quad \text{Equation 16}$$

Scalefactor= outer radius in map units

Irad= inner radius of annulus in cells

Orad = outer radius of annulus in cells

Taking in account Slope Position, landscapes can be classified into discrete slope position classes.

4.6.10. Topographic Wetness Index (TWI)

Describe the tendency of a cell to accumulate water. Defined as: $\ln[A/\tan \beta]$, where A is the specific catchment area and β is the local slope angle (Quinn et al., 1995).

4.6.11. Vertical Distance to Channel Network (VDCN)

It is obtained by an interpolation method, that does an iterative aggregation of values of the cells, (the number of steps depends on the size of the grid data set). The interpolation is between the position of the grid cells with channel lines (that had got z-values), and in each interpolation a z-value is assigned. The result is a grid data set that constitutes a theoretical surface regarding to the channel lines ("base level"). The VDCN is the result of the subtraction between the DEM and the base level (Bock & Köthe, 2008).

4.7. Data sampling

To explore the spatial connections between predictor variables and the geographical position of the landslides, we selected a mapping unit consisting of a grid with 12.5meter cells, corresponding to the resolution of the available DEM.

Additionally, our sampling strategy entailed partitioning the landslide area into three distinct datasets: SUP, INF, and BODY (Fig. 48). This division aims to assess the predictive capacity differences for various parts of the landslide (source area, entire area, and deposition zone) within each dataset, as explained below:

- SUP and INF: These datasets contain the highest and the lowest 10% of cells within each landslide area, respectively. SUP aims at representing the conditions of the main source area while INF cells are expected to characterize the accumulation area.
- BODY: This dataset encompasses random cells within the landslide polygons, providing a comprehensive view of the entire landslide area.

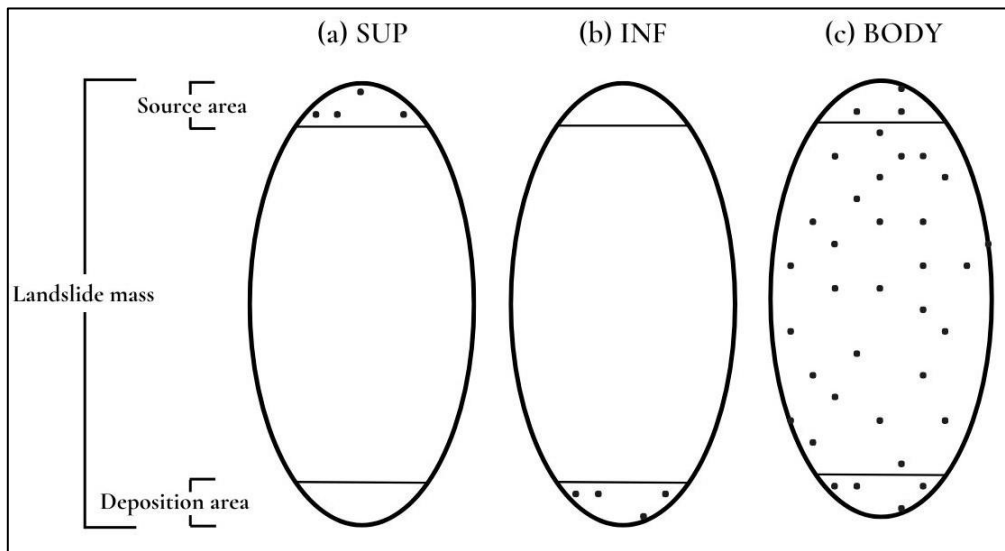


Fig. 48. Representation of data sampling strategy on landslides. (a) Random pixels from the highest 10% landslide area. (b) Random pixels from the lowest 10% landslide area. (c) Random pixels from all landslide areas.

Furthermore, during the sampling process, each mapped landslide was assigned a distinct and unique identification (ID). This distinction is crucial to avoid selecting cells during the testing phase from the same landslides used in the training process. mages.

4.8. Statistical modeling

The probability of landslides in the study area was estimated by generating models using the Multivariate Adaptive Regression Splines (MARS) algorithm. MARS is a non-parametrically methodology for estimating general functions from high-dimensional data (independent variables) (Friedman, 1991). This approach extends traditional linear models by creating multiple basis functions or regression models, through a two-step strategy involving forward and backward procedures.

In the forward step, many basic functions are generated intentionally to capture the nuances in the data, sometimes resulting in overfitting (Friedman, 1991). Subsequently, the most suitable basis function is selected as candidate “variables” in the backward step. To connect these separate regression lines, the algorithm identifies optimal breakpoints, known as knots. This results in a piecewise linear response with breaks at the knots, or regression splines across neighboring subsets, yielding a smooth response curve (Vorpahl et al., 2012).

The primary utility of MARS lies in its ability to derive a predictive relationship between a “response” variable and numerous concurrently measured “predictor” variables. It accomplishes this task using only the values of the predictor variables (training data) to establish a rule for estimating (missing) response values in future observations (Friedman, 1991).

The models were created using the “Earth” package in the open-source statistical programming language “R” (R Core Team, 2021). In our application, we integrated both categorical and continuous variables to construct distinct models. To ensure the credibility of our results, we generated ten calibrations, and ten validation samples for each model.

4.9. Validation strategy

To assess the performance of the model, we conduct 10 random repetitions. This strategy helps prevent overfitting or underfitting with the training dataset (Chung and Fabbri 2003). In this study, for each dataset, 75% of the data was utilized for model training, while the remaining 25% was reserved for testing. During this process, data was randomly sampled to ensure a representative and unbiased selection. Additionally, the predicted binary variable, which in this study signifies the presence or absence of landslides, was kept at a 1:1 ratio.

We evaluated the accuracy of the models obtained for each dataset, by generating receiver operating characteristic (ROC) curves and calculating the corresponding area under the ROC curve (AUC) for training and testing sample. The ROC curve is a graphical representation that relies on Sensitivity (true positive rate, TPR) and the associated value of 1-Specificity (false positive rate, FPR) at various cut-off thresholds (Tien Bui et al., 2016). The AUC is utilized to compare the overall performance of the models. It can be interpreted as the probability that the classifier will correctly rank a randomly selected pixel as either a landslide or non-landslide, where an AUC value of 1 indicates a model with exceptional discrimination between areas of high and low landslide probability (Tien Bui et al., 2016).

In this experiment, we classified the accuracy of the models as either acceptable, excellent, or outstanding based on the AUC values. Models were considered acceptable with AUC values greater than 0.7, excellent with values exceeding 0.8, and outstanding with values surpassing 0.9 (Vargas-Cuervo et al., 2019).

CHAPTER 5. RESULTS

5.1. Geomorphology Map

In the study area, the identification of both natural and anthropogenic landforms was carried out using the methodology of the "Geomorphological Maps Guide of Italy," known as "Cuaderno 13" (ISPRA et al., 2021). In the 'Vía al Llano' area, the main morphogenetic process corresponds to the lito-structural, characterized by cuesta and trench resulting from selective erosion, as well as structural slopes, some of which also exhibit tectonic landforms. The second principal morphogenetic process identified is the fluvial, as mentioned, the study area comprises basins whose waters flow into the Negro and Guayuriba rivers, along which the road runs almost parallelly. Lastly, it is important to highlight the presence of gravitational landforms on all slopes of the mountainous area.

In the area of Chipaque (Fig. 49), we find a significant presence of lito-structural landforms with slopes whose main dip is towards the northeast. Additionally, selective erosion in the form of trenches and knickpoints is observed. In some slopes next to the cuesta dip, a sub-horizontal surface can be identified. Regarding fluvial landforms, the presence of V-shaped valleys and relict alluvial fans stands out, with no other significant fluvial landforms, as the Rio Negro runs along the southern boundary of the area. On the other hand, gravitational processes are evident with slow movements present in the western and northern parts of the area. The highway passes over these areas at the beginning from the west. Furthermore, there is an anthropogenic landform represented by the quarry to the west, at the beginning of the road. Finally, the Chipaque area is strongly dominated by a lithology alternating between mudstones and sandstones (blue in color) from Chipaque Formation., where selective erosion is observed (Fig. 49).

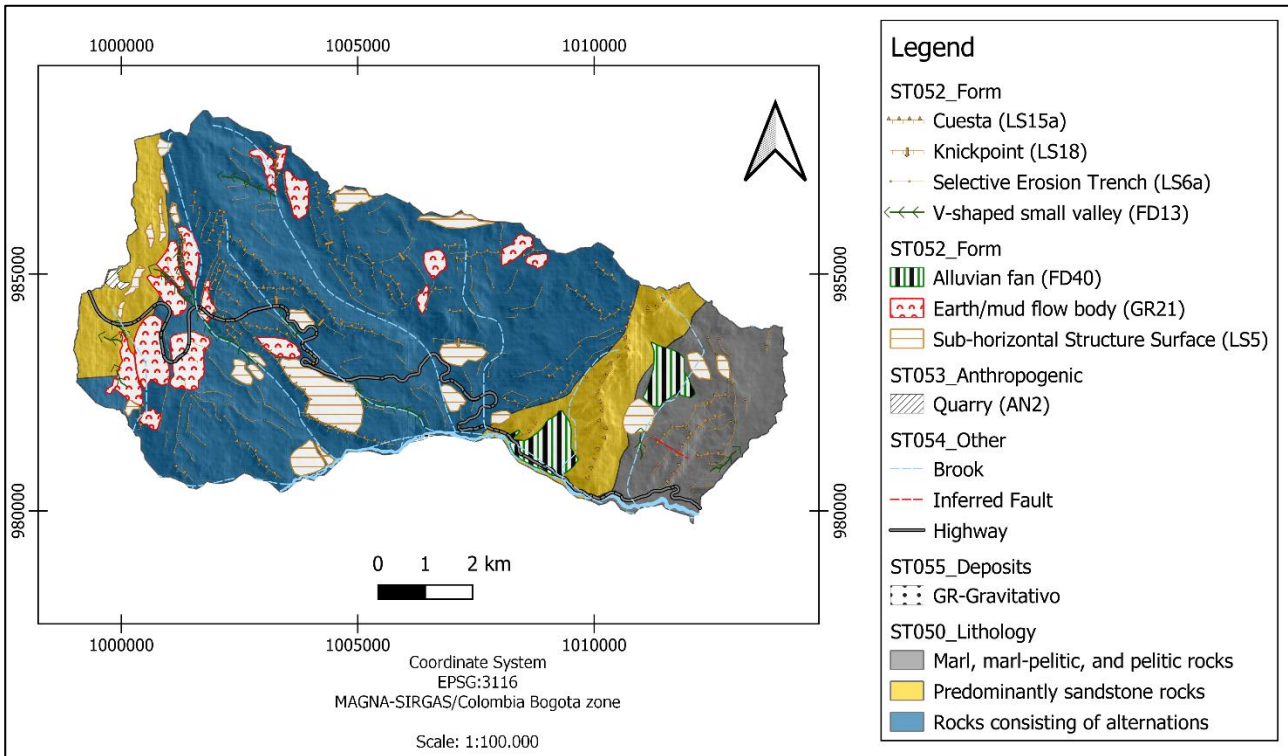


Fig. 49. Geomorphological map of Chipaque.

In general, the region of the municipality of Cáqueza is predominantly controlled by structural landforms (Fig. 50). There is a widespread presence of cuesta, whose dip orientation is not uniform throughout the area, with a southern orientation in the central part and an eastern orientation in the southern part of the area, after crossing the boundaries of some faults. In some areas, it is also possible to observe tectonically controlled sub-horizontal surfaces, as well as stepped slopes and crests of selective erosion. Additionally, in the southern part, there is a hill where the presence of "Hogsback" (those where lines gather) is observed (Fig. 50).

Regarding fluvial landforms, a flat area intersected by some watercourses is observed in the northern part of the area, where alluvial terraces can be distinguished, as well as an alluvial cone. Then it is possible to identify the floodplain area of the Negro River, which begins on the west side and remains significant in the central and final part of the area. However, the road follows the southern edge of this floodplain throughout its route in the Cáqueza area. It is important to highlight that within one of these fluvial landforms, specifically one of the terraces on the southern side, the urban area of Cáqueza is located, an area that has been influenced by mass movements over the years (Fig. 50).

In the area, there is the presence of fault facet landforms associated with faults, which align with the Cáqueza Fault whose strike is east-west. However, these are the only tectonic landforms that were identified. As for gravitational landforms, slow movements were identified on the northern slope facing the triangular facet of the Cáqueza fault, due to the presence of lobes and non-uniform surfaces. Finally, we see once again a prevalence in rocks alternating between shales and sandstones (blue in color), this time belonging to the Lutitas de Macanal Formation (Fig. 50).

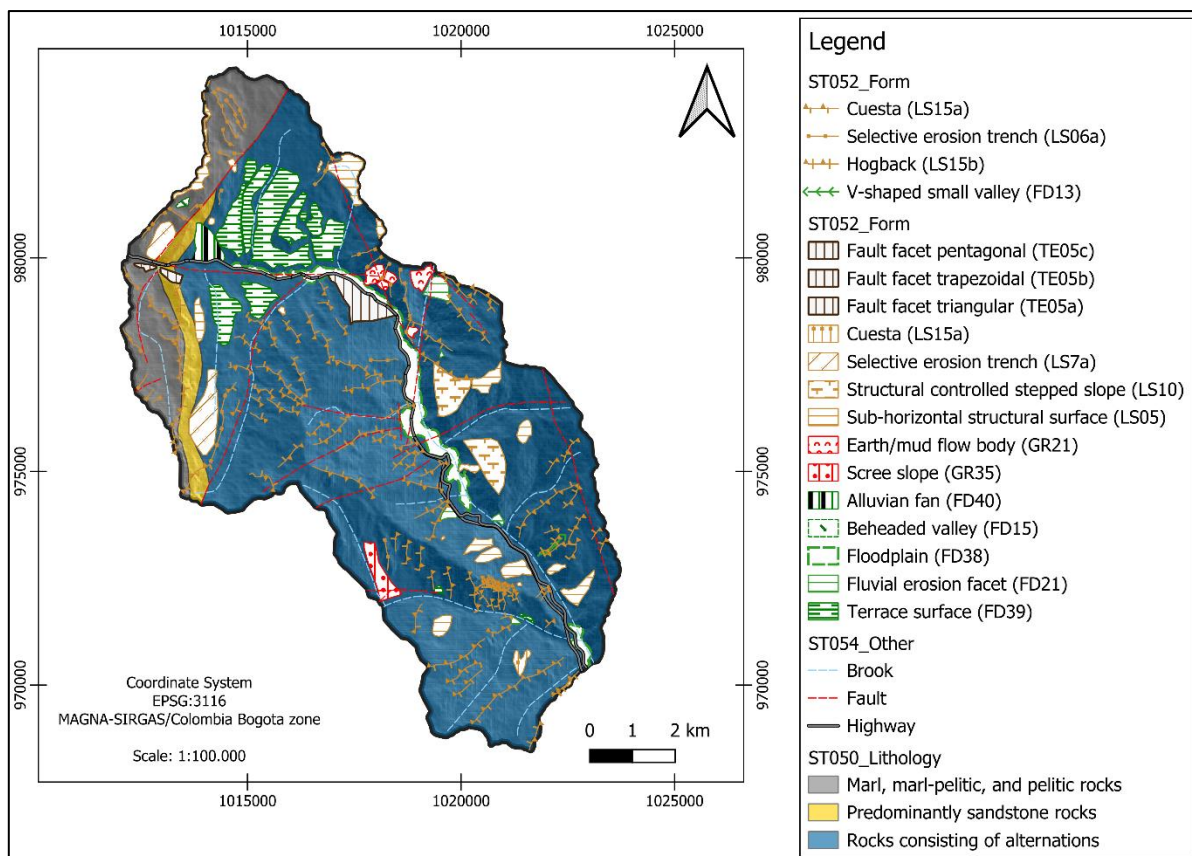


Fig. 50. Geomorphological map of Cáqueza.

Firstly, in this area, we observe a significant change in lithology. Although rocks with alternation persist, metamorphic schist rocks predominantly prevail. This change is also reflected in the landforms, as gravitational landforms predominate here. In the northern part, within the alternating lithology (blue color), slow movements are still observed, while debris flow channels prevail in the southern part of the area. Additionally, on other slopes, there are bodies of rotational and translational movements, along with their scarps, specifically in the Monterredondo area. Significant-sized debris cones and scree slopes are also found in the central part (Fig. 51).

As for fluvial landforms, alluvial terraces have been identified in the northern and central parts of the area, with one of these terraces, specifically in the central part, housing the urban area of Quetame. Fluvial erosion facet due to fluvial erosion are found in other areas. Moreover, floodplain areas of the Negro River have been identified in both the central and southern parts of the area. An alluvial fan is also identified in this southern part, precisely where the urban area of Guayabetal is located (Fig. 51).

Lastly, within the lito-structural landforms, the presence of some flat slopes with inclinations is observed, possibly associated with structural planes. Additionally, in the highest parts of the mountainous landscape, crests and trenches associated with differential erosion within the metamorphic body are found (Fig. 51).

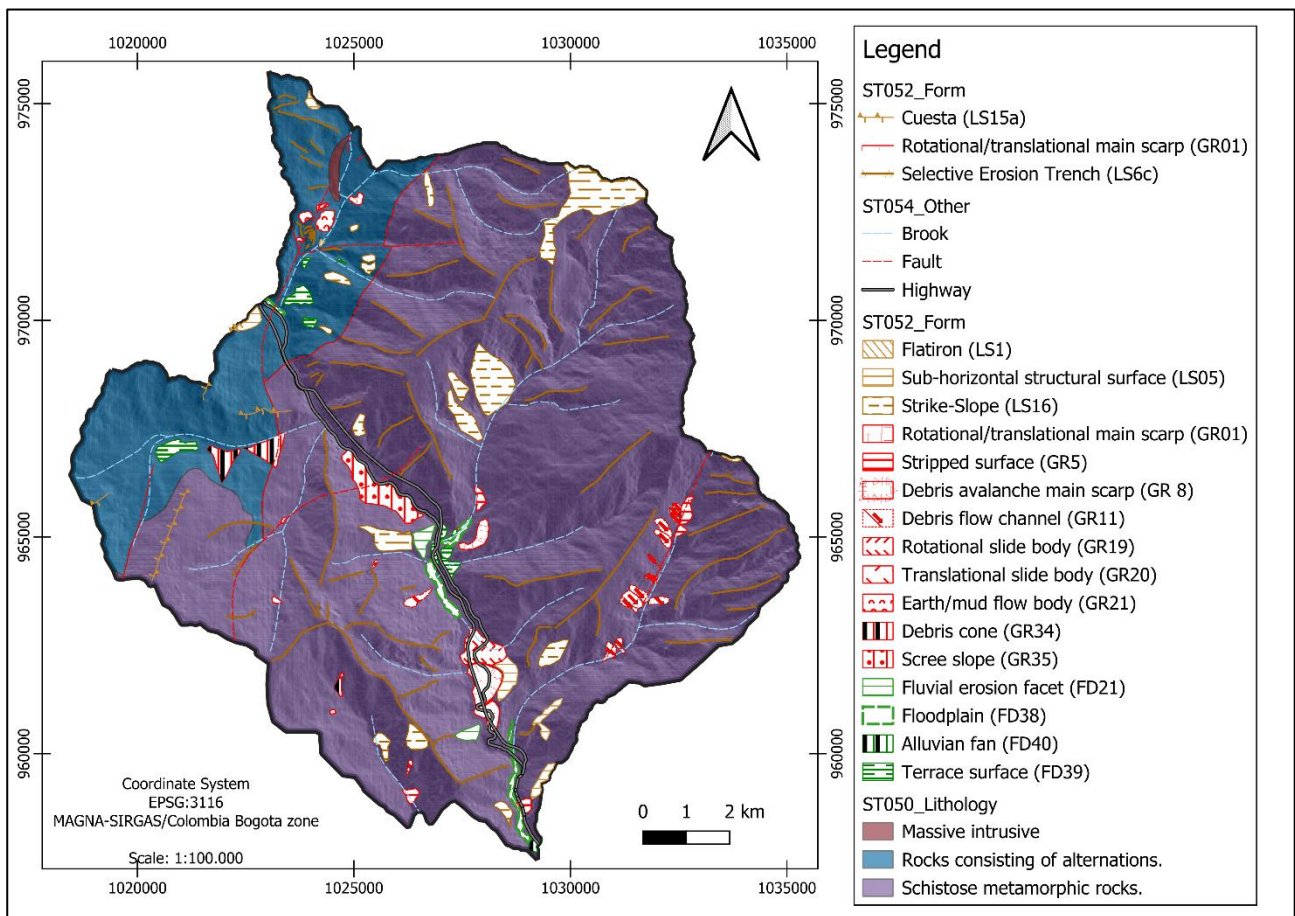


Fig. 51. Geomorphological map of Quetame.

In the area, metamorphic schist rocks are prevalent in the northern part, while arenitic rocks predominate in the south. For this reason, gravitational landforms continue to prevail in the area, especially in the northern area, where the presence of several debris flows and landslide bodies, as well as stripped surfaces, is observed. Additionally, debris cones were identified along with scree slopes both to the north and south of the area (Fig. 52).

Near the Rio Negro, fluvial landforms such as terraces and floodplains are observed. At the beginning of the road entrance into the area, on the west side, an anthropogenic terraced area is observed next to an alluvial fan, as the road passes over these. Additionally, there are two facets of fluvial erosion, where both the highway and the Rio Negro runs between them. However, there are debris flow channels on these slopes (Fig. 52). Finally, in relation to structural areas, some crests of selective erosion were identified in both the northern and southern areas, as well as structural surfaces (Fig. 52).

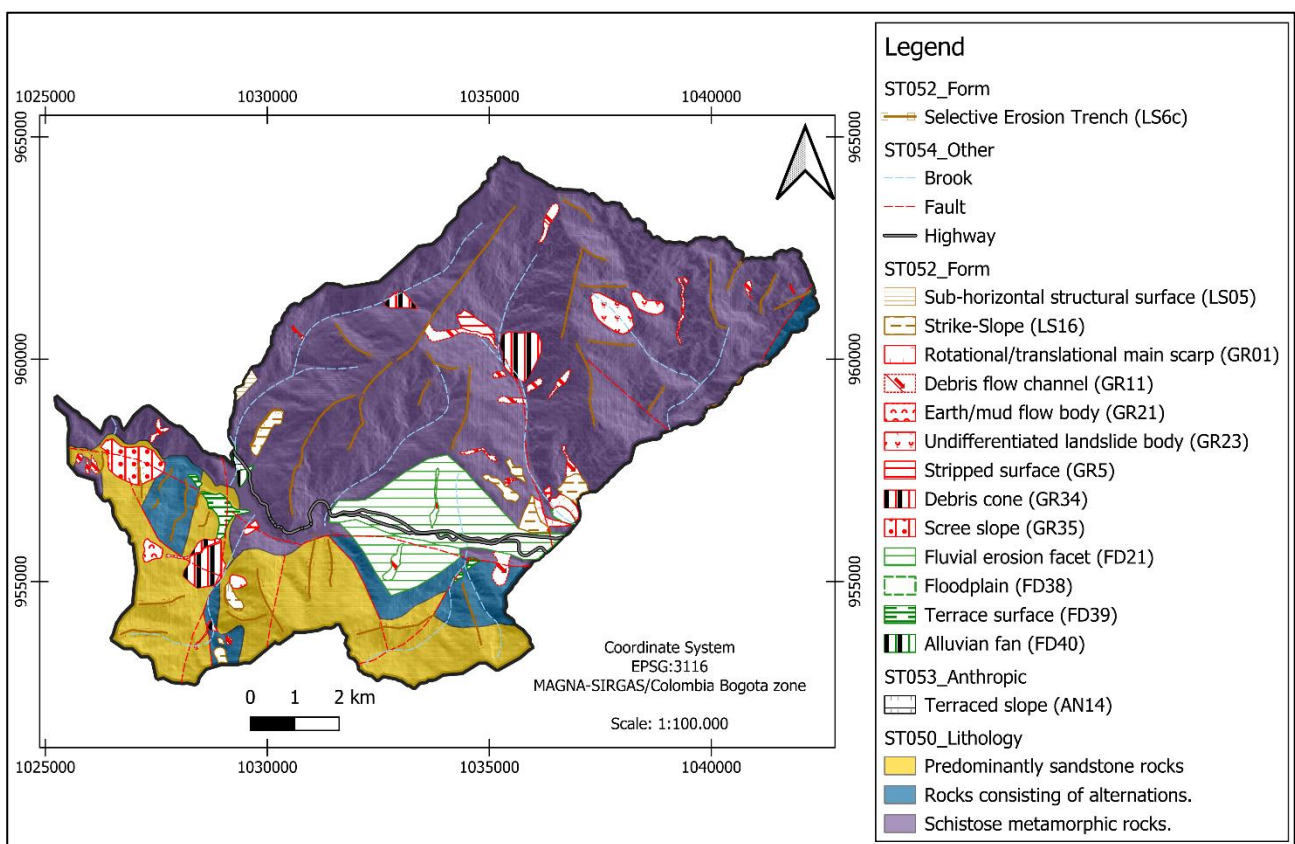


Fig. 52. Geomorphological map of Guayabetal.

In the area of Villavicencio, several geological formations converge, within which three are grouped in lithologies of rocks constituted by alternations. These are the Lutitas de Pipiral Formation, the Lutitas de Macanal Formation, and the Capas Rojas del Guatiquia Formation. Then, a band of arenitic rocks belonging to the Gutiérrez Sandstone Formation passes through the alternation rocks. Finally, in the eastern part, the lithotype related to conglomerates (ruditic rocks), known as the Buenavista Breccia Formation, is identified (Fig. 53).

Although gravitational processes had previously been related to metamorphic schist rocks, here, in both alternating rocks and sandstones, we observe the presence of debris flows, along with colluvial deposits such as scree slopes and debris cones. Additionally, within the ruditic rocks (conglomerates), we observe the initiation of two large debris flows (Fig. 53).

Regarding fluvial landforms, at the end of the road, we see the beginning of the Guayuriba River, where fluvial deposits, terrace landforms and the floodplain area of the river are present. Additionally, the highway crosses gravitational deposits and some fluvial landforms, located on the west side of the area. Lastly, concerning structural landforms, some crests of selective erosion and areas of structural planes were identified (Fig. 53).

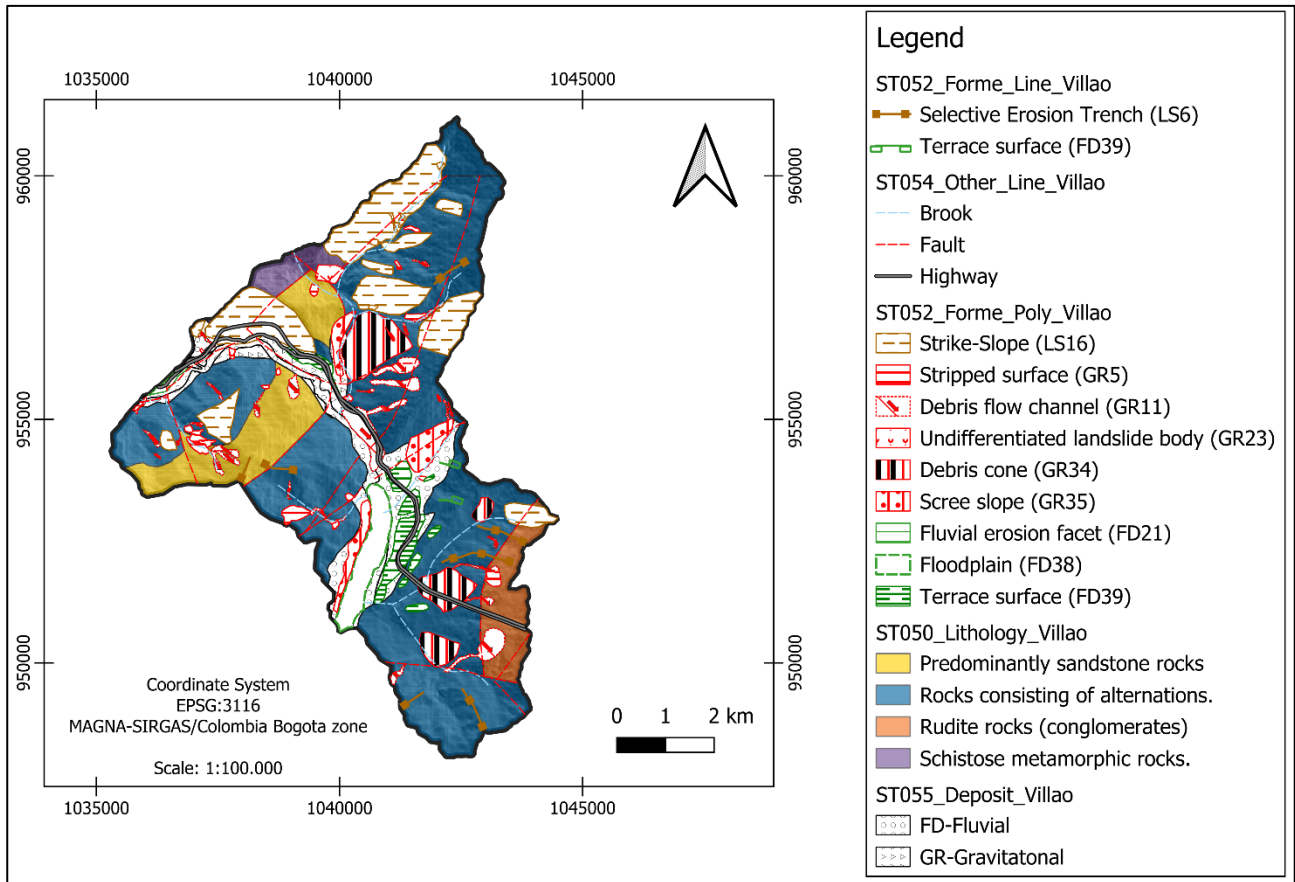


Fig. 53. Geomorphological map of Villavicencio.

5.2. Pluviosity maps

As a result of interpolating the annual averages from each station, the map of the annual average precipitation in the area was obtained (Fig. 56). This reveals values ranging from 500mm to 7000mm per year in different areas of the study zone. Overall, precipitation increases towards the southeastern or final part of the road, near the city of Villavicencio. Meanwhile, the lowest amount of precipitation is observed near the city of Bogota.

According to the data in Table 10 and the twelve-monthly maps obtained (Fig. 54 and 55), it is evident that the month with the highest precipitation is May. Based on the multi-year average monthly precipitation, there are two stations that reach the highest peaks of precipitation in the area in May, which are Servitá and Buenavista with 950mm and 1020mm, respectively. In these stations, during periods of lower precipitation such as January, the lowest average monthly precipitation has been 120mm. This value equals the monthly average of the wettest month (May) for the Juan Rey station in the northwest of the area.

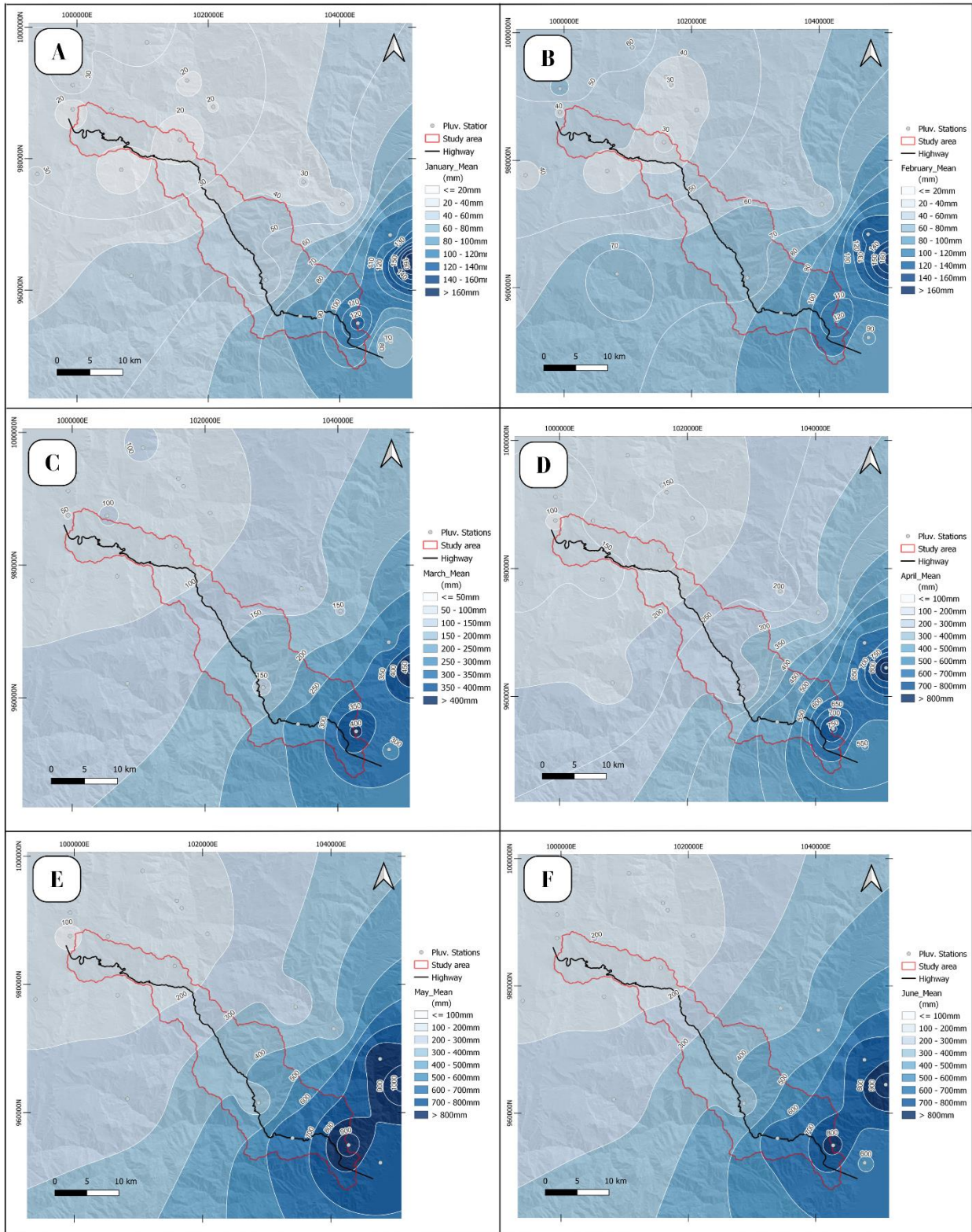


Fig. 54. Multi-year Average Monthly Precipitation Maps from January (A), February (B), March (C), April (D), May (E), and July (F).

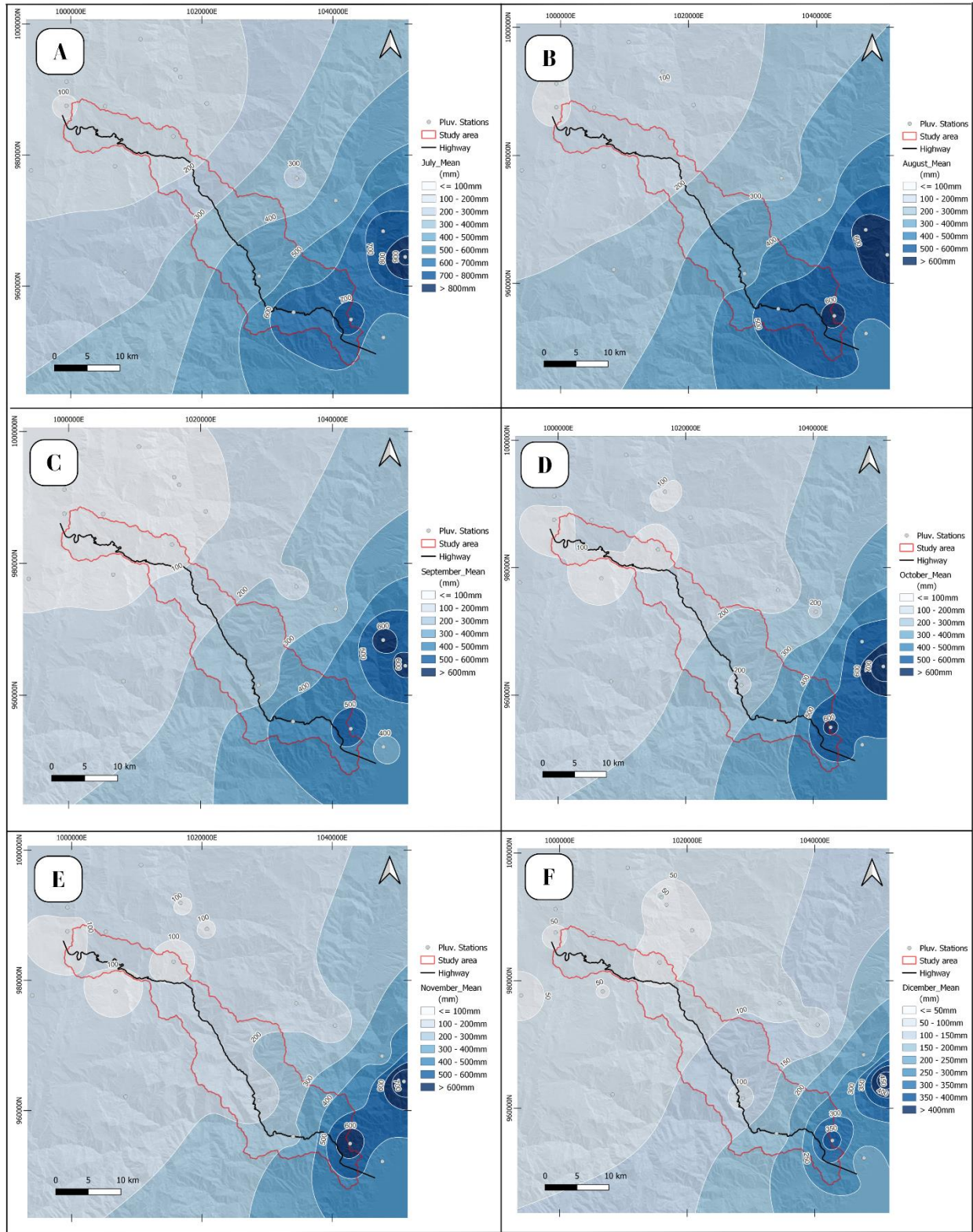


Fig. 55. Multi-year Average Monthly Precipitation Maps from June (A), August (B), September (C), October (D), November (E), and December (F).

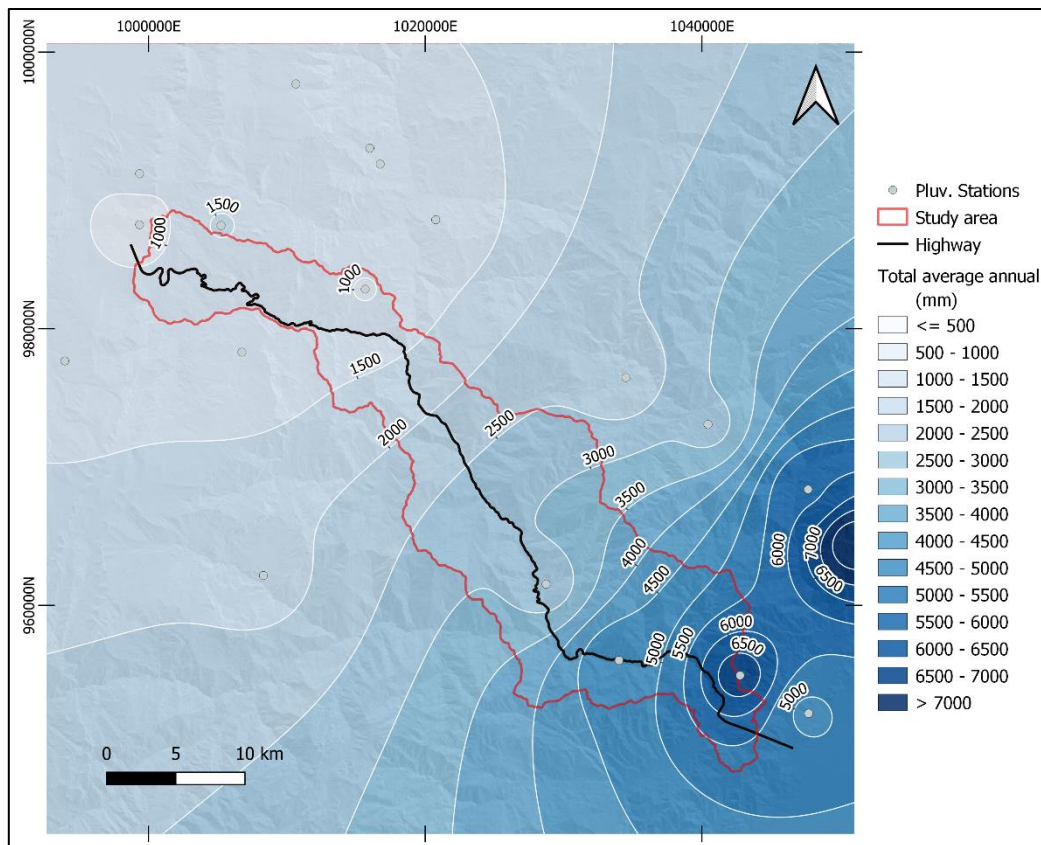


Fig. 56. Annual Average Precipitation Map.

5.3. Landslides inventory

In the area, 2,363 landslides were identified through Google Earth images, of which 196 are in Chipaque, 652 in Caqueza, 1,076 in Quetame, 267 in Guayabetal, and 172 in Villavicencio (Fig. 57A, 58A, 59A, 60A, 61A). Generally, debris flows, debris avalanches, rotational, and translational slides predominated, according to the classification of Hungr et al. (2014).

On the other hand, attempts were made to obtain the inventory of each area automatically using optical and radar images on the Google Earth Engine (GEE) platform. The inventory obtained with NDVI difference with optical images, creates small points, and polygons (Fig. 57C, 58C, 59C, 60C, 61C). In contrast, the inventory with radar images, resulting just in the random distribution of pixels (Fig. 57B, 58B, 59B, 60B, 61B).

Additionally, it is important to note that landslides identified in Chipaque occurred after November 2021, in Caqueza after December 2022, in Quetame after January 2022, in Guayabetal after February 2021, and in Villavicencio after December 2020. The procedure carried out to identify the landslides in each study area with GEE is presented below.

Chipaque: <https://code.earthengine.google.com/429600d2af8dfd1d6e184b42a84a5959>

Caqueza: <https://code.earthengine.google.com/13b0b6ec53ada51f1fa2852218202447>

Quetame: <https://code.earthengine.google.com/795317fc103181768819faf63b987ba8>

Guayabetal: <https://code.earthengine.google.com/8f05eecb381f8099d83d68c1853011f7>

Villavicencio: <https://code.earthengine.google.com/6f9610d55124d6024473e1bab824893a>

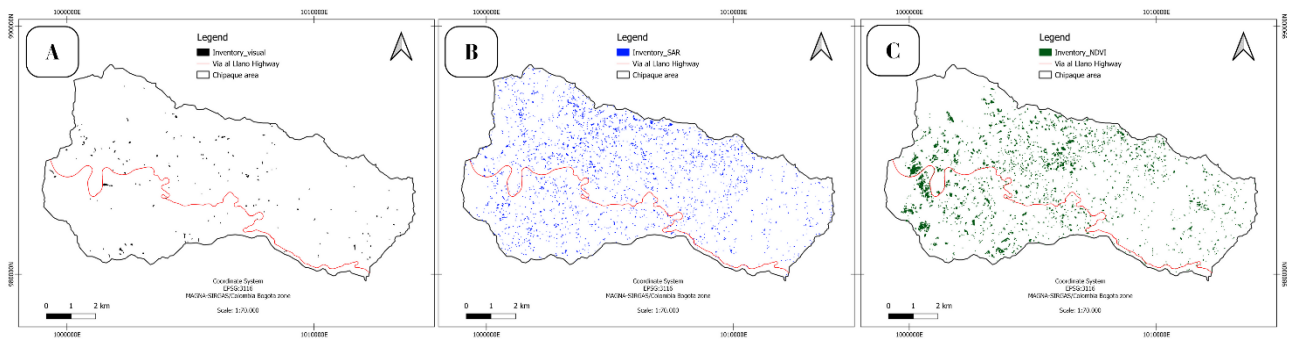


Fig. 57. Inventory of landslides in Chipaque area identified visually (A), automatically using SAR (B), and automatically using NDVI (C).

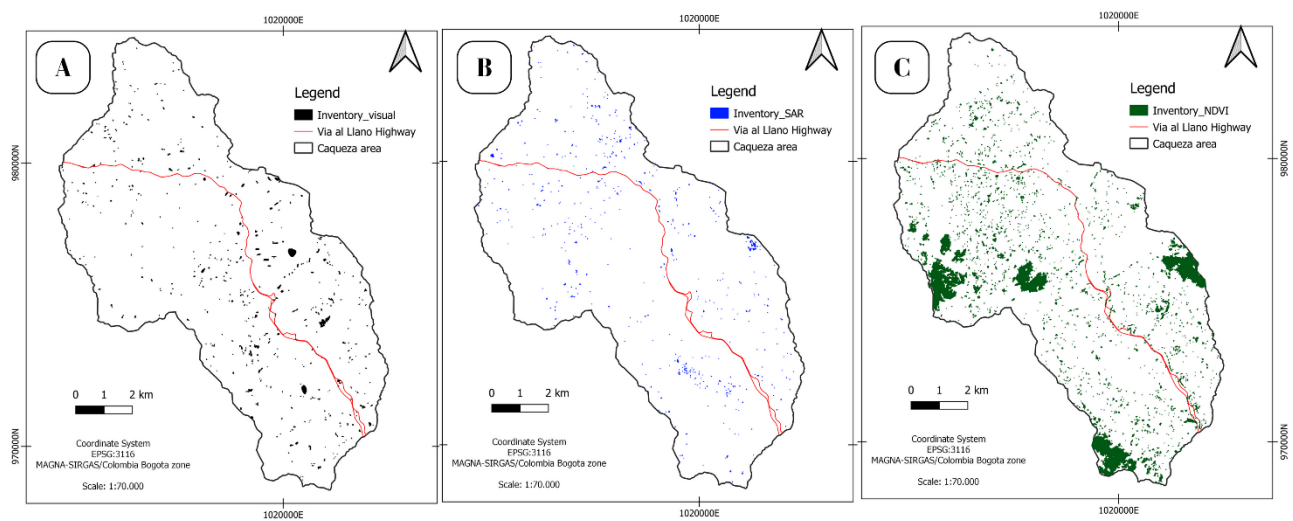


Fig. 58. Inventory of landslides in Caqueza area identified visually (A), automatically using SAR (B), and automatically using NDVI (C).

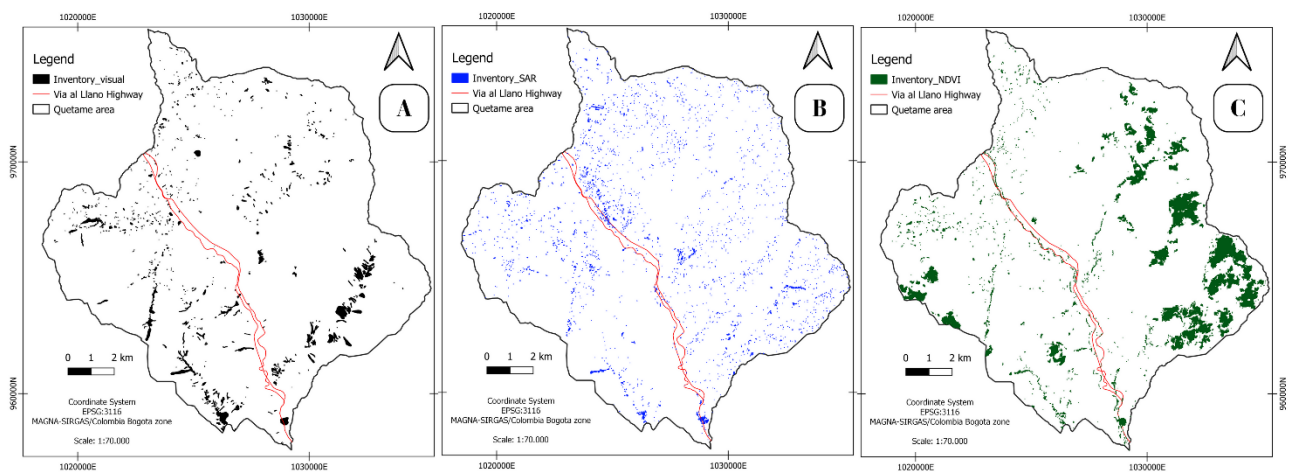


Fig. 59. Inventory of landslides in Quetame area identified visually (A), automatically using SAR (B), and automatically using NDVI (C).

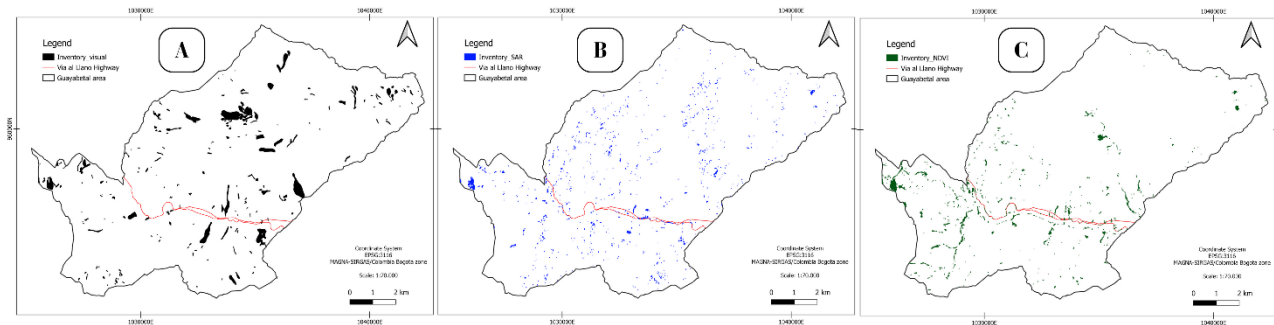


Fig. 60. Inventory of landslides in Guayabatal area identified visually (A), automatically using SAR (B), and automatically using NDVI (C).

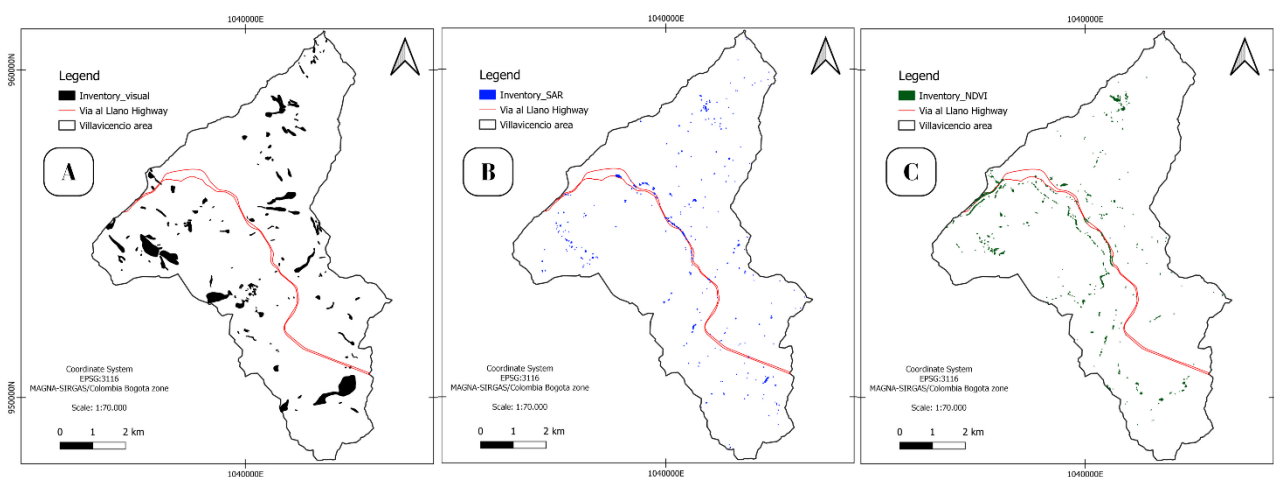


Fig. 61. Inventory of landslides in Villaviciencia area identified visually (A), automatically using SAR (B), and automatically using NDVI (C).

To assess the identification capability of landslides using both optical and radar images, confusion matrices were generated using as reference the inventory generated visually by the expert. These results are represented in Table 12.

Table 12. Evaluation metrics of landslide identification based on visual reference, to assess the results of the inventory created with NDVI and SAR.

		*TP	*FP	*TN	*FN	*N	Sensitivity	Specificity	Precision	Accuracy	kappa	McNemar test
Chip.	NDVI	203	22344	472277	1705	496529	0.1064	0.9548	0.0090	0.9516	0.0096	2.00E-16
	SAR	39	13533	481088	1869	496529	0.0204	0.9726	0.0029	0.9690	-0.0017	2.00E-16
Caque.	NDVI	539	43372	553828	5972	603711	0.0828	0.9274	0.0123	0.9183	0.0026	2.00E-16
	SAR	26	2879	594321	6485	603711	0.0040	0.9952	0.0090	0.9845	-0.0011	2.00E-16
Quet.	NDVI	5428	67470	972997	22678	1068573	0.1931	0.9352	0.0745	0.9156	0.0723	2.00E-16
	SAR	2140	12095	1028372	25966	1068573	0.0761	0.9884	0.1503	0.9644	0.0849	2.00E-16
Guay.	NDVI	2778	6916	630032	20046	659772	0.1217	0.9891	0.2866	0.9591	0.1534	2.00E-16
	SAR	1623	5388	631560	21201	659772	0.0711	0.9915	0.2315	0.9597	0.0941	2.00E-16
Villao.	NDVI	1209	2623	322890	15418	342140	0.0727	0.9919	0.3155	0.9473	0.1018	2.00E-16
	SAR	593	1411	324102	16034	342140	0.0357	0.9957	0.2959	0.9490	0.0538	2.00E-16

*TP: True positive, FP: False positive, TN: True negative, FN: False negative, N: total number of predictions.

In general, there is a lower number of true positives compared to false positives, while the number of true negatives is higher than the number of false negatives. For this reason, sensitivity, which indicates if the images have the ability to detect real landslides, is less than 10%, while specificity is very good at identifying areas where there are no landslides, with a percentage above 90%. This situation is also reflected in precision, which shows high erroneous predictions in identifying landslide areas. Additionally, accuracy has a high value, as this method has high precision in identifying areas without landslides, although it is not good at identifying areas with landslides.

When observing the kappa value, which allows to determine if there is agreement between the classification with GEE and the visual, we see values close to zero and even some negative ones, indicating that the prediction does not match the real predictions, that is, it has poor predictive ability. Finally, with the McNemar test, we see that the value is very small, which rejects the null hypothesis that there is no difference between types of errors. We thus conclude that there are more type 1 errors than type 2 errors, meaning that these images tend to produce more false positives than false negatives.

When comparing the metrics of both NDVI and SAR, it can be observed that the kappa value of NDVI is slightly better than the kappa values of SAR, except for the Quetame area, where the latter had a better prediction. Lastly, when evaluating the 5 areas, those with the worst predictions were Chipaque and Caqueza, while the best prediction was achieved in Guayabetal with NDVI, given the highest kappa value of 0.1534. Despite being the highest kappa value among the data obtained, it remains a poor model for identifying landslides in a historical inventory.

5.4. Importance of predictor variables

Within the predictor variables used to predict landslides, a categorical variable corresponding to lithology is included. This variable varies from one area to another, meaning that some of these categories may be present or absent in the five different municipalities (Table 13). Additionally, 15 continuous variables summarized in Table 14 were used.

Table 13. Categorical variable

Variable name	Abbreviation	ID	Model ID	Description
Lithology	LITO	1	LTL1	Arenisca Dura Fm.
		2	LTL2	Chipaque Fm.
		3	LTL3	Une Fm.
		4	LTL4	Fomeque Fm.
		5	LTL5	Areniscas de Caqueza Fm.
		6	LTL6	Lutitas de Macanal Fm.
		7	LTL7	Capas Rojas del Guatiquia Fm.
		8	LTL8	Brechas de Buenavista Fm.
		9	LTL9	Lutitas de Pipiral Fm
		10	LTL10	Areniscas de Gutierrez Fm.
		11	LTL11	Quetame Group
		12	LTL12	Rhyodacite
		13	LTL13	Deposits

Table 14. Continues variables of topographic attributes.

Variable name	Abbreviation	Description
Elevation	ELE	Altitude in meters
Slope	SLO	Maximal rate of change of elevation values between horizontal and tangential planes (Zevenbergen & Thorne, 1987).
Plan curvature	PCV	Convergence and divergence of a normal section on the surface (Dikau, 1988).
Profile curvature	PRC	Relative deceleration or acceleration of flow according to a profile plane which cuts the surface (Shary, 1995).
Convergence index	CVI	Smoother plan curvature outcomes. (Köthe et al., 1996; Watkins, 2019).
LS Factor	LSF	Slope length using the slope gradient and the slope length factor (RUSLE equation) (Desmet & Govers, 1996).
Stream power index	SPI	Flow erosion potential, considering the amount of water contributed by the upslope area and the velocity of water flow. (Gruber & Peckham, 2009).
Topographic position index	TPI	Classification of the landscapes into slope position classes. (Weiss, 2001).
Topographic wetness index	TWI	Water accumulation tendency based on specific catchment area and the local slope angle (Quinn et al., 1995).
Vertical distance to channel network	VDCN	It constitutes a theoretical surface regarding the channel lines ("base level") (Bock & Köthe, 2008).
Northness	N	Cosine of slope direction
Eastness	E	Sine of slope direction
Pluviosity	PLV	Mean total annual precipitation
Normalized Difference Vegetation Index	NDVI	Index of vegetation health and density (Rouse, et al., 1974).

After splitting the landslide inventory into calibration and validation groups, comprising 75% and 25% of the landslides, respectively, we applied the Multivariate Adaptive Regression Splines (MARS) model. This statistical method was conducted on the ten-training dataset of each subset (SUP, INF, and BODY) for each municipality, including the same number of presences and absences, the latter randomly selected from stable slopes.

The importance of each variable in the models was determined based on the mean Residual Sum of Squares (RSS) across the ten repetitions (Fig.62 to 66). RSS measures the variability in a dataset by summing the squares of the differences between observed and model-estimated values (Milborrow, 2021). Following the Earth code notes (Milborrow, 2021), the criterion involved calculating the decrease in RSS for each subset compared to the previous one. These subset decreases were then summed and normalized, with the largest decrease set to 100. Consequently, variables causing the greatest net decreases in RSS were considered more important.

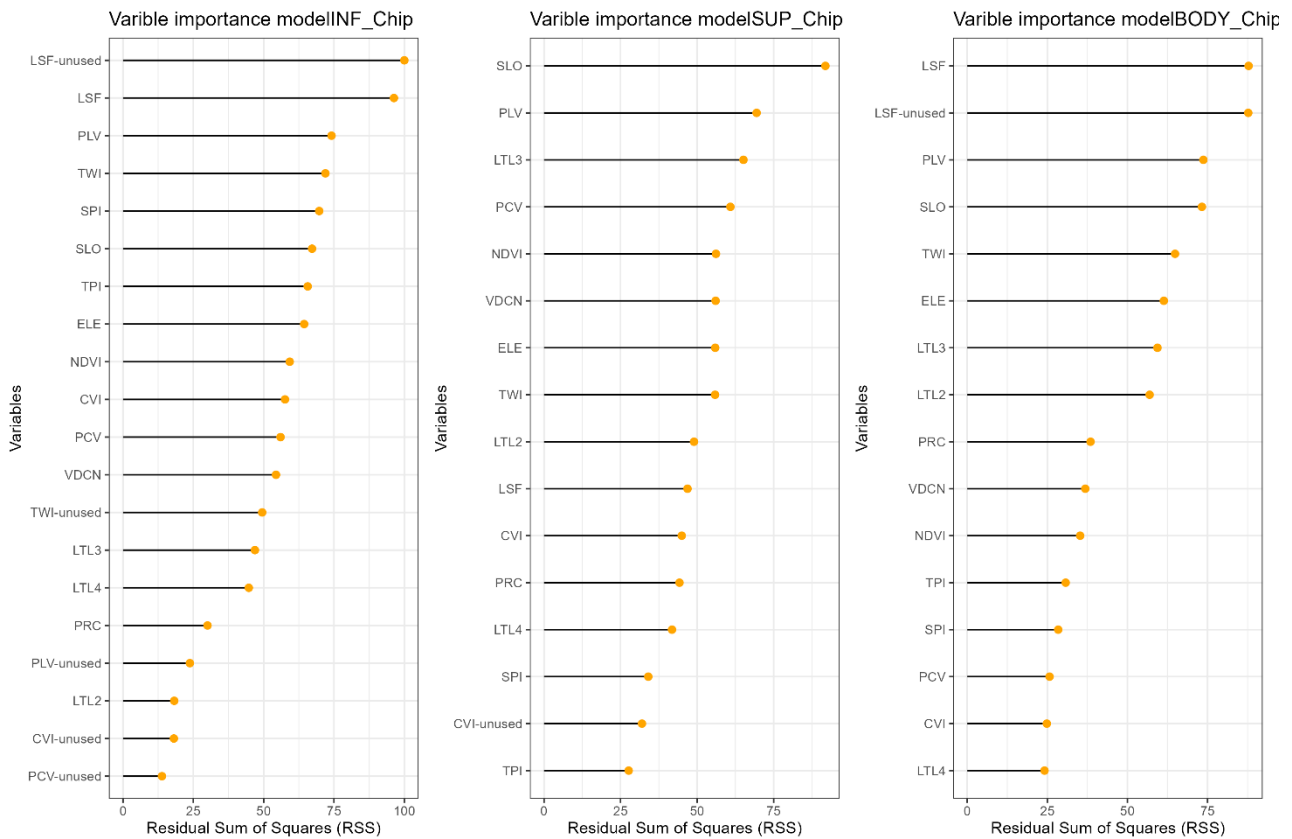


Fig. 62. Importance variables on each model (INF, SUP, and BODY) for Chipaque, after applying MARS modeling.

According to the RSS values, in the Chipaque area, the most important variables for predicting the deposit areas (INF) and the entire landslide (BODY) are LSF and PLV. Conversely, for predicting detachment areas (SUP), the most important variables are SLO, PLV, and LTL3 (Fig. 62). In this area, we can observe that precipitation data (PLV) plays an important role in predicting landslides, along with the LS Factor (LSF) and slope (SLO).

In the Caqueza area, the most significant variables for predicting INF and BODY are LSF and NDVI. Instead, for predicting SUP, the most crucial variables are SLO, NDVI, and PLV LTL3 (Fig. 63). In this region, we observe a similarity with Chipaque, but with NDVI replacing PLV. However, PLV maintains its significance as the third most important variable in SUP and BODY.

The variable importance for predicting the initial movement locations (SUP) in Quetame, Guayabetal, and Villavicencio highlights NDVI, SLO, and ELE as the most crucial variables. In Quetame, NDVI and ELE take precedence (Fig. 64), while in Guayabetal and Villavicencio, it is NDVI and SLO that are most significant (Fig. 65 and 66).

For predicting INF and BODY areas in Quetame, the most important variables remain the same for both: TPI, NDVI, and ELE (Fig. 64). In contrast, in Guayabetal and Villavicencio, TPI and VDCN are the primary predictors for deposit areas (INF), respectively. However, NDVI still holds significance as the second most important variable (Fig. 65 and 66).

When predicting the entire area (BODY) in Guayabetal and Villavicencio, NDVI emerges as the most crucial variable. Following this, ELE and LSF are significant in Guayabetal (Fig. 65), while LSF and VDCN are crucial in Villavicencio (Fig. 66).

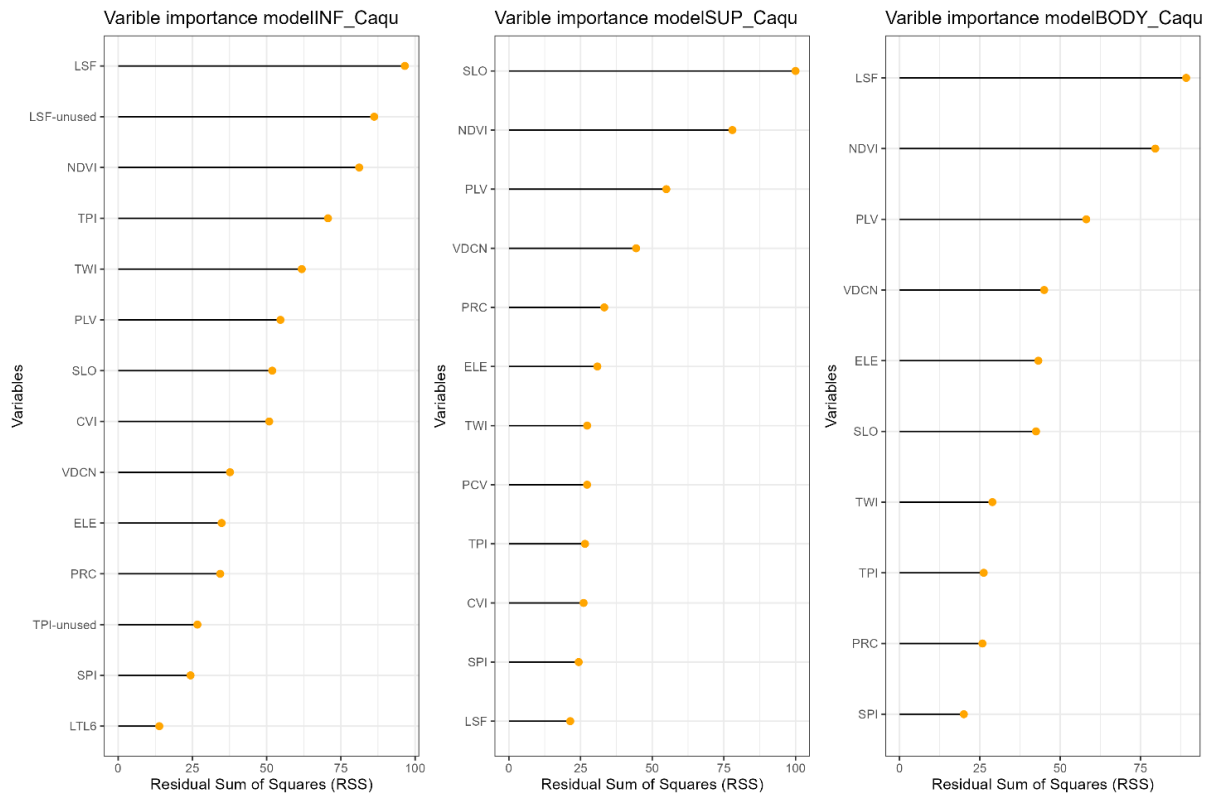


Fig. 63. Importance variables on each model (INF, SUP, and BODY) for Caqueza, after applying MARS modeling.

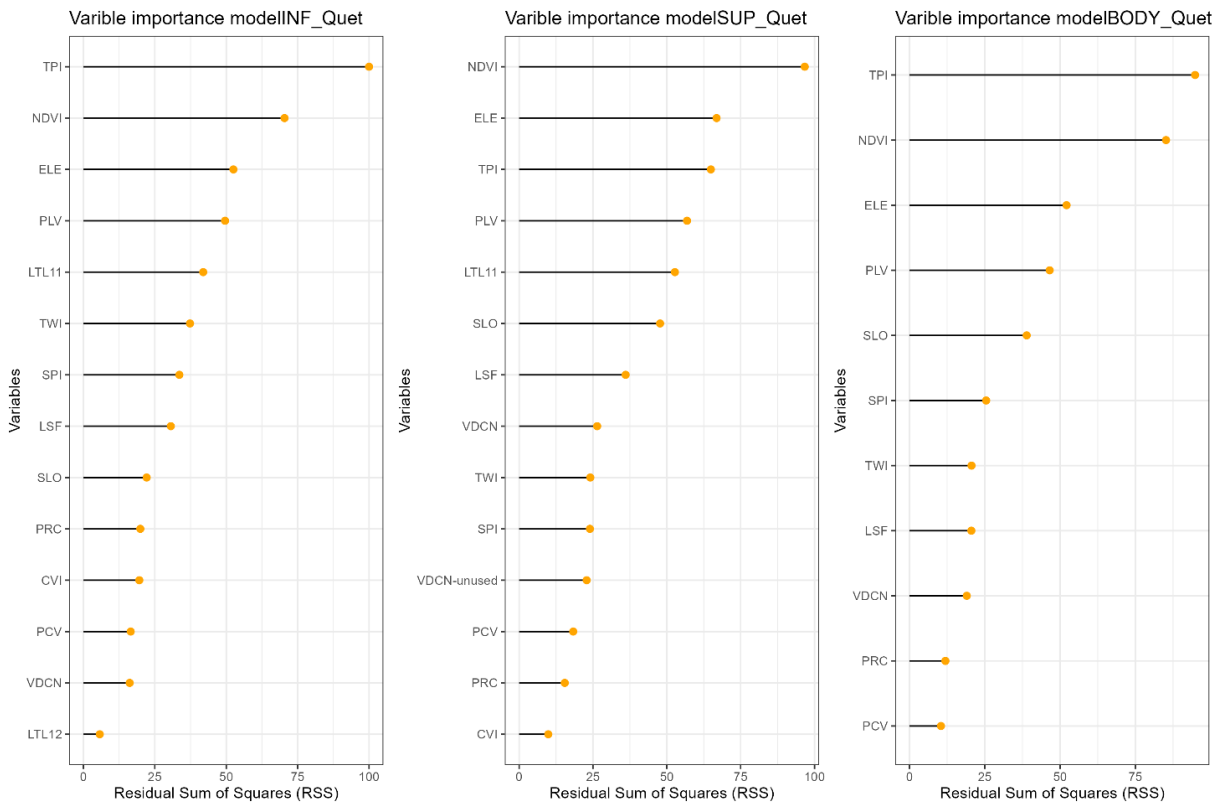


Fig. 64. Importance variables on each model (INF, SUP, and BODY) for Quetame, after applying MARS modeling.

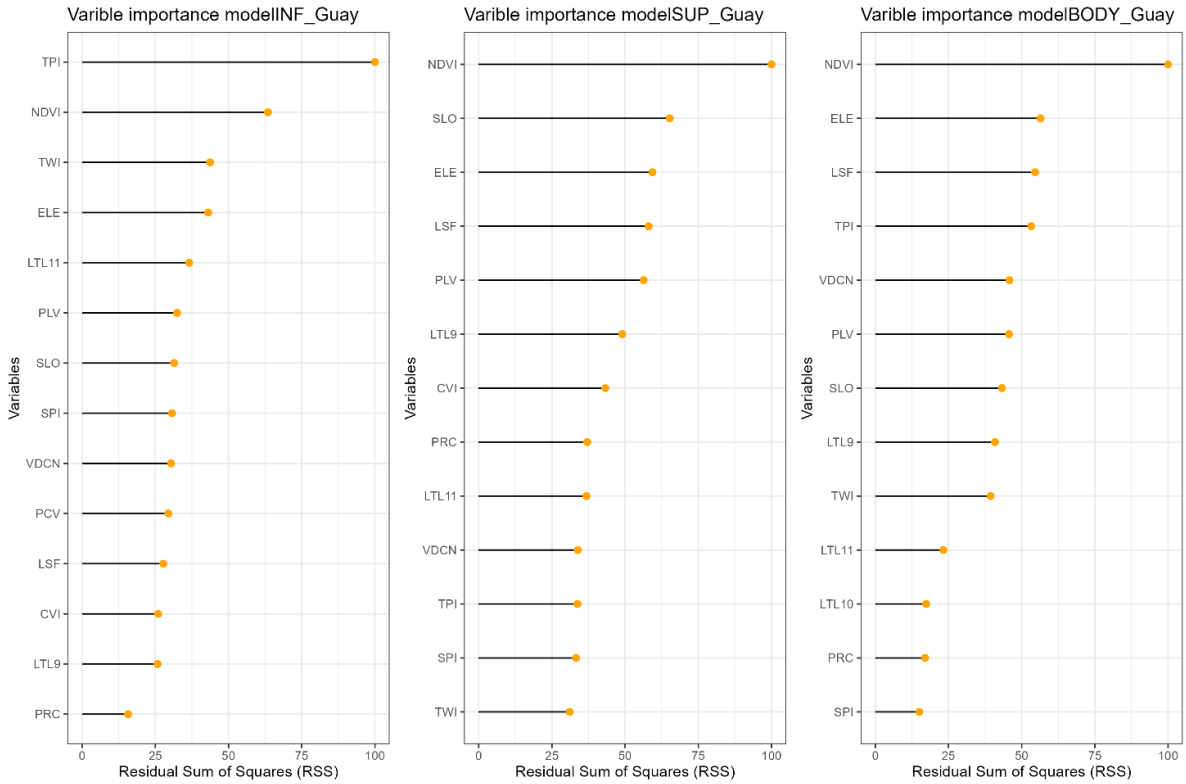


Fig. 65. Importance variables on each model (INF, SUP, and BODY) for Guayabetal, after applying MARS modeling.

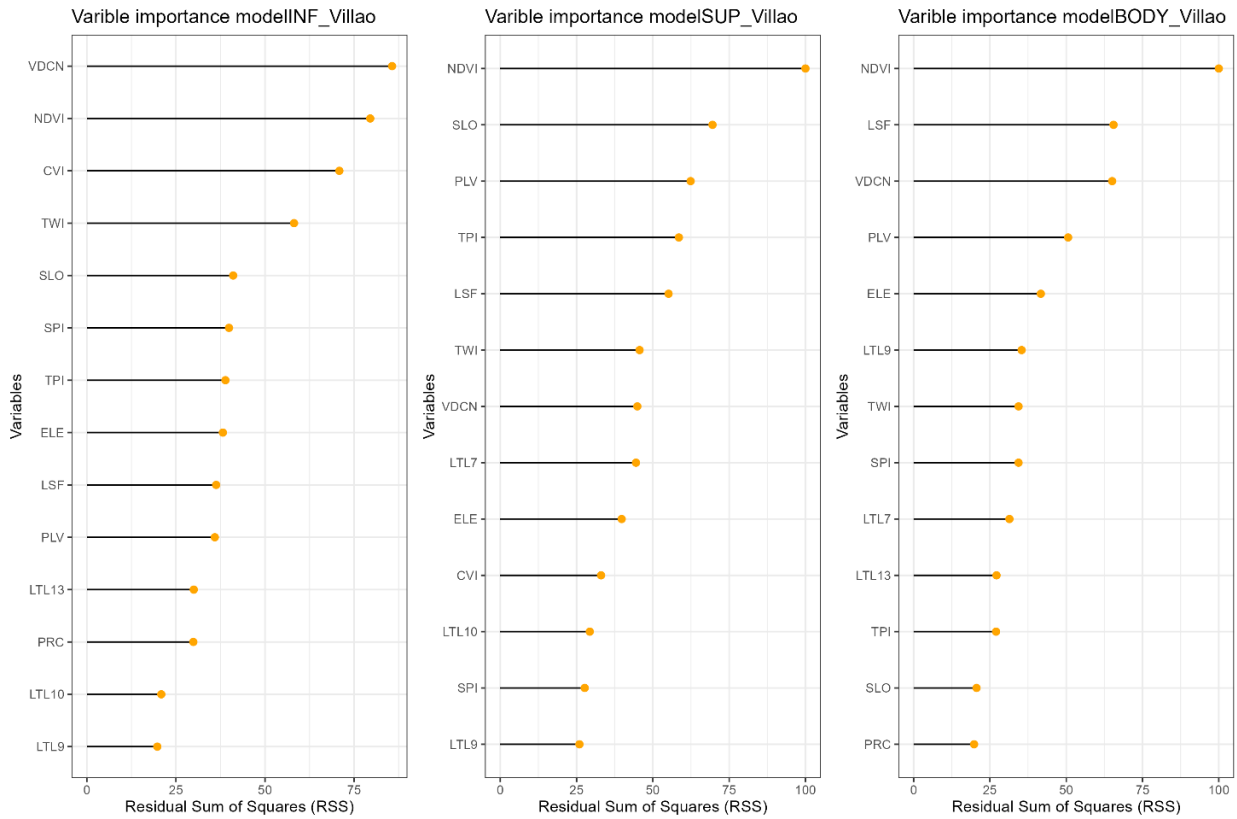


Fig. 66. Importance variables on each model (INF, SUP, and BODY) for Villaviecio, after applying MARS modeling.

5.5. Validation of the models

The predictive skill of the models of each subset was assessed using the validation subsets of landslides, which correspond to the 25% of each data set. This process is comparable to predicting potential future landslides in the area. Through this evaluation, we aim to measure the accuracy of the models in predicting each area prone to mass movements.

According to the assessment of the models in Chipaque, the INF model demonstrates the best predictive performance for determining the entire landslide area (BODY), with an average AUC of 0.74. However, it exhibits a relatively high standard deviation of 0.06 compared to standard deviations of other models (Fig. 67 and Table 15). Overall, the BODY, INF, and SUP models provide significantly better predictions for the entire landslide area (BODY) compared to the deposit areas (INF) and landslide initiation (SUP) areas. Moreover, they are the only ones deemed acceptable for landslide prediction in the area, as they exceed the 0.70 AUC threshold. In conclusion, these three models are only reliable for predicting the landslide area (BODY), as they are not reliable to predict the INF and SUP areas.

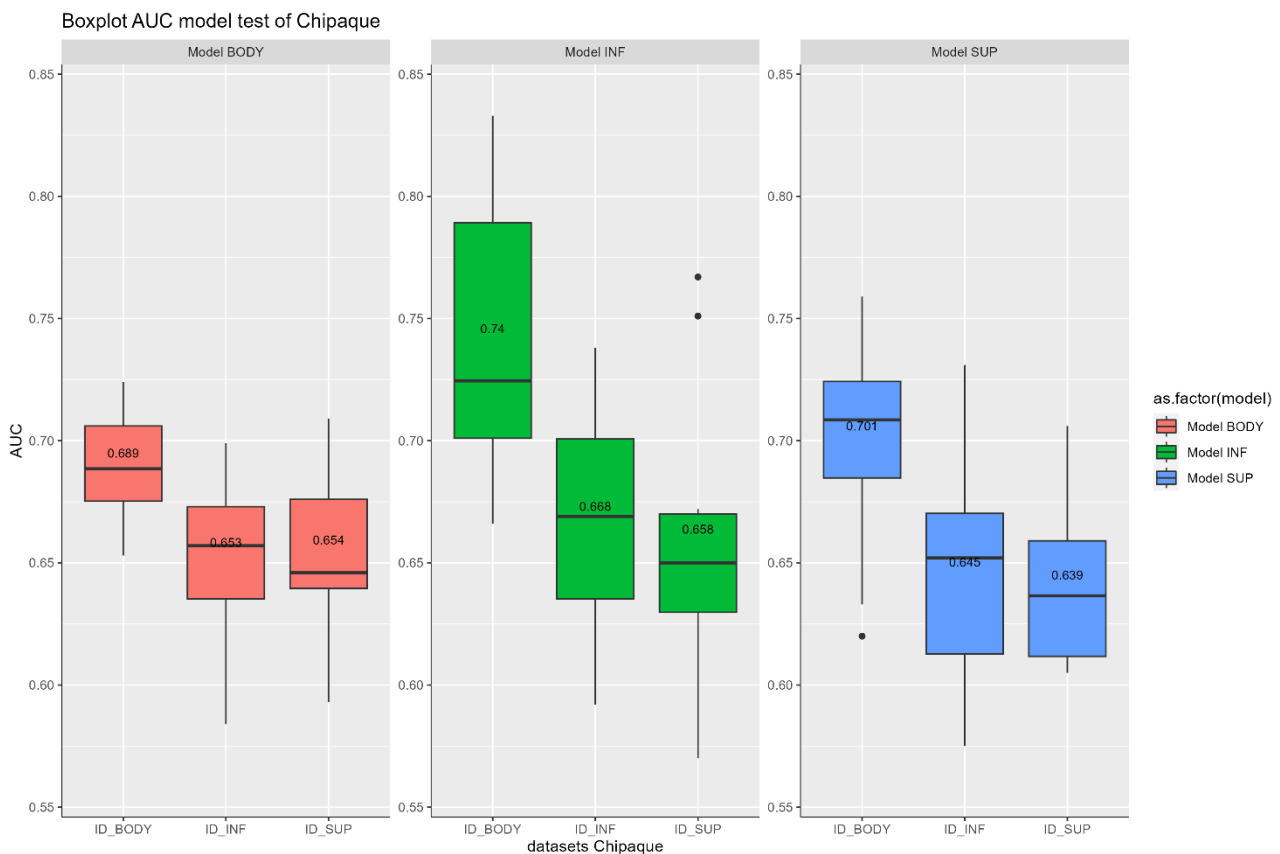


Fig. 67. Boxplot of the AUC for each model applied to the BODY, INF, and SUP test datasets of Chipaque.

Table 15. Mean and standard deviation (SD) of the AUC from 10 repetitions of each model applied to every database in Chipaque.

		AUC_Test_database Chipaque			AUC_Train_database Chipaque		
Dataset		BODY	INF	SUP	BODY	INF	SUP
Model BODY	Mean	0.689	0.653	0.654	0.765	0.660	0.660
	SD	0.025	0.034	0.032	0.016	0.027	0.013
Model INF	Mean	0.740	0.668	0.658	0.740	0.784	0.644
	SD	0.060	0.048	0.062	0.039	0.040	0.040
Model SUP	Mean	0.701	0.645	0.640	0.705	0.632	0.787
	SD	0.046	0.048	0.032	0.031	0.030	0.035

In the case of Caqueza, it is again observed that the INF model has a better performance, specifically for predicting the entire landslide area (BODY), with an average of 0.754 AUC. However, the BODY model has an average of 0.748, with a lower standard deviation of 0.016 compared to that of the INF model, which is 0.023 (Fig. 67 and Table 15). Overall, it is observed that the BODY model has an acceptable capacity to predict all three landslide areas (INF, SUP, and BODY), while the INF model is only acceptable for predicting the BODY and INF areas, and the SUP model is acceptable only for predicting the BODY and SUP areas. Nonetheless, it is seen that the best overall values are obtained for predicting the entire landslide area (BODY).

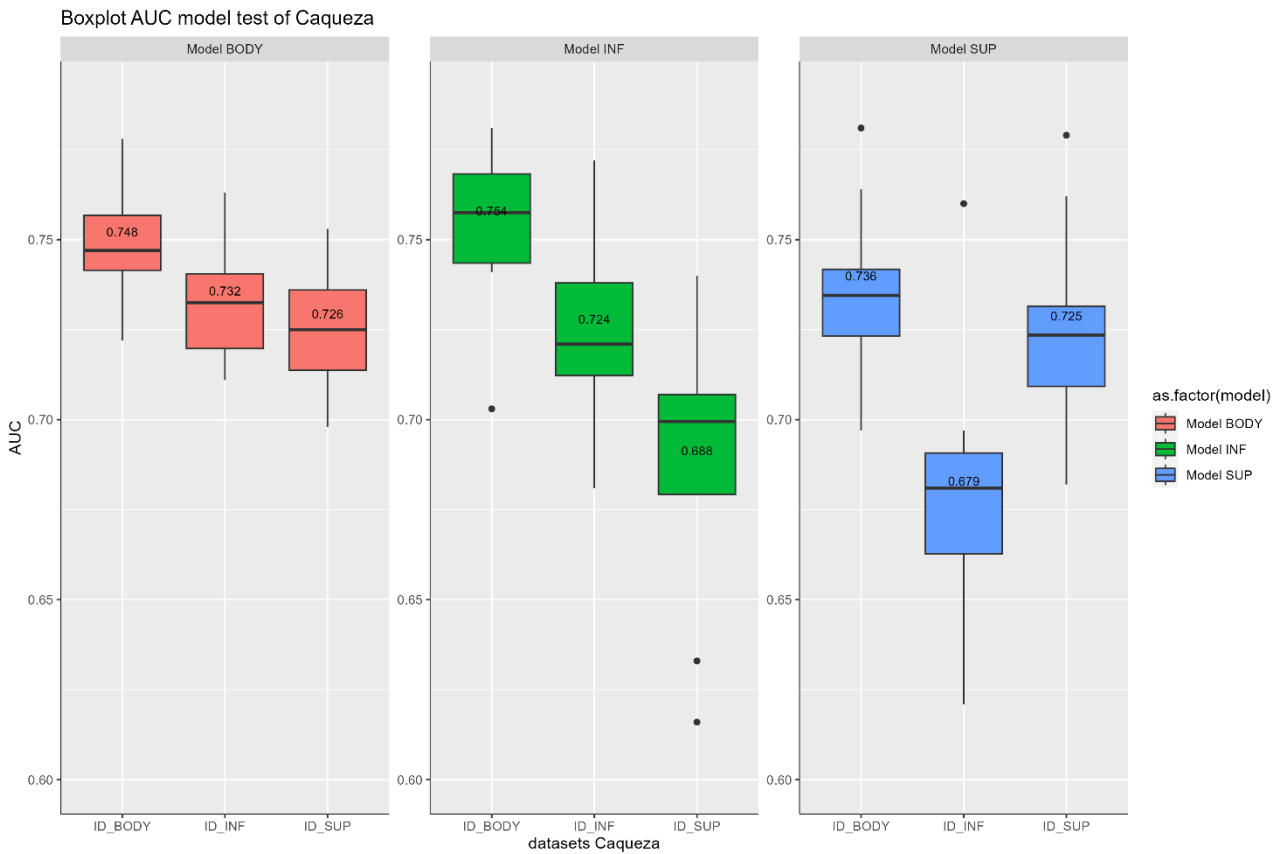


Fig. 68. Boxplot of the AUC for each model applied to the BODY, INF, and SUP test datasets of Caqueza.

Table 16. Mean and standard deviation (SD) of the AUC from 10 repetitions of each model applied to every database in Caqueza.

Dataset		AUC_Test_database Caqueza			AUC_Train_database Caqueza		
		BODY	INF	SUP	BODY	INF	SUP
Model BODY	Mean	0.748	0.732	0.726	0.7713	0.726	0.7225
	SD	0.016	0.015	0.019	0.0059	0.0053	0.0105
Model INF	Mean	0.754	0.724	0.688	0.7562	0.7885	0.6996
	SD	0.023	0.024	0.038	0.0104	0.0102	0.0164
Model SUP	Mean	0.736	0.679	0.725	0.7357	0.694	0.7738
	SD	0.023	0.037	0.028	0.0136	0.0168	0.0096

In the Quetame area, the models demonstrate a superior predictive capacity, with mean AUC values exceeding 0.8. The INF model exhibits the highest AUC values for predicting both the entire landslide (BODY) and deposit areas (INF), with means of 0.833. As for the BODY model, its highest mean AUC of 0.8 is observed for predicting the BODY area, while mean AUC values for predicting INF and SUP are similar, at 0.779 and 0.778, respectively. However, the SUP model falls below 0.75 in predicting any landslide area. Therefore, for a more reliable prediction of detachment areas (SUP), it is preferable to use the BODY model.

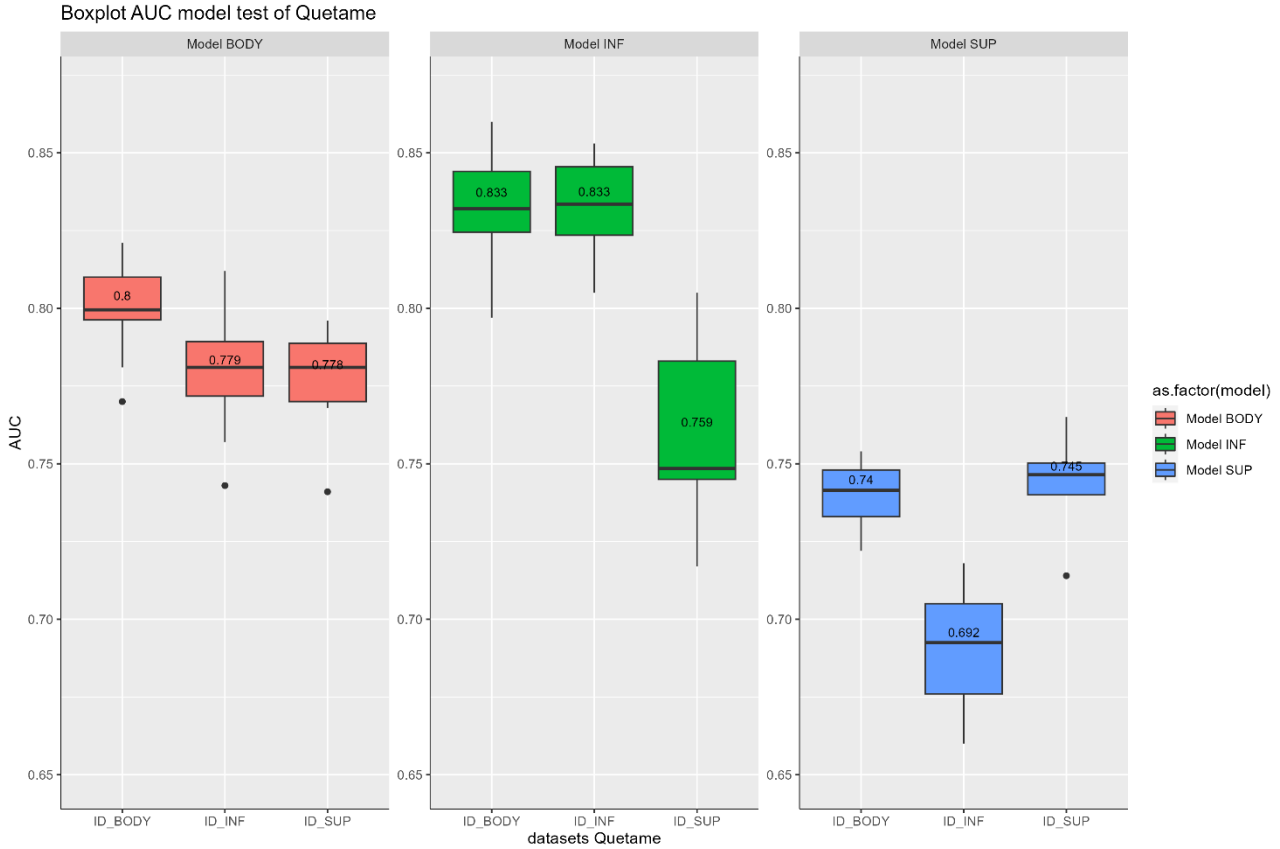


Fig. 69. Boxplot of the AUC for each model applied to the BODY, INF, and SUP test datasets of Quetame.

Table 17. Mean and standard deviation (SD) of the AUC from 10 repetitions of each model applied to every database in Quetame.

Dataset		AUC_Test_database Quetame			AUC_Train_database Quetame		
		BODY	INF	SUP	BODY	INF	SUP
Model BODY	Mean	0.800	0.779	0.778	0.805	0.776	0.772
	SD	0.016	0.020	0.016	0.005	0.004	0.011
Model INF	Mean	0.833	0.833	0.759	0.823	0.845	0.757
	SD	0.018	0.015	0.028	0.009	0.008	0.026
Model SUP	Mean	0.741	0.692	0.745	0.757	0.703	0.783
	SD	0.011	0.019	0.014	0.011	0.012	0.013

In the case of Guayabetal, we observe a behavior similar to that of the Quetame models, where the INF model achieves the highest AUC values for predicting both the entire landslide area (BODY) and deposit areas (INF). However, when predicting the detachment area of landslides (SUP), it is ideal to use the SUP model, as it has a better mean value than the BODY model. Nonetheless, the BODY model exhibits a lower standard deviation (0.013) compared to the SUP model (0.027) for predicting SUP.

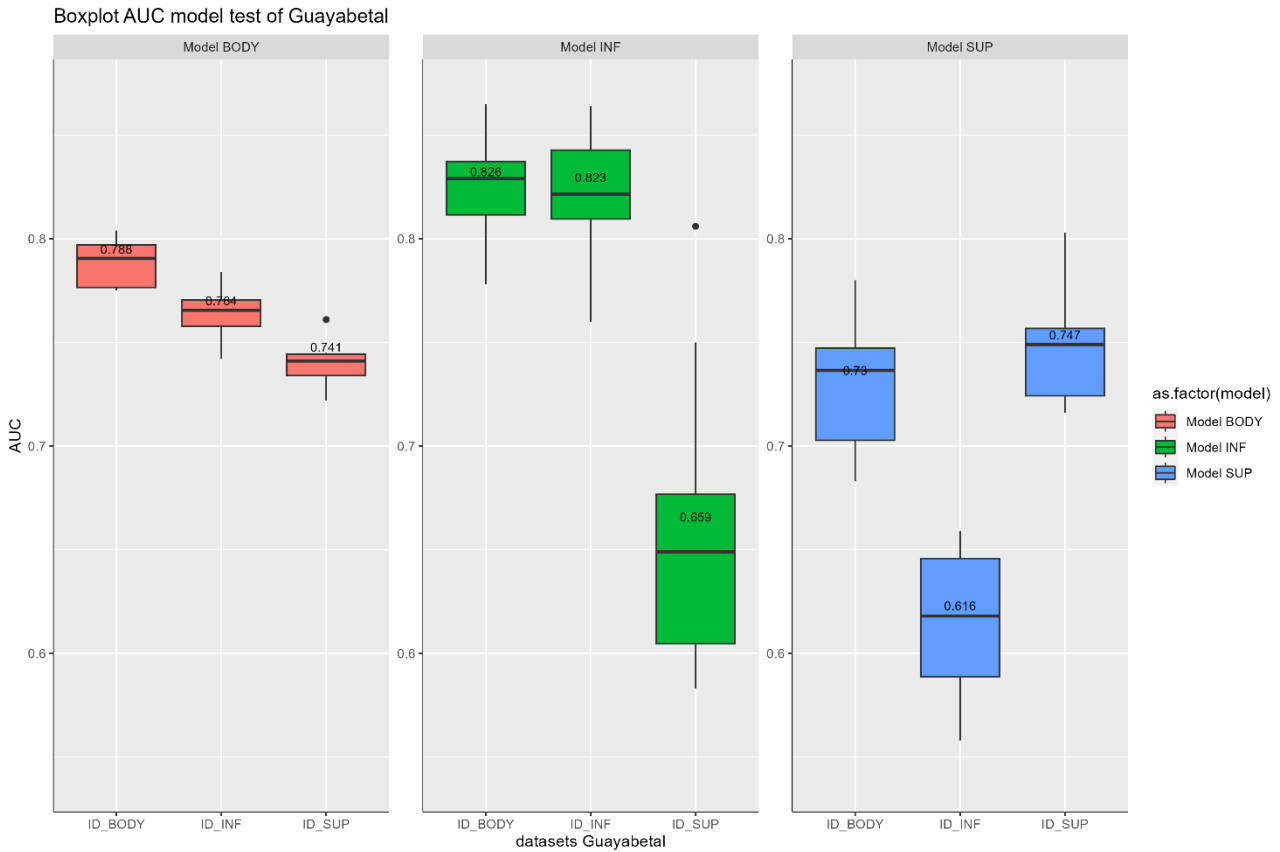


Fig. 70. Boxplot of the AUC for each model applied to the BODY, INF, and SUP test datasets of Guayabetal.

Table 18. Mean and standard deviation (SD) of the AUC from 10 repetitions of each model applied to every database in Guayabetal.

Dataset		AUC_Test_database Guayabetal			AUC_Train_database Guayabetal		
		BODY	INF	SUP	BODY	INF	SUP
Model BODY	Mean	0.788	0.764	0.741	0.8127	0.7553	0.7343
	SD	0.011	0.012	0.013	0.0038	0.0117	0.0207
Model INF	Mean	0.826	0.823	0.659	0.8185	0.8722	0.6371
	SD	0.025	0.031	0.072	0.014	0.0065	0.0369
Model SUP	Mean	0.730	0.616	0.747	0.7339	0.6305	0.8042
	SD	0.034	0.036	0.027	0.0139	0.0216	0.0132

For the Villavicencio area, the best prediction averages, with values exceeding 0.8 of AUC, are from the INF model for predicting both the entire landslide area (BODY) and deposit areas (INF). Therefore, it would be the most recommended model for predicting these areas. In the case of predicting the landslide initiation areas (SUP), the BODY model, with a mean of 0.716, is the one that has the best predictive ability. Additionally, we observe that the SUP model has the lowest overall AUC values, as well as higher standard deviations compared to the other models.

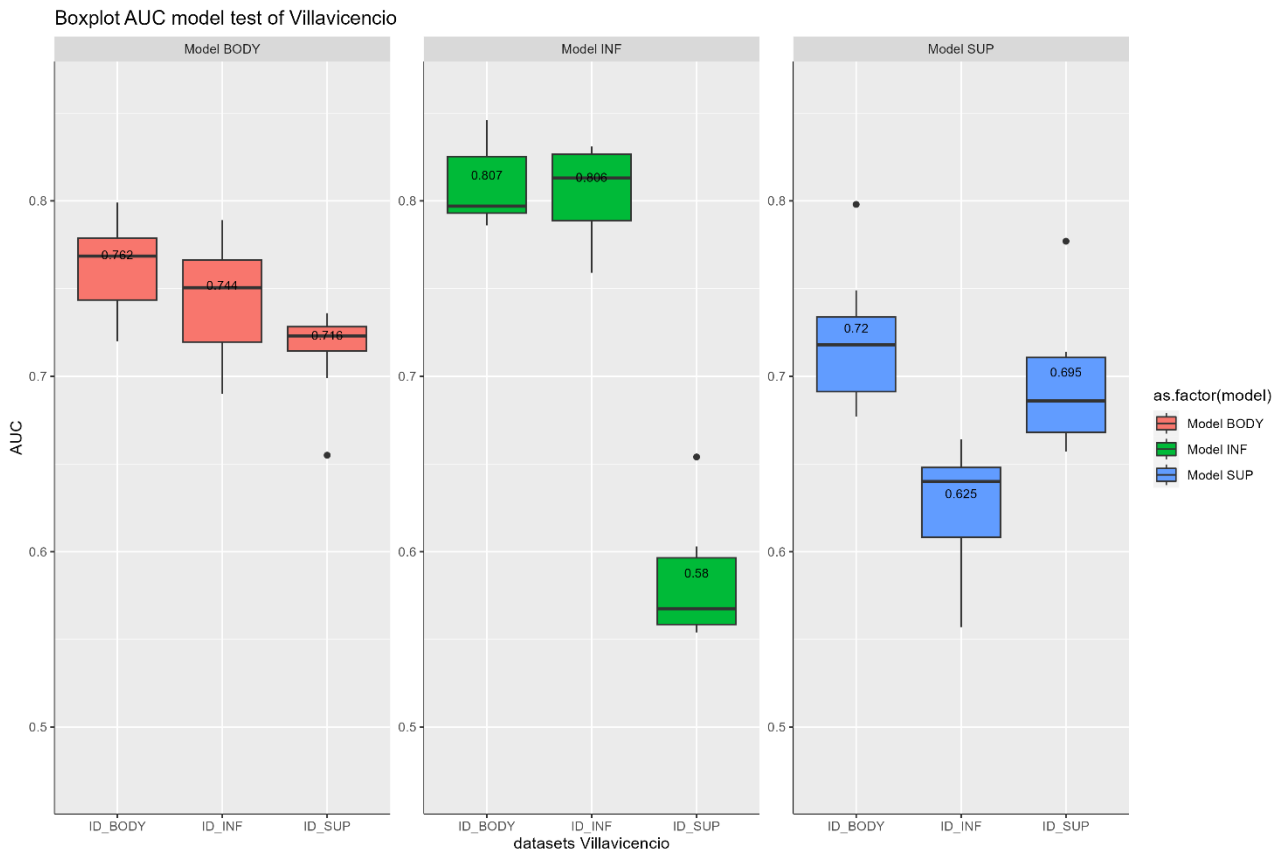


Fig. 71. Boxplot of the AUC for each model applied to the BODY, INF, and SUP test datasets of Villavicencio.

Table 19. Mean and standard deviation (SD) of the AUC from 10 repetitions of each model applied to every database in Villavicencio.

Dataset		AUC_Test_database Villavicencio			AUC_Train_database Villavicencio		
		BODY	INF	SUP	BODY	INF	SUP
Model BODY	Mean	0.762	0.744	0.716	0.818	0.748	0.702
	SD	0.025	0.031	0.024	0.013	0.015	0.025
Model INF	Mean	0.807	0.806	0.580	0.820	0.885	0.602
	SD	0.021	0.025	0.032	0.013	0.008	0.028
Model SUP	Mean	0.720	0.625	0.695	0.735	0.632	0.819
	SD	0.037	0.035	0.036	0.018	0.023	0.015

5.6. Landslide susceptibility maps

The following susceptibility maps represent the entire landslide area in each of the municipalities. This is because, according to the models obtained, predicting the entire landslide area (BODY) showed a better predictive value using the INF model.

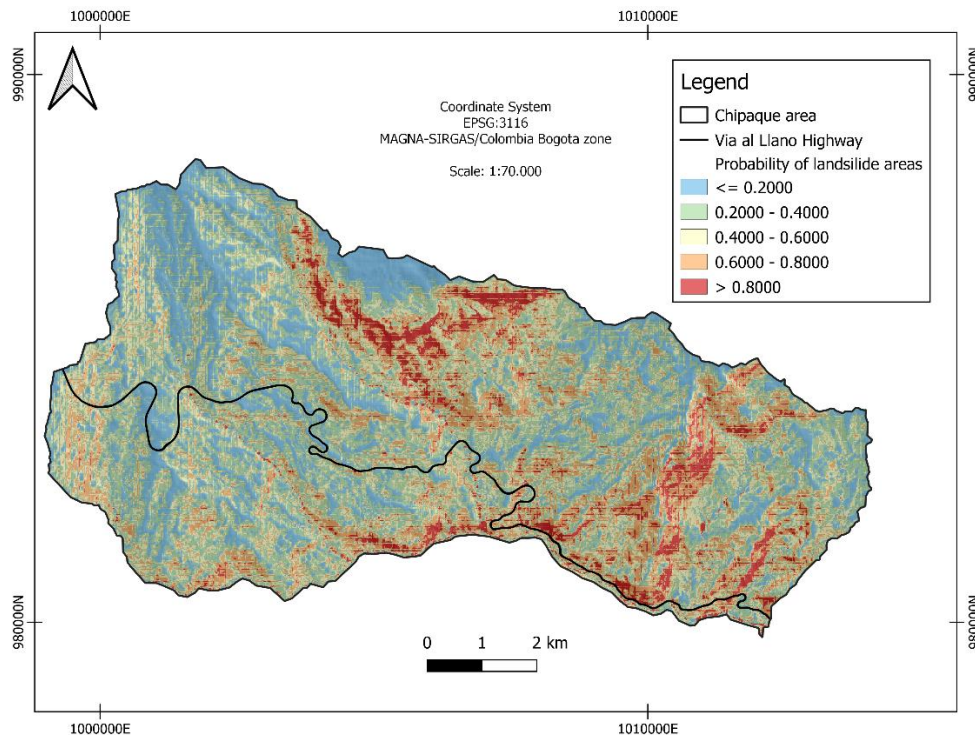


Fig. 72. Susceptibility map of landslides area in Chipaque municipality using the INF model.

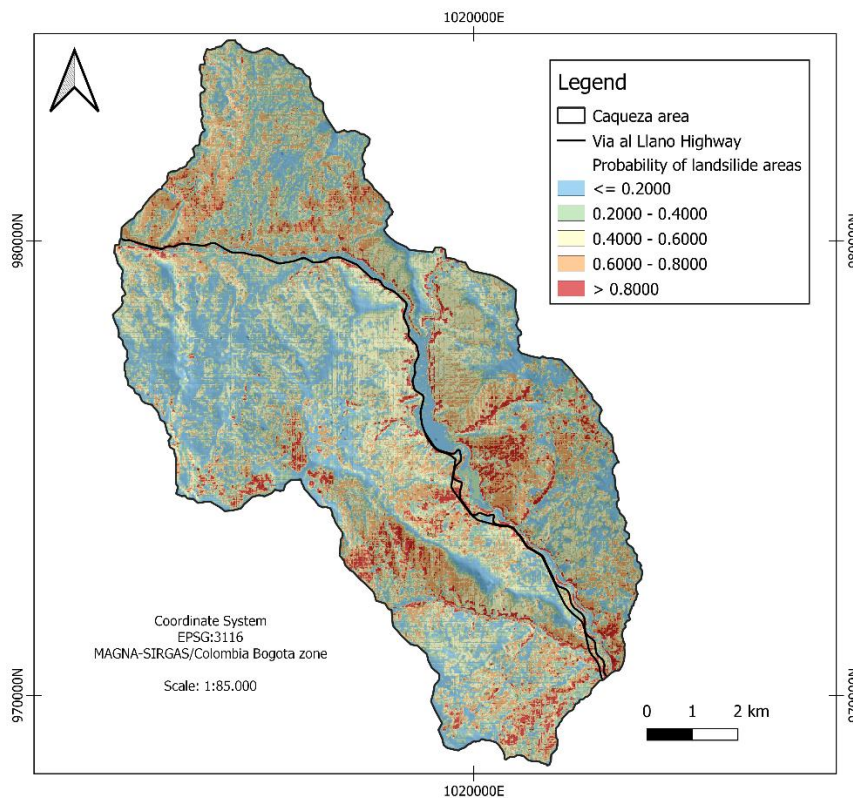


Fig. 73. Susceptibility map of landslides area in Caqueza municipality using the INF model.

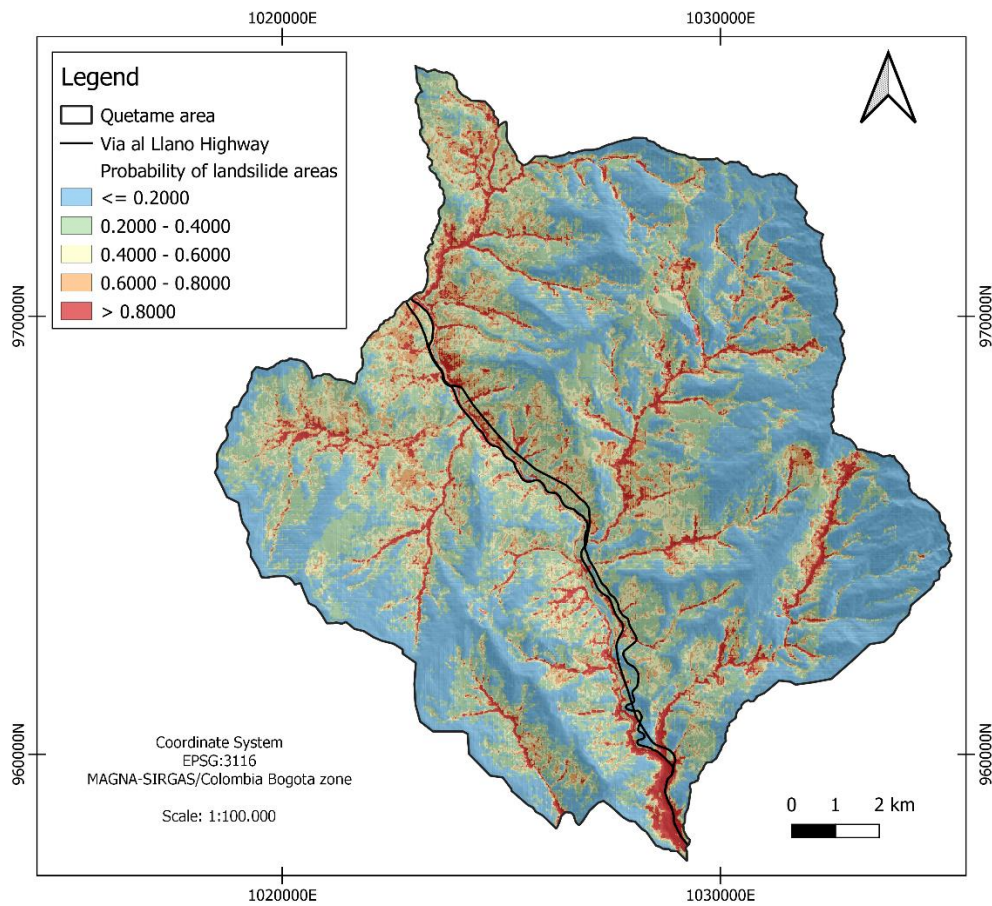


Fig. 74. Susceptibility map of landslides area in Quetame municipality using the INF model.

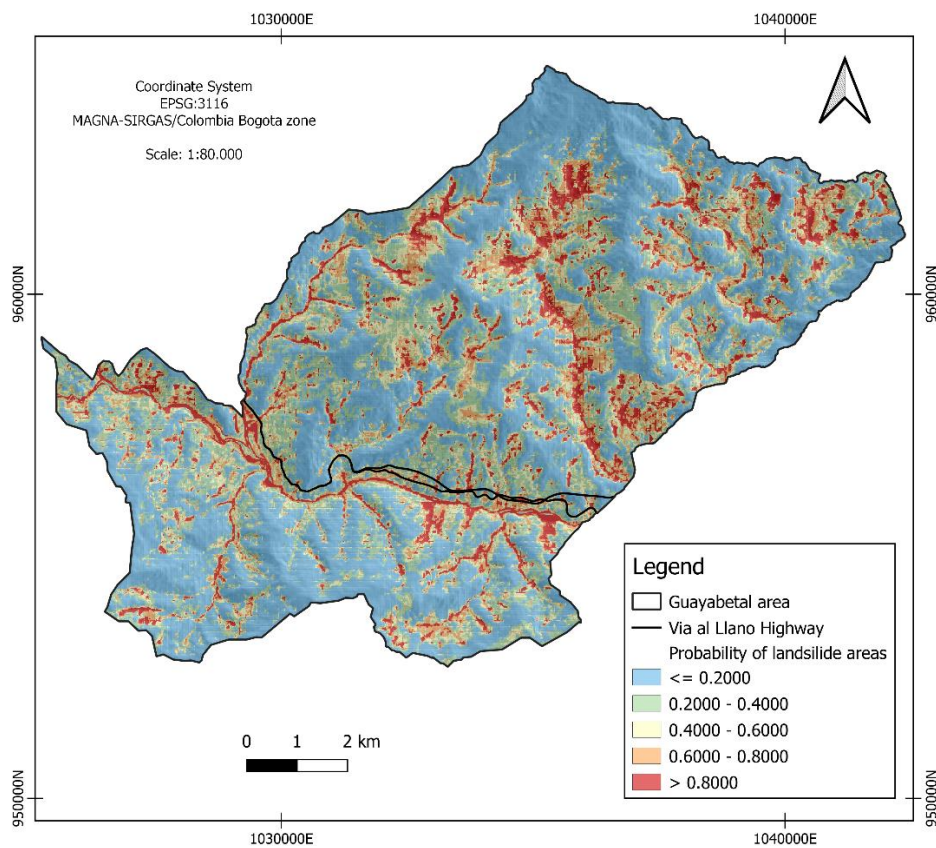


Fig. 75. Susceptibility map of landslides area in Guayabetal municipality using the INF model.

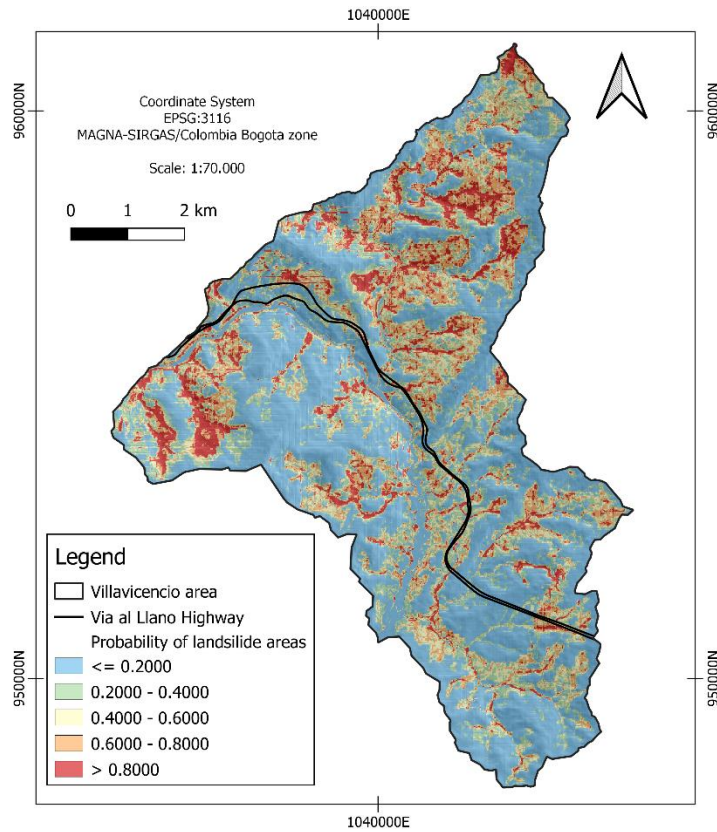


Fig. 76. Susceptibility map of landslides area in Villavicencio municipality using the INF model.

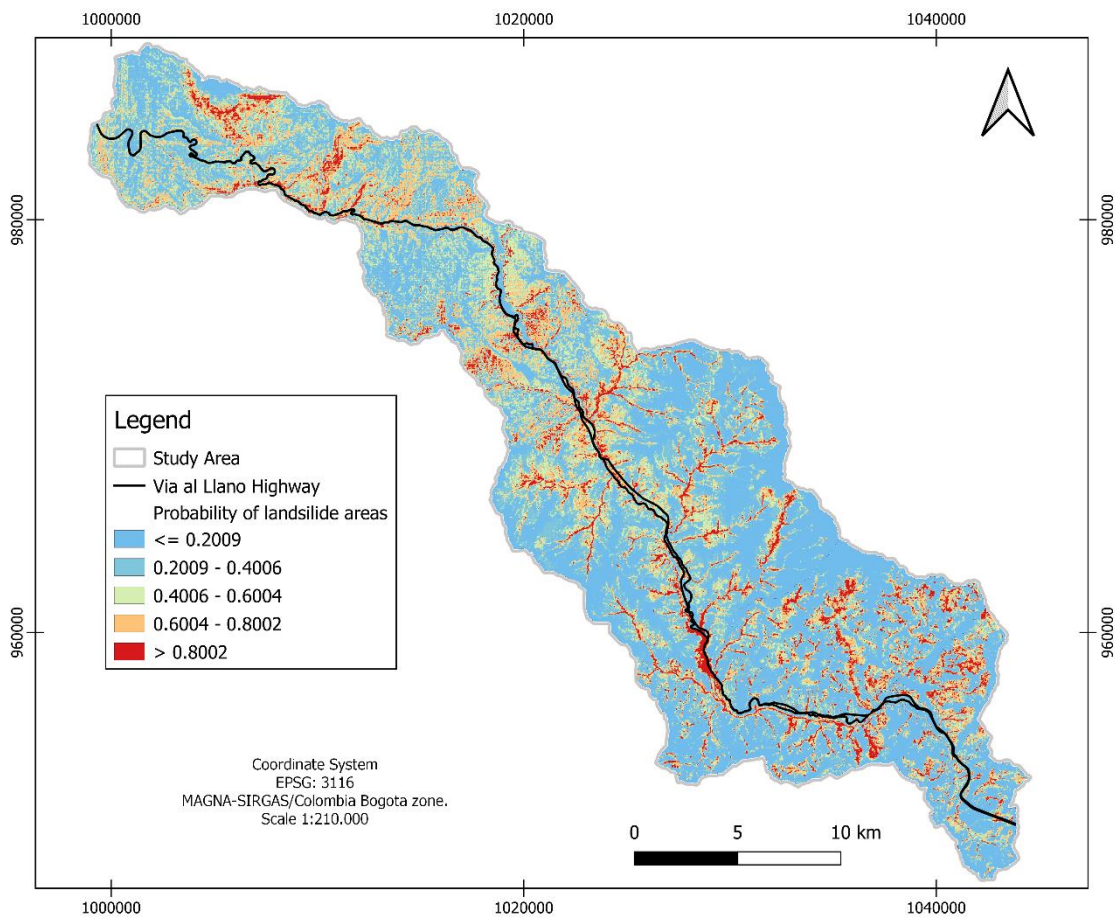


Fig. 77. Susceptibility map of landslides area in Via al Llano area using the INF model.

CHAPTER 6. DISCUSSION

6.1. Geomorphology Mapping

Comparing the geomorphological maps from both the Colombian Geological Survey (SGC) (Fig. 78A) and the one elaborated in this study (Fig. 78B), a clear difference in symbology is observed in terms of shape (polygons, lines, points) as well as color (specific to each type of morphogenesis), which can either facilitate or hinder their reading, interpretation, and analysis. Comparing the maps for the Chipaque area, the presence of lito-structural or structural morphogenetic processes (SGC) is evident. In the central part, we have indicated the presence of *cuestas* (Fig. 78B), while the SGC has indicated the entire area as a structural slope (Fig. 78A). However, in this is not possible to differentiate in which direction this slope is dipping, which is instead facilitated in the linear slope symbology with triangles and lines, as provided by the ISPRA et al. (2021) guide. On this same central area, we have indicated the presence of gravitational processes, which were not identified by the SGC. The gravitational processes indicated are soil creep (Fig. 44). However, in the "Cuaderno 13" guide from ISPRA et al. (2021), this type of movement is not included in the symbology, so the closest to this type of slow movement would be solifluction. Although according to the classification of Hungr, et al., (2014), solifluction is related to the slow movement of soil due to permafrost thawing. However, the study area is located in the tropics, near the equator and at an altitude of 2,500 to 3,000 m.a.s.l., which does not have permafrost. For this reason, it was preferred to indicate the area as a slow flow of Earth/mud, as present in the ISPRA et al. (2021) guide.

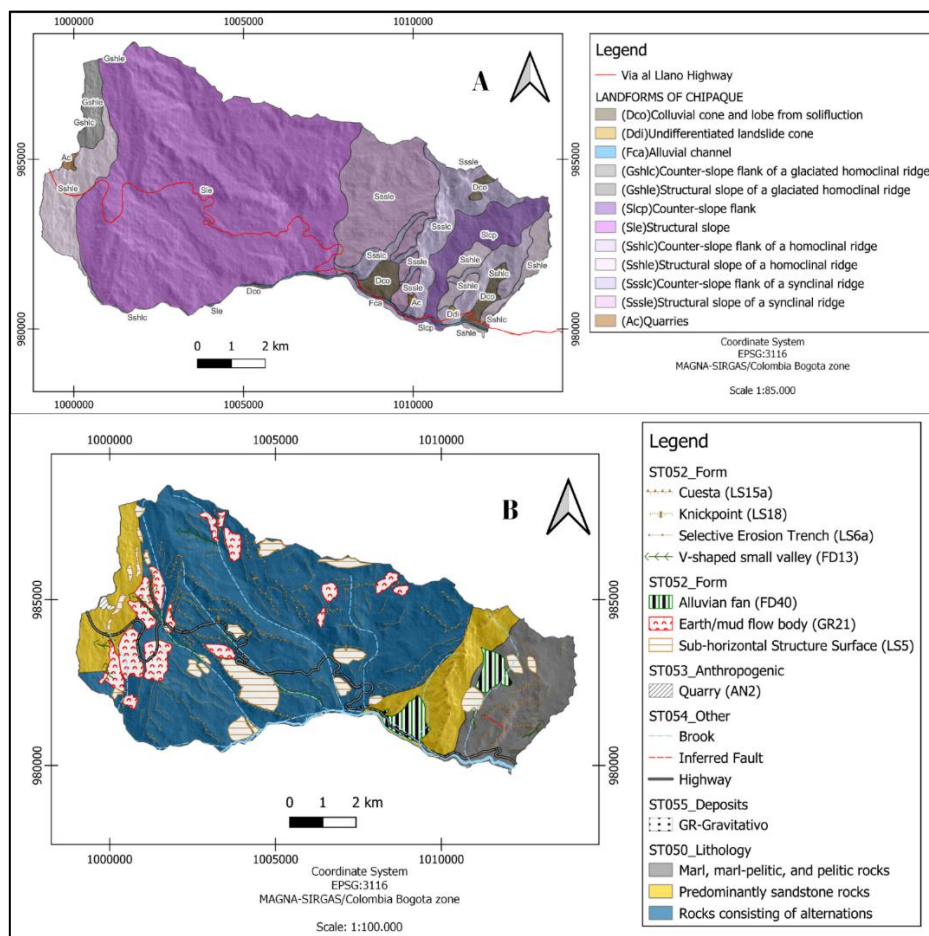


Fig. 78. Comparison of the geomorphological maps of Chipaque created by (A) Servicio Geológico Colombiano et al., (2012) and (B) based on guidance from "Cuaderno 13" of ISPRA et al., (2021).

In Caqueza, both maps agree on the presence of lito-structural, fluvial, and gravitational landforms. From this process, we have identified a scree slope (Fig. 79B) at south of the area. However, on the SGC map (Fig.79A), this has been indicated as a “Colluvial cone and lobe of solifluction”. The inclusion of the word "solifluction" in the nomenclature of the gravitational deposit shape specifically relates to the type of mass movement. Likewise, this nomenclature groups both cone and lobe deposit forms, which in the ISPRA et al., (2014) guide are classified separately. Therefore, the SGC nomenclature is quite general for this type of landform. On the other hand, within the lito-structural landforms that are also significant in this area, the presence of *cuesta* is observed, indicated by the SGC as counter-slope and structural-slope polygons, identified at south of the area. However, this is clear when there is a large aerial distance between them. Nevertheless, the large number of intercalated *cuesta* makes their polygonal delineation difficult, so it would be more advisable to identify them linearly. Another area that matches is the hogback area, which for the SGC encompasses the entire ridge, but for us, it mainly occurs at the end of it. Regarding fluvial landforms, the Floodplain area matches in both maps. However, the fluvial terraces that we recognized in this study were not identified by the SGC. Identify these potential terraces, especially where the urban area of Caqueza is located, is of vital importance for the management of the territorial planning of the area.

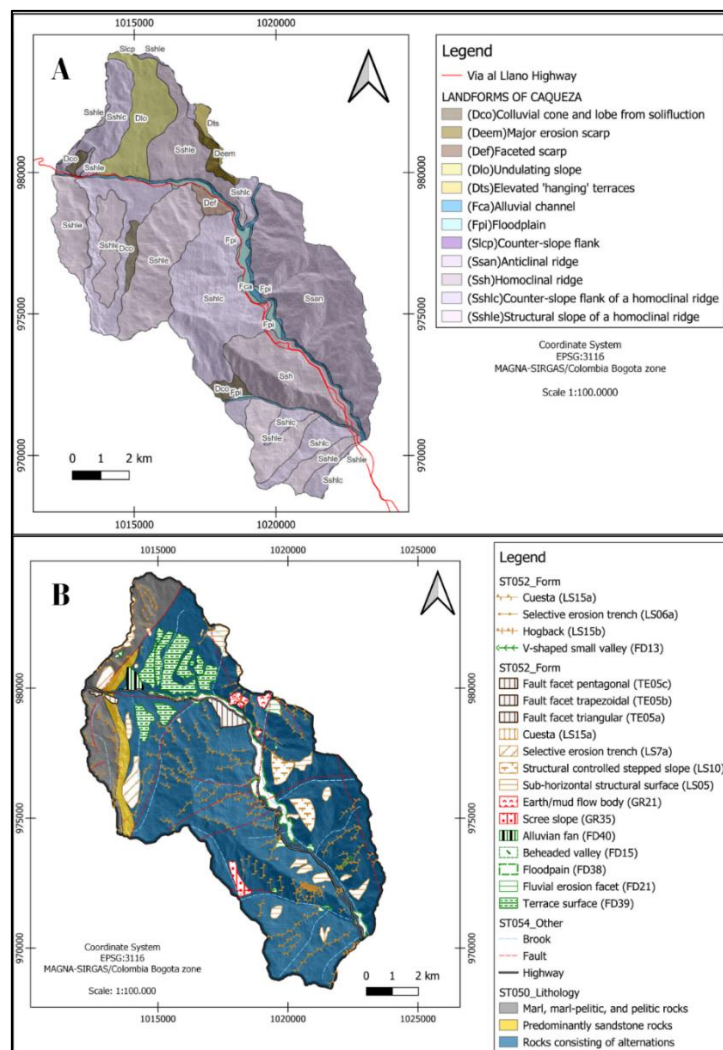


Fig. 79. Comparison of the geomorphological maps of Caqueza created by(A) Servicio Geológico Colombiano et al., (2012) and (B) based on guidance from “Cuaderno 13” of ISPRA et al., (2021).

In the Quetame area, the lithological change is not reflected in the geomorphological map of the SGC. Specifically in the central part, as a metamorphic body outcrop there. In this case, the same litho-structural symbology used within the sedimentary lithoid bodies is also used in the metamorphic one (Fig. 80A). The guide provided by ISPRA et al. (2014) allows for the differentiation ridges and trenches between lithology based, with 'a' representing the stratum, 'b' for the dike, and 'c' for different lithoid bodies. In this case, we utilized LS6c to represent these ridges in the Quetame Group area (Fig. 80B). On the southeastern side of the area, both maps agree on the presence of gravitational landforms. However, they are not classified as the same type of landform due to the difference between the guides. Conversely, some fluvial landforms do not match, as we have identified alluvial terraces in the center of the area, while according to the SGC map, the presence of terraces is located to the south of the area. Finally, we have identified a wide variety of gravitational landforms than litho-structural landforms. However, in the geomorphological map of SGC, there is a greater variety of litho-structural and fluvial landforms than gravitational ones.

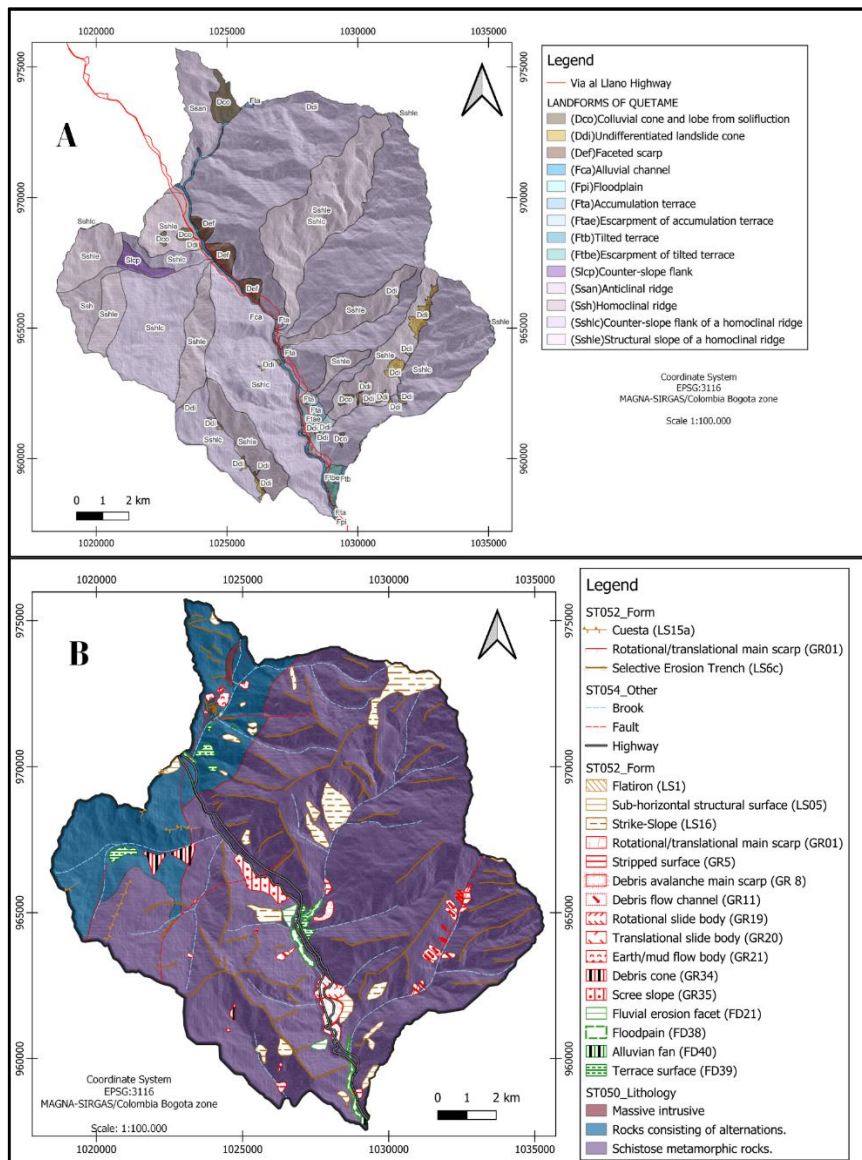


Fig. 80. Comparison of the geomorphological maps of Quetame created by (A) Servicio Geológico Colombiano et al., (2012) and (B) based on guidance from “Cuaderno 13” of ISPRA et al., (2021).

In the geomorphological map of Guayabetal by the SGC, we see more landforms classified as denudational, which are related with gravitational process. One of them is the "denuded ridge," which, according to the SGC guide, represents areas of long, concave, and convex slopes with high gradient, generally related to igneous and metamorphic lithologies (Table1) (Fig. 82A). However, this area within our analysis were identified ridges and trenches, but they are not overly pronounced (Fig. 80B). Additionally, in this same area, specifically where the highway passes through, we have identified two facets of fluvial erosion, which could also be fault facets. However, the limitation of verifying the landforms in the field does not allow us to be certain that they are fault facets. As for gravitational landforms, we have identified a wide variety on the northern side of the area, with significant dimensions, something that was not identified in the geomorphological map of SGC. This is possibly due to the difference in the dates of map creation. The geomorphological map of SGC was published in 2018, while the geomorphological maps presented here are published in 2023-2024, using satellite images from 2020 and 2021.

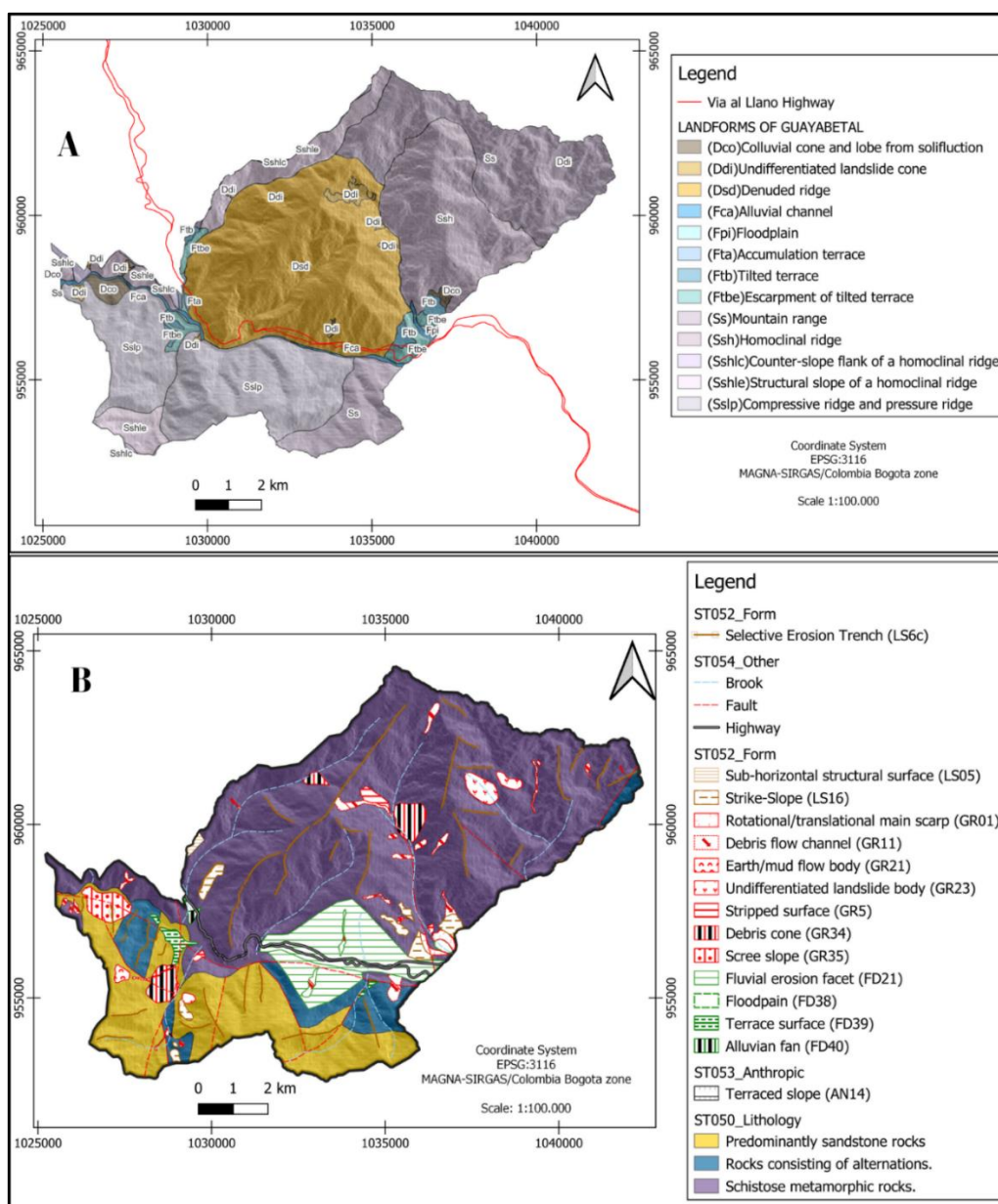


Fig. 81. Comparison of the geomorphological maps of Guayabetal created by (A) Servicio Geologico Colombiano et al., (2012) and (B) based on guidance from “Cuaderno 13” of ISPRA et al., (2021).

Finally, in the Villavicencio area, several landforms, both litho-structural and gravitational, match with those indicated on the SGC map. However, variations in the type of landform are observed, perhaps due to differences in nomenclature. In the geomorphological map presented, a greater number of gravitational landforms have been identified, possibly due to differences in the timing of their creation. Additionally, almost all fluvial landforms, such as terraces and floodplains, align between both maps (Fig. 82).

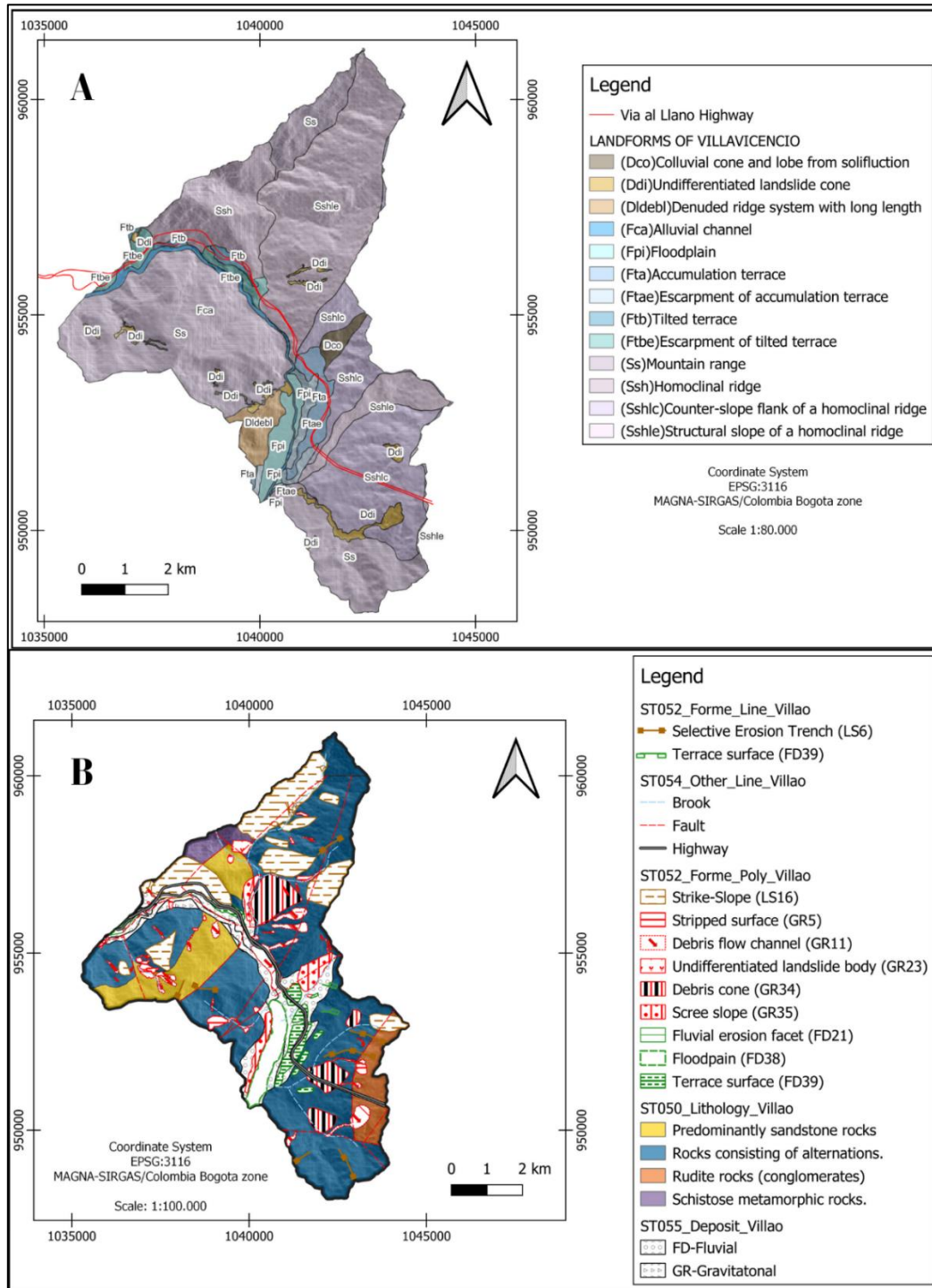


Fig. 82. Comparison of the geomorphological maps of Villavicencio created by (A) Servicio Geologico Colombiano et al., (2012) and (B) based on guidance from “Cuaderno 13” of ISPRA et al., (2021).

In general, when comparing the two methodologies used for geomorphological mapping, there are two clear differences. The methodology used by the Colombian Geological Service (SGC) limits the landforms to polygons, which means that linear and even point-like forms are not included. Similarly, the arrangement of colors without internal symbology makes it difficult to differentiate between different landforms of the same geomorphological process. On the other hand, the underlying lithology required by the "Cuaderno 13" guide is useful to correlate the landforms and morphogenesis, a detail that is lost in the SGC map. Additionally, the ISPRA et al. (2021) guide includes other information that could be important to show on the geomorphological maps, such as lithological forms (ST050), soil (ST051), anthropic forms (ST053), other symbols (ST055), and deposits (ST055), in addition to morphogenetic landforms (ST052), which further facilitates the visual relationship between them. Furthermore, each geomorphological map must specify the date of creation as certain landforms may be deformed, eliminated, or created over time.

On the other hand, the geomorphological maps created in this study were the result of visualizing high-resolution images and relief available from Google Earth. However, it is vital to confirm these landforms in field with the respective deposits associated. Furthermore, it is recommended to generate geomorphological maps at a scale of at least 1:50,000 to include more morphogenetic processes that are important for correlating with the Via al Llano Highway and the urban towns located around it.

6.2. Pluviosity

Two areas that have experienced frequent mass movements reported through public media are located at km 64 and km 58 along the Via al Llano Highway. In May 2017, debris material began to obstruct the highway due to a debris slide process in the km 64. Then, in mid-June 2017 and early July 2017, the sliding area expanded, once again obstructing the road. Then, this landslide was reactivated at the end of August and the beginning of September 2018, depositing debris material onto the road, as seen in Fig. 83. This movement has classified by its form as debris flow.

Later, in mid-April 2019, one of the most significant landslides recently recorded along the highway occurred at km 58. During that month, debris material occupied a section of the road as depicted in Fig. 84A. Then, in mid-May 2019, the debris slide became more evident, and the number of debris and rock material transported increased, completely covering the road (see Fig. 84B). In June, the debris slide extended laterally, forming a debris avalanche (see Fig. 84C), and in July, the landslide was reactivated, expanding both laterally and uphill (see Fig. 84D).

These two landslide sites are located, one to the south of the Quetame area (km 58) and the other in the center of the Guayabetal area (km 64). Coincidentally, two pluviometric stations, Monterredondo and Susumuco (Fig. 45), are situated in the vicinity of these two landslides.

To analyze the relationship between the previously mentioned landslides and rainfall, Table 20 summarizes the monthly precipitation from April to August, which are the rainiest months in the study area. This table includes the average monthly values over 15 years from both stations (Table 10), the average range of these values in the monthly mean maps created in this study (Fig. 54D to F, and 55A and B), as well as the monthly average values for the year 2017, associated with the initiation of the landslide event at km 64, and the monthly average values for the year 2019, associated with the initiation of the landslide at km 58.



Fig. 83. Debris flow at km 64. (Castañeda & Charrupí, 2018).



Fig. 84. Debris avalanche at km 58. **A.** May-2019 (Volando en Drone, 2019). **B.** June-2019 (Valora Analitik, 2019). **C.** July 2019 (Moreno, 2019). **D.** July 2019 (Blue radio, 2019).

Table 20. Monthly precipitation analysis from April to August in Monterredondo and Susumuco pluviometric stations.

	Monterredondo				Susumuco			
	Monthly average	Monthly map	2017	2019	Monthly average	Monthly map	2017	2019
April	252 mm	250-300 mm	190 mm	144 mm	490 mm	450-500 mm	395 mm	364 mm
May	368 mm	300-400 mm	478 mm	386 mm	697 mm	600-700 mm	1075 mm	623 mm
June	367 mm	300-400 mm	422 mm	523 mm	654 mm	600-700 mm	857 mm	795 mm
July	426 mm	400-500 mm	515 mm	570 mm	694 mm	600-700 mm	670 mm	1015 mm
August	381 mm	300-500 mm	272 mm	390 mm	585 mm	500-600 mm	575 mm	507 mm

When analyzing the year 2017 in the Table 20, it is noted that in April the value is below the average. However, in May, both in Monterredondo and Susumuco, precipitation significantly exceeds the average. Then, in the months of June and July, precipitation remains just a few units above their average, and in August, precipitation values decrease significantly. This indicates that the months of May, June, and July experienced precipitation above the average, coinciding with the beginning of the landslide at km 64 in May 2017, which continued to transport material constantly until July 2017. Additionally, it is observed that in August 2017, there were no reports of material transport for this landslide.

Analyzing the year 2019, we again observe that the month of April presents values below its monthly average. Then, in May, the monthly precipitation means are within the expected range. "However, in June and July of 2019, the amount of precipitation exceeded both the monthly average and the range generated on the maps, although it did not reach the level recorded in May 2017. Then, in August 2019, the monthly rainfall returned to within the expected range.

In the case of the landslide at km 58, it began moving in mid-April, a period when rainfall had not yet reached its monthly average. It is possible that some precipitation event occurred within 24 hours, greater than expected, but due to the lack of data, we cannot be certain. Subsequently, this area increased its material transport with the arrival of the rainiest months of the year, which in 2019 surpassed their monthly averages (June and July).

Therefore, we can conclude that in this case, where we have information on both the development of the landslide and the monthly data precipitation, we can establish a direct approximate relationship between the initiation of these events and the increase in rainfall during the months of May to July, occurring in the years 2017 and 2019. However, to obtain precise data on the average precipitation that can trigger landslides in an area, it is necessary to have data on intensity, duration, and frequency of precipitation events, along with the date of initiation of the landslides. This implies the presence of more pluviometric stations within the study area, as well as a monitoring network of mass movements in the area.

6.3. Automatic landslide inventory

Reviewing the results from Table 12, which display the metrics of the confusion matrices of the automatic inventory generated with GEE, it is evident that the images have a good capability to identify areas where there is no landslide, as indicated by the excellent values of specificity and accuracy. However, the objective is to assess the capability to identify landslide areas, and the presence of these non-landslide pixels may underestimate the results.

Therefore, we conducted an analysis exclusively comparing the polygons of landslides identified visually with the polygons obtained from vegetation changes, generated in GEE using SAR and NDVI data (see Table 21). Firstly, it is observed that the number of polygons generated with SAR and NDVI is relatively similar, but significantly higher than those identified visually. This may be due to the automatic identification of individual pixels showing vegetation changes, but not directly related to landslides. These polygons could represent anthropogenic interventions or other kinds of natural changes, such as mining, construction, deforestation, agriculture, flooding, and changes in reservoir water levels (Handwerger et al., 2022, and Scheip et al., 2021).

Table 21. Intersection polygons between the inventory created by SAR, NDVI, and Visual (expert).

	CHIPAQUE	CAQUEZA	QUETAME	GUAYABETAL	VILLAVICENCIO
Number of SAR polygons	2818	585	2950	1076	307
Number of NDVI polygons	2419	2677	2039	1004	491
Number of visual polygons	196	652	1076	267	172
Number of polygons intersected by SAR and NDVI	415	137	405	150	56
Number of polygons intersected by SAR and NDVI with visual	1	4	114	63	27
Number of polygons intersected by SAR and visual	7	7	231	127	88
Number of polygons intersected by NDVI and visual	31	70	449	188	147
Percentage of polygons intersected by SAR out of the total SAR polygons.	25%	1%	8%	12%	29%
Percentage of polygons intersected by NDVI out of the total NDVI polygons.	1%	3%	22%	19%	30%
Percentage of polygons intersected by SAR and NDVI with visual out of the total SAR and NDVI polygons.	0%	3%	28%	42%	48%

When analyzing the percentage of polygons identified by SAR as potential landslides, only 30% of the generated polygons were confirmed to be landslides, particularly in Villavicencio and 25% in Chipaque, as well as less than 15% in Guayabetal, Quetame, and Caqueza. Regarding NDVI, 30% of the generated polygons corresponded to landslide areas, specifically in Villavicencio, and 22% in Quetame. However, less than 20% of the polygons were identified as landslides in Guayabetal, Caqueza, and Chipaque.

Therefore, the results cannot suggest that either the NDVI or SAR method was superior to the other, given their similar outcomes. Nevertheless, the potential combination of SAR and NDVI data can help confirm whether there was indeed a vegetation change in a specific location, as this change could be evidenced in both types of images. This intersection reproduces a

relatively low number of polygons compared to the visually identified ones (Table 21). The results demonstrate that almost half of these polygons represent landslides, reaching up to 48% in Villavicencio and 42% in Guayabetal. Therefore, the combination of information obtained from SAR and NDVI significantly enhances the development of the automatic inventory.

An important consideration is the type of inventory. As mentioned in the study, the inventory for the Vía al Llano is historical or multitemporal, as the detachment date for almost 99% of the landslides in the area is unknown. Therefore, an exact date of landslides triggered cannot be defined. This means that when identifying them in the images, it is assumed they occurred after a certain period, which we have defined as the year prior to the image date. However, several of these landslides may have occurred in the pre-event period. As a result, when differentiating between rNDVI and SAR, these landslides are not identified as different, and therefore do not match the visually generated inventory through the images.

The articles that utilized rdNDVI and SAR for landslide identification did not evaluate their performance using confusion matrices. For areas identified as landslides based on SAR images, landslide density heatmaps were generated and assessed using ROC curves to determine if the landslide density identified by SAR corresponded with landslides identified after the events. This analysis demonstrated that the level of agreement exceeded 70% in regions with a high concentration of landslides (Handwerger et al., 2022). These findings were significant as they helped identify the most vulnerable areas within a region within hours or days of the event, enabling swift intervention.

In contrast, authors who utilized relative differences in NDVI (rdNDVI) for landslide identification did not provide a quantitative evaluation of the results obtained. This was because the outcomes were visually evident for landslide areas as well as other regions affected by wildfires, pyroclastic flows, and lava inundation (Scheip et al., 2021). Their primary objective was to establish a platform for promptly identifying certain natural phenomena without requiring high-performance devices, remote sensing knowledge, or coding skills, leveraging the capabilities of GEE.

6.4. Variable importance analysis and comparative model results

As mentioned in the results, the INF model demonstrated the best performance in identifying landslide-prone areas across the study municipalities. Considering the high-performance INF model for Quetame to identify potential landslide-susceptible locations, the optimal combination of variables includes Topographic Position Index (TPI), NDVI, elevation (ELE), precipitation (PLV), and lithology (LTL). This same relationship is replicated in Guayabetal, with a similarity in variable importance, but substituting PLV for slope (SLO).

Although there is a greater variation in precipitation (PLV) levels towards the southern part of the study area, this variable did not prove to be a significant differentiator for landslides in the INF model within the Villavicencio area. However, the PLV variable was found to be significant for Chipaque and Quetame, which are in the northern and central parts of the area.

In the case of the lithology variable, it was indispensable for Quetame and Guayabetal, but not for the regions of Chipaque, Caqueza, and Villavicencio. This variable may have contributed to better performance in Quetame and Guayabetal with values of 83% and 82%, respectively, as

landslide presence is significant in the Quetame group, which represents a metamorphic lithology.

Generally, the most important variables for landslide detachment areas (SUP databases) are slope (SLO), elevation (ELE), and curvature, as demonstrated by studies conducted by Rotigliano et al. (2019), Mercurio et al. (2022), and Martinello et al. (2022). In the SUP models, the slope (SLO) variable proved more influential than elevation (ELE). However, in Guayabetal, these two variables, along with NDVI, were identified as the most crucial, resulting in the highest model reliability value (0.747 AUC) among the evaluated municipalities for predicting landslide initiation areas (SUP).

On the other hand, the most representative variables for determining deposition areas are generally LS Factor (LSF), Topographic Position Index (TPI), as well as Topographic Wetness Index (TWI) and Stream Power Index (SPI), as demonstrated in the results of Vorpahl et al. (2012). These variables proved to be significant throughout the INF model analysis, with LSF, TPI, and TWI standing out.

Finally, it was evident that the curvature variable, including both profile curvature (PRC) and plan curvature (PCV), was not significant in the development of the BODY, INF, and SUP models.

In Herrera-Coy et al. (2023) study, the most important variables for the overall area were elevation (ELE), lithology (LTL), and land cover. However, notable variables also included Topographic Position Index (TPI), aspect (ASP), Topographic Roughness Index (TRI), Normalized Difference Vegetation Index (NDVI), as well as distance to rivers and distance to roads. Their models achieved a prediction probability of 0.87 and 0.83 for shallow and deep movements, respectively, using the random forest method. In our study, the three important variables for Herrera-Coy et al. (2023) did not have the same importance, but this did not result in a decrease in prediction accuracy.

In Calderón-Guevara et al. (2022) study, the variables included for develop the models were distance to faults (DF), elevation (EL), flow accumulation (FA), land cover (LC), and profile curvature (PRC). In comparison with the variables used in our study, only elevation (EL) would be coincident. With these variables, a prediction of 93.7% was achieved in the area using both random forest and artificial neural network methods.

Comparing the results of this study with those obtained in the same area by Herrera-Coy et al. (2023) and Calderón-Guevara et al. (2022) reveals some differences. In Fig. 85C, the area of high susceptibility is mainly limited to the central area where Quetame and Guayabetal are located, covering not only landslide-prone areas but also regions that may not be equally susceptible, as evidenced by Fig. 85A and Fig. 85B. In our models, we observe that the highest probability of landslides occurs amid the tributary streams of the Rio Negro, as indicated by the red color representing high susceptibility areas overlapping with drainage areas. Similar patterns are also observed in the maps of Herrera-Coy et al. (2023), both for shallow and deeper landslides. However, Herrera-Coy et al. (2023) maps encompass more susceptible areas both in the southern and northern parts of the area. In our case, susceptibility in the southern part is highly concentrated within the drainage, whereas in the northern part, it tends to be found in sections away from the drainage. Nonetheless, our models clearly distinguish areas that are truly not susceptible. However, in the maps by Calderón-Guevara et al. (2022), the southern and northern areas are generally not susceptible to landslide.

The maps in Fig. 85B and Fig. 85C fail to show their relationship with the road network. However, the map in Fig. 85A does consider this relationship, although it is difficult to precisely define the most susceptible areas along the road, due their scale. Therefore, municipality-based maps allow for increased resolution, enabling a better understanding of susceptibility in relation to the road network, as evidenced in Fig. 72 to Fig. 76.

In the Chipaque area, the southern region where the road crosses the Une Formation and the alluvial fan, has a high probability of landslides. In the case of Caqueza, susceptibility is significantly higher in the central part where some *cuesta* converge and there is a presence of structurally controlled stepped slopes. Conversely, in Quetame, the most susceptible areas near the road are in the southern and northern parts, close to the floodplains. Both in Quetame and Guayabetal, there are drainage areas intersecting the road, which are the most susceptible points in both areas. In Villavicencio, susceptibility over the road decreases, although there are some intersections with susceptible areas, but with a lower tonality of less than 80%.

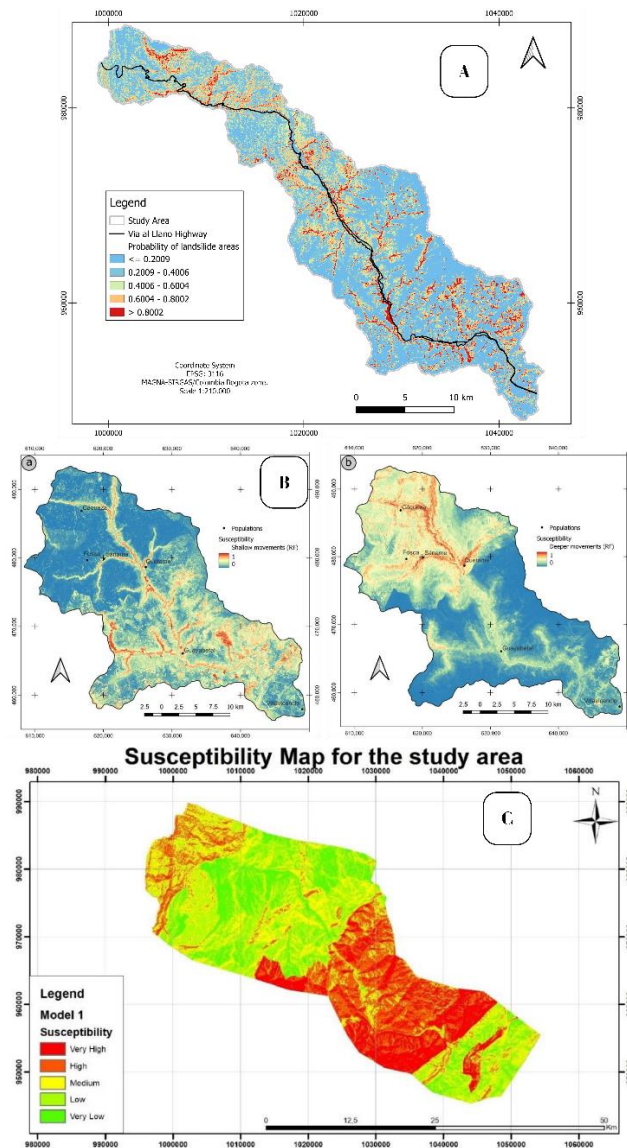


Fig. 85. Landslide susceptibility maps of the Via al Llano area. **A.** Map from the present study. **B.** Shallow movement susceptibility map (a) and deep movement susceptibility map (b) from Herrera-Coy et al. (2023). **C.** Landslide susceptibility map from Calderón-Guevara et al. (2022).

CHAPTER 7. CONCLUSIONS

The methodology of geomorphological mapping from Colombian Geological Service (SGC) limits landforms to polygons, excluding linear and point-like forms. Additionally, the absence of internal symbology in color coding complicates differentiation between different landforms of the same geomorphological process. Furthermore, the lack of additional features like lithology or anthropic processes hinders map understanding. However, the "Cuaderno 13" guide has addressed these issues through ongoing development and updates.

Improvements in geomorphological mapping using "Cuaderno 13" guide from ISPRA allow for correlating these maps with landslide susceptibility. However, generating maps at a scale of at least 1:50,000 is advised to capture significant morphogenetic processes impacting hazard and risk assessment along the Via al Llano area.

The correlation of morphogenetic processes in the area, as determined through the creation of geomorphological maps, aided in recognizing their association with the occurrence of landslides in particular areas. For instance, the km64 landslide, situated between two river facets, facilitates gravitational processes owing to its morphogenesis and slope.

In cases where we have information on both landslide development and monthly precipitation data, we could establish a direct relationship between the initiation of these events and increased rainfall during May to July in 2017 and 2019. However, precise data on average precipitation triggering landslides requires information on intensity, duration, frequency of precipitation events, and landslide initiation dates. This highlights the need for more pluviometric stations and a mass movement monitoring network within the study area.

The automated identification of vegetation change areas using SAR and NDVI data in GEE to correlate with landslide occurrence revealed a significant number of false positives, with a maximum of 30% of these areas correctly classified. These inaccuracies may arise from various anthropogenic or natural factors. However, by combining SAR and NDVI results, the number of false positives decreases, resulting in nearly half of the common areas identified representing actual landslide occurrences in our study.

An important aspect to consider in the results of the automatic inventory process is the nature of the study area, which involves a multitemporal inventory. This implies that some of the identified landslides may not correspond to the time of occurrence, leading to the presence of false positives. However, implementing this methodology for seasonal inventories holds the potential to yield more accurate results.

The INF model outperformed the BODY and SUP models in identifying landslide-prone areas across the study municipalities, achieving AUC values of 0.74 in Chipaque, 0.75 in Caqueza, 0.83 in Quetame, 0.82 in Guayabetal, and 0.81 in Villavicencio. This superior performance can be attributed to its optimal combination of key variables, including Topographic Position Index (TPI), Normalized Difference Vegetation Index (NDVI), elevation (ELE), precipitation (PLV), slope (SLO) and lithology (LTL).

Although two susceptibility studies have been conducted in the area with capable prediction results from the models, the important variables in these studies are not of the same significance as those emphasized by the MARS model in our study.

In our models, we have noted that landslides are most probable around the tributary streams of the Rio Negro, matching findings from Herrera-Coy et al. (2023). However, discrepancies emerge with the map of Calderón-Guevara et al. (2022), where southern and northern areas show lower susceptibility, contrary to our findings.

While the susceptibility maps from the two previous studies in the area do not clearly depict the relationship with the road network, our study aimed to address this aspect. However, limitations due to scale were encountered in our attempts. Therefore, municipality-based maps offer enhanced resolution, allowing for a better understanding of susceptibility concerning the road network.

In summary, this area stands out as a unique "natural laboratory" located in Colombia. Within just 80 kilometers, there is a remarkable variation in thermal floors, ranging from 400 to over 2300 meters, accompanied by contrasting climatic conditions. The region features all types of rocks of varying ages and highly abrupt morphologies. This exceptional combination of factors makes it an invaluable site for scientific study and observation.

REFERENCES

- Alvioli, M., Marchesini, I., Reichenbach, P., Rossi, M., Ardizzone, F., Fiorucci, F., & Guzzetti, F. (2016). Automatic delineation of geomorphological slope units with r.slopeunits v1.0 and their optimization for landslide susceptibility modeling. *Geoscientific Model Development*, 9(11), 3975–3991.
<https://doi.org/10.5194/gmd-9-3975-2016>
- Aukema, Y. J., Wilson, S., & Irwin, D. (2019). THE SAR HANDBOOK Comprehensive Methodologies for Forest Monitoring and Biomass Estimation (SERVIR Global).
<https://doi.org/10.25966/nr2c-s697>
- Beguiría, S. (2006). Validation and evaluation of predictive models in hazard assessment and risk management. *Natural Hazards*, 37(3), 315–329.
<https://doi.org/10.1007/s11069-005-5182-6>
- Blue radio (2019, 23 July) Desde 2013 notificamos de los problemas en el km 58 de la vía al Llano: Coviandes.
<https://www.bluradio.com/nacion/desde-2013-notificamos-de-los-problemas-en-el-km-58-de-la-via-al-llano-coviandes>
- Bock, M., & Köthe, R. (2008). Predicting the depth of hydromorphic soil characteristics influenced by ground water. *SAGA—Seconds Out*, 19, 13–22.
<https://www.researchgate.net/publication/267553405>
- Bock, M., Böhner, J., Conrad, O., Köthe, R., & Ringeler, A. (2007). XV. Methods for creating functional soil databases and applying digital soil mapping with SAGA GIS. JRC Scientific and Technical Reports.
- Booth, G., Niccolucci, M., & Schuster EG. (1994). Identifying proxy sets in multiple linear regression: an aid to better coefficient interpretation. Research Paper INT (USA).
<https://agris.fao.org/agris-search/search.do?recordID=US9439776>
- Brenning, A. (2005). Spatial prediction models for landslide hazards: review, comparison and evaluation. In *Natural Hazards and Earth System Sciences* (Vol. 5).
- Calderón Guevara, W. A. (2020). Assessment of susceptibility to landslides in the eastern cordillera of Colombia using the weight of evidence statistical method. [Tesis, Universidad de los Andes]. Repositorio Uniandes.
- Calderón-Guevara, W., Sánchez-Silva, M., Nitescu, B., & Villarraga, D. F. (2022). Comparative review of data-driven landslide susceptibility models: case study in the Eastern Andes mountain range of Colombia. *Natural Hazards*, 113(2), 1105–1132.
- Camilo, D. C., Lombardo, L., Mai, P. M., Dou, J., & Huser, R. (2017). Handling high predictor dimensionality in slope-unit-based landslide susceptibility models through LASSO-penalized Generalized Linear Model. *Environmental Modelling and Software*, 97, 145–156.
<https://doi.org/10.1016/j.envsoft.2017.08.003>
- Carrara, A., Guzzetti, F., Cardinali, M., & Reichenbach, P. (1999). Use of GIS Technology in the Prediction and Monitoring of Landslide Hazard. In *Natural Hazards* (Vol. 20).
- Castañeda, P. & Charrupí L.F. (2018, 26 september). La Vía al Llano: el incurable dolor de cabeza del Meta. *Semana*.
<https://www.semana.com/via-al-llano-cierre-de-la-carretera-bogota-villavicencio/641/>
- Chaparro-Cordón, J. L., Rodríguez-Castiblanco, E. A., Rangel-Flórez, M. S., García-Delgado, H., & Medina-Bello, E. (2020). Statistical description of some landslide inventories from Colombian Andes: study cases in Mocoa, Villavicencio, Popayán, and Cajamarca, SCG-XIII International

- Symposium on Landslides 2020, Cartagena, Colombia, 15–19 June 2020.
- Chow, V.T., Maidment, D.R., Mays, L.W. (1971). *Applied hydrology*. McGraw-Hill International Editions, Civil Engineering Series.
- Chung, C.-J. F., & Fabbri, A. G. (2003). Validation of Spatial Prediction Models for Landslide Hazard Mapping. In *Natural Hazards* (Vol. 30).
- Ciccacci, S. (2010). *Le forme del rilievo. Atlante illustrato di geomorfologia*. Mondadori Università-Sapienza Università di Roma.
- Cohen, J., 1960. A coefficient of agreement for nominal scales. *Educ. Psychol. Meas.* 20(1), 37–46.
- Conoscenti, C., Ciaccio, M., Caraballo-Arias, N. A., Gómez-Gutiérrez, Á., Rotigliano, E., & Agnesi, V. (2015). Assessment of susceptibility to earth-flow landslide using logistic regression and multivariate adaptive regression splines: A case of the Belice River basin (western Sicily, Italy). *Geomorphology*, 242, 49–64. <https://doi.org/10.1016/j.geomorph.2014.09.020>
- Corominas J, van Westen, C, Frattini P, et al. (2014). Recommendations for the quantitative analysis of landslide risk. *Bull Eng Geol Environ* 73(2): 209-263. <https://doi.org/10.1007/s10064-013-0538-8>
- Cruden, D. M., & Varnes, D. J. (1996). *Landslide Types and Processes*. In Transportation Research Board, U.S. National Academy of Sciences, Special Report (Vol. 247). <https://www.researchgate.net/publication/269710331>
- Czaplewski, R.L., 1994. Variance Approximations for Assessments of Classification Accuracy. Res. Pap. RM-316. U.S. Department of Agriculture, Forest Service, Rocky Mountain Forest and Range Experiment Station, Fort Collins, CO (29 pp.).
- Desmet, P. J. J., & Govers, G. (1996). A GIS procedure for automatically calculating the USLE LS factor on topographically complex landscape units. *Journal of Soil and Water Conservation*, 51(5), 427-433. <https://www.jswconline.org/content/51/5/427.short>
- Díaz, J. M. (2002). *Zonificación de la amenaza por fenómenos de remoción en masa en la vía Bogotá - Villavicencio, tramo Túnel del Boquerón - Chipaque*. Trabajo Final. Universidad nacional de Colombia. Bogotá
- Dikau, R. (1988). Entwurf einer geomorphologisch-analytischen Systematik von Reliefeinheiten. *Heidelberger Geographische Bausteine*, 5, 45.
- Dormann, C. F., Elith, J., Bacher, S., Buchmann, C., Carl, G., Carré, G., Marquéz, J. R. G., Gruber, B., Lafourcade, B., Leitão, P. J., Münkemüller, T., McClean, C., Osborne, P. E., Reineking, B., Schröder, B., Skidmore, A. K., Zurell, D., & Lautenbach, S. (2013). Collinearity: a review of methods to deal with it and a simulation study evaluating their performance. *Ecography*, 36(1), 27–46. <https://doi.org/10.1111/J.1600-0587.2012.07348.X>
- Fiorucci, F., Cardinali, M., Carlà, R., Rossi, M., Mondini, A. C., Santurri, L., Ardizzone, F., & Guzzetti, F. (2011). Seasonal landslide mapping and estimation of landslide mobilization rates using aerial and satellite images. *Geomorphology*, 129(1–2), 59–70. <https://doi.org/10.1016/j.geomorph.2011.01.013>
- Fleiss, J.L., Levin, B., Paik, M.C., 2013. *Statistical Methods for Rates and Proportions*, Third edition. John Wiley & Sons.
- Foody, G. M. (2020). Explaining the unsuitability of the kappa coefficient in the assessment and comparison of the accuracy of thematic maps obtained by image classification. *Remote sensing of environment*, 239, 111630.

- Friedman, J. H. (1991). Estimating Functions of Mixed Ordinal and Categorical Variables Using Adaptive Splines. <https://apps.dtic.mil/sti/citations/ADA590939>
- Google Earth Engine. (n.d.). Overview.
- Gruber, S., & Peckham, S. (2009). Chapter 7 Land-Surface Parameters and Objects in Hydrology. *Developments in Soil Science*, 33(C), 171–194. [https://doi.org/10.1016/S0166-2481\(08\)00007-X](https://doi.org/10.1016/S0166-2481(08)00007-X)
- Gu, Q., Zhu, L., Cai, Z., 2009. Evaluation measures of the classification performance of imbalanced data sets. In: *International Symposium on Intelligence Computation and Applications*. Springer, pp. 461–471.
- Guerrero, J. (2002). A proposal on the classification of System Tracts: Application to the Allostratigraphy and Sequence Stratigraphy of the Cretaceous Colombian Basin Part 1: Berrriasian to Hauterivian. *Geología Colombiana*, 27.
- Guzzetti, F. (2005). *Landslide Hazard and Risk Assessment [Rheinische Friedrich-Wilhelms-Universität]*. <https://bonndoc.ulb.uni-bonn.de/xmlui/handle/20.500.11811/2644>
- Guzzetti, F., Mondini, A. C., Cardinali, M., Fiorucci, F., Santangelo, M., & Chang, K. T. (2012). Landslide inventory maps: New tools for an old problem. *Earth-Science Reviews*, 112(1–2), 42–66. <https://doi.org/10.1016/j.earscirev.2012.02.001>
- Handwerger, A. L., Huang, M. H., Jones, S. Y., Amatya, P., Kerner, H. R., & Kirschbaum, D. B. (2022). Generating landslide density heatmaps for rapid detection using open-access satellite radar data in Google Earth Engine. *Natural Hazards and Earth System Sciences*, 22(3), 753–773. <https://doi.org/10.5194/nhess-22-753-2022>
- Handwerger, A. L., Huang, M.-H., Jones, S. Y., Amatya, P., Kerner, H. R., and Kirschbaum, D. B. (2022) Generating landslide density heatmaps for rapid detection using open-access satellite radar data in Google Earth Engine, *Nat. Hazards Earth Syst. Sci.*, 22, 753–773, <https://doi.org/10.5194/nhess-22-753-2022>
- Hartkamp, A. D., De Beurs, K., Stein, A., & White, J. W. (1999). Interpolation techniques for climate variables. *Cimmyt*.
- Hengl, T., & Reuter, H. I. (2008). *Geomorphometry: concepts, software, applications (Vol. 33)*. *Developments in Soil Science*.
- Hennemuth, B., Bender, S., Bülow, K., Dreier, N., Keup-Thiel, E., Krüger, O., ... & Schoetter, R. (2013, January). Statistical methods for the analysis of simulated and observed climate data: applied in projects and institutions dealing with climate change impact and adaptation. *CSC*.
- Herrera-Coy, M. C., Calderón, L. P., Herrera-Pérez, I. L., Bravo-López, E., Conoscenti, C., García, J. D., Sánchez-Gómez, M., & Fernández, T. (2023). Landslide susceptibility analysis on the vicinity of Bogotá-Villavicencio Road (Eastern Cordillera of the Colombian Andes). *Remote Sensing*, 15(15), 3870. <https://doi.org/10.3390/rs15153870>
- Hornberger, G.M., Wiberg, P.L., Raffensperger, J.P., D’Odorico, P. (2014). *Elements of Physical Hydrology*. Second Edition. Johns Hopkins University Press. Baltimore
- Hungr, O., Leroueil, S., & Picarelli, L. (2014). The Varnes classification of landslide types, an update. *Landslides*, 11(2), 167–194. <https://doi.org/10.1007/S10346-013-0436-Y/FIGURES/33>
- Hussin, H. Y., Zumpano, V., Reichenbach, P., Sterlacchini, S., Micu, M., van Westen, C., & Bălteanu, D. (2016). Different landslide sampling strategies in a grid-based bi-variate statistical susceptibility model. *Geomorphology*, 253, 508–523.

- <https://doi.org/10.1016/j.geomorph.2015.10.030>
- IDEAM (2017). Atlas Climatológico de Colombia. Bogota, D.C.
- INGEOMINAS & IDEAM (2010). “Mapa Nacional de Amenaza Relativa por Movimientos en Masa actualización”. Plancha 5-09 y Plancha 5-14. Escala 1:500.000.
- INGEOMINAS, Patiño, A., Fuquen, J., Ramos, J., Pedraza, A., Ceballos, L., Pinzón, L., Jerónimo, Y., Álvarez, L., Torres Bogotá, A., & De, M. (2011). Memoria Explicativa Cartografía Geológica De La Plancha 247 Cáqueza Escala: 1:100,000.
- INGEOMINAS, Pulido, O., & Gomez, L. S. (2001). Memoria Explicativa Cartografía Geológica De La Plancha 266 Cáqueza Escala: 1:100,000.
- INGEOMINAS. (1998). Mapa Geologico de la Plancha 266.
- INGEOMINAS. (2011). Mapa Geologico de la Plancha 247.
- ISPRA, AIGeo, CNG, Campobasso C., Carton A., Chelli A., D’Orefice M., Dramis F., Graciotti R., Guida D., Pambianchi G., Peduto F., & Pellegrini L. (2021). Quaderni Serie III. Aggiornamento ed Integrazioni delle Linee guida della Carta Geomorfologica d’Italia alla scala 1:50,000 e Banca Dati Geomorfologica (Vol. 13).
- Jacobs, L., Kervyn, M., Reichenbach, P., Rossi, M., Marchesini, I., Alvioli, M., & Dewitte, O. (2020). Regional susceptibility assessments with heterogeneous landslide information: Slope unit- vs. pixel-based approach. *Geomorphology*, 356. <https://doi.org/10.1016/j.geomorph.2020.107084>
- Köthe, R., Gehrt, E., & Böhner, J. (1996). Automatische Reliefanalyse für geowissenschaftliche Anwendungen- derzeitiger Stand und Weiterentwicklungen des Programms SARA. *Arbeitshefte Geologie*, 31–37.
- Landis, J.R., Koch, G.G., 1977. The measurement of observer agreement for categorical data. *Biometrics* 33, 159–174.
- Le Toan, T., Beaudoin, A., Riou, J., and Guyon, D.: Relating forest biomass to SAR data, *IEEE T. Geosci. Remote*, 30, 403–411, <https://doi.org/10.1109/36.134089>, 1992.
- Lima, P., Steger, S., & Glade, T. (2021). Counteracting flawed landslide data in statistically based landslide susceptibility modelling for very large areas: a national-scale assessment for Austria. *Landslides*, 18(11), 3531–3546. <https://doi.org/10.1007/s10346-021-01693-7>
- Magliulo, P., Di Lisio, A., Russo, F., & Zelano, A. (2008). Geomorphology and landslide susceptibility assessment using GIS and bivariate statistics: A case study in southern Italy. *Natural Hazards*, 47(3), 411–435. <https://doi.org/10.1007/s11069-008-9230-x>
- Martinello, C., Cappadonia, C., Conoscenti, C., & Rotigliano, E. (2022). Landform classification: a high-performing mapping unit partitioning tool for landslide susceptibility assessment—a test in the Imera River basin (northern Sicily, Italy). *Landslides*, 19(3), 539–553. <https://doi.org/10.1007/S10346-021-01781-8/FIGURES/10>
- Martinello, C., Cappadonia, C., Conoscenti, C., Agnesi, V., & Rotigliano, E. (2021). Optimal slope units partitioning in landslide susceptibility mapping. *Journal of Maps*, 17(3), 152–162. https://doi.org/10.1080/17445647.2020.1805807/SUPPL_FILE/TJOM_A_1805807_SM7352.PDF
- Mercurio, C. (2022). Landslides Susceptibility Stochastic Modelling Under Earthquakes and Rainfalls Triggering: Applications to 2001 Earthquakes (13th January and 13th February) and 2009 Tropical Storm (IDA

- /96E). Dissertation. Università degli Studi de Palermo.
- Milborrow, S. (2021). Notes on the earth package.
- Mondini, A. C., Guzzetti, F., Chang, K. T., Monserrat, O., Martha, T. R., & Manconi, A. (2021). Landslide failures detection and mapping using Synthetic Aperture Radar: Past, present and future. *Earth-Science Reviews*, 216, 103574. <https://doi.org/10.1016/j.earscirev.2021.103574>
- Monserud, R.A., Leemans, R., 1992. Comparing global vegetation maps with the kappa statistic. *Ecol. Model.* 62 (4), 275–293.
- Moreno, J. (2019, 18 July), Descartan construcción de túneles falsos en el km 58. *Periódico del Meta*. <https://periodicodelmeta.com/descartan-construccion-de-tuneles-falsos-en-el-km-58/>
- Navarro, S., Hernandez, A., García, J., Reyes, A., Ruiz, G., ... Mora, M. (2019). Contexto geológico, geomorfológico, susceptibilidad y amenaza por movimientos en masa km 58 vía Bogotá - Villavicencio. Bogotá: Servicio Geológico Colombiano; Dirección de Geoamenazas.
- Pembury Smith, M.Q.R., Ruxton, G.D. (2020). Effective use of the McNemar test. *Behav Ecol Sociobiol* 74, 133 <https://doi.org/10.1007/s00265-020-02916-y>
- Petley, D. (2012). Global patterns of loss of life from landslides. *Geology*, 40(10), 927–930. <https://doi.org/10.1130/G33217.1>
- Petschko, H., Brenning, A., Bell, R., Goetz, J., & Glade, T. (2014). Assessing the quality of landslide susceptibility maps - Case study Lower Austria. *Natural Hazards and Earth System Sciences*, 14(1), 95–118. <https://doi.org/10.5194/nhess-14-95-2014>
- Pineda, C. (2019). Análisis de la zona de remoción de masa, sector de la vereda Servitá, municipio de Villavicencio: alcance de la amenaza y soluciones de ingeniería. [Tesis, Universidad Santo Tomas].
- Posit. (2024). RStudio IDE User Guide. Revision 41.
- QGIS Community. (2024). QGIS User Guide for Users.
- Quinn, P. F., Beven, K. J., & Lamb, R. (1995). The $\ln(a/\tan\beta)$ index: How to calculate it and how to use it within the topmodel framework. *Hydrological Processes*, 9(2), 161–182. <https://doi.org/10.1002/HYP.3360090204>
- R Core Team. (2024). R Language Definition version 4.3.3 (2024-02-29).
- Ramírez Criollo, N. L. (2012). Análisis de las investigaciones en el posgrado de geotecnia en la Universidad Nacional de Colombia sede Bogotá [Tesis Maestría, Universidad Nacional de Colombia, Sede Bogota]. Repositorio Unal.
- RCN Radio. (2018). Cuál es la situación actual de la vía al Llano? Recuperado 5 de enero de 2024, de <https://www.rcnradio.com/especiales/cu-al-es-la-situacion-actual-de-la-al-llano>
- Regmi, N. R., Giardino, J. R., McDonald, E. V., & Vitek, J. D. (2014). A comparison of logistic regression-based models of susceptibility to landslides in western Colorado, USA. *Landslides*, 11(2), 247–262. <https://doi.org/10.1007/s10346-012-0380-2>
- Riley, S., DeGloria, S., & Elliot, R. (1999). A Terrain Ruggedness that Quantifies Topographic Heterogeneity. *Intermountain Journal*, 5(1–4), 23–27. http://download.osgeo.org/qgis/doc/reference-docs/Terrain_Ruggedness_Index.pdf
- Rodríguez, N. L. (2001). Mecanismos de falla de taludes en depósitos de ladera que suprayacen lutitas cizalladas en la

- variante Cáqueza de la vía Bogotá-Villavicencio. Tesis de Maestría. Universidad Nacional de Colombia. Bogotá
- Rotigliano, E., Martinello, C., Hernández, M. A., Agnesi, V., & Conoscenti, C. (2019). Predicting the landslides triggered by the 2009 96E/Ida tropical storms in the Ilopango caldera area (El Salvador, CA): optimizing MARS-based model building and validation strategies. *Environmental Earth Sciences*, 78, 210. <https://doi.org/10.1007/s12665-019-8214-3>
- Rouse Jr, J. W., Haas, R. H., Schell, J. A., & Deering, D. W. (1974). Third Earth Resources Technology Satellite-1 Symposium: The Proceedings of a Symposium Held by Goddard Space Flight Center at Washington, DC on 10–14 December 1973: Prepared at Goddard Space Flight Center; Scientific and Technical Information Office. National Aeronautics and Space Administration: Washington, DC, USA, 351, 309.
- Sanchez, C.E. & Urrego L.F. (2011) Metodología para la Evaluación de Riesgo en Corredores Viales. [Tesis Maestría, Pontificia Universidad Javeriana]. Repository Javeriana
- Scheip, C. M. and Wegmann, K. W. (2021) HazMapper: a global open-source natural hazard mapping application in Google Earth Engine, *Nat. Hazards Earth Syst. Sci.*, 21, 1495–1511, <https://doi.org/10.5194/nhess-21-1495-2021>.
- Servicio Geologico Colombiano, & Universidad Pedagógica y Tecnológica de Colombia. (2018a). Mapa Geomorfológico Aplicado a Movimientos en Masa Plancha 247 Bogota Sur Este (Caqueza).
- Servicio Geologico Colombiano, & Universidad Pedagógica y Tecnológica de Colombia. (2018b). Mapa Geomorfológico Aplicado a Movimientos en Masa Plancha 266 Villavicencio.
- Servicio Geologico Colombiano, Leiva O.Y., Moya Berbeo H.G., Trejos Gonzalez G.A., & Carvajal J.H. (2012). Propuesta Metodológica Sistemática Para La Generación De Mapas Geomorfológicos Analíticos Aplicados A La Zonificación De Amenaza Por Movimiento En Masa Escala 1:100,000.
- Servicio Geologico Colombiano. (2020). Inventario de movimientos en masa por tipo de movimiento. ArcGIS Map Viewer. Recuperado 5 de enero de 2024, de <https://www.arcgis.com/home/item.html?id=accfa961f1d249c7a1efe2cc3d1ed326>
- Shano, L., Raghuvanshi, T. K., & Meten, M. (2020). Landslide susceptibility evaluation and hazard zonation techniques – a review. In *Geoenvironmental Disasters* (Vol. 7, Issue 1). Springer. <https://doi.org/10.1186/s40677-020-00152-0>
- Shary, P. A. (1995). Land surface in gravity points classification by a complete system of curvatures. *Mathematical Geology* 1995 27:3, 27(3), 373–390. <https://doi.org/10.1007/BF02084608>
- Sim, J., Wright, C.C., 2005. The kappa statistic in reliability studies: use, interpretation, and sample size requirements. *Phys. Ther.* 85 (3), 257–268.
- Soeters R., van Westen C.J. (1996) Slope instability recognition, analysis, and zonation. In: Turner AK, Schuster RL, editors. *Landslides: investigation and mitigation*. (Special Report; vol. 247). Washington, D.C.: National Academy Press; p. 129-177.
- Steger, S., Brenning, A., Bell, R., & Glade, T. (2016). The propagation of inventory-based positional errors into statistical landslide susceptibility models. *Natural Hazards and Earth System Sciences*, 16(12), 2729–2745. <https://doi.org/10.5194/nhess-16-2729-2016>

- Steger, S., Brenning, A., Bell, R., & Glade, T. (2017). The influence of systematically incomplete shallow landslide inventories on statistical susceptibility models and suggestions for improvements. *Landslides*, 14(5), 1767–1781. <https://doi.org/10.1007/s10346-017-0820-0>
- Stehman, S.V., 1997. Estimating standard errors of accuracy assessment statistics under cluster sampling. *Remote Sens. Environ.* 60 (3), 258–269.
- Tien Bui, D., Tuan, T. A., Klempe, H., Pradhan, B., & Revhaug, I. (2016). Spatial prediction models for shallow landslide hazards: a comparative assessment of the efficacy of support vector machines, artificial neural networks, kernel logistic regression, and logistic model tree. *Landslides*, 13(2), 361–378. <https://doi.org/10.1007/S10346-015-0557-6/FIGURES/7>
- Valero-Carreras, D., Alcaraz, J., & Landete, M. (2023). Comparing two SVM models through different metrics based on the confusion matrix. *Computers & Operations Research*, 152, 106131.
- Valora Analitik (2019, 13-July). Derrumbe mantiene cerrada vía Bogotá-Villavicencio [video]. Youtube. https://www.youtube.com/watch?v=t5w2_IW0ys4
- Vargas-Cuervo, G., Rotigliano, E., & Conoscenti, C. (2019). Prediction of debris-avalanches and -flows triggered by a tropical storm by using a stochastic approach: An application to the events occurred in Mocoa (Colombia) on 1 April 2017. *Geomorphology*, 339, 31–43. <https://doi.org/10.1016/J.GEOMORPH.2019.04.023>
- Varnes, D. J. (1978). Slope Movement Types and Processes.
- Venables, W. N., Smith, D. M., & R Core Team. (2024). An Introduction to R Notes on R: A Programming Environment for Data Analysis and Graphics Version 4.4.0 Under development (2024-03-16). In R. Gentleman & R. Ihaka Copyright c.
- Volando en Drone (2019, 29 May). Volando en Drone, MAVIC 2 ZOOM 4K , SECTOR DERRUMBE KM 58 VIA BOGOTA - VILLAVICENCIO. [video]. Youtube. <https://www.youtube.com/watch?app=desktop&v=Pu3LGebn9pU>
- Vorpahl, P., Elsenbeer, H., Märker, M., & Schröder, B. (2012). How can statistical models help to determine driving factors of landslides? *Ecological Modelling*, 239, 27–39. <https://doi.org/10.1016/j.ecolmodel.2011.12.007>
- Wang, L., & Liu, H. (2006). An efficient method for identifying and filling surface depressions in digital elevation models for hydrologic analysis and modelling. *International Journal of Geographical Information Science*, 20(2), 193-213.
- Watkins, R. L. (2019). Terrain Metrics and Landscape Characterization from Bathymetric Data: SAGA GIS Methods and Command Sequences.
- Weiss, A. (2001). Topographic position and landforms analysis. In ESRI user conference (Vol. 200).
- Zevenbergen, L. W., & Thorne, C. R. (1987). Quantitative analysis of land surface topography. *Earth Surface Processes and Landforms*, 12(1), 47–56. <https://doi.org/10.1002/ESP.3290120107>